

CONNECTING THE DOTS: COMPARING SPH SIMULATIONS AND
SYNTHETIC OBSERVATIONS OF STAR-FORMING CLUMPS IN MOLECULAR
CLOUDS

CONNECTING THE DOTS: COMPARING SPH SIMULATIONS
AND SYNTHETIC OBSERVATIONS OF STAR-FORMING CLUMPS
IN MOLECULAR CLOUDS

By

RACHEL LOUISE WARD, B.SC. SPEC. HON., YORK UNIVERSITY, 2009

A Thesis

Submitted to the School of Graduate Studies

in Partial Fulfilment of the Requirements

for the Degree

Master of Science

McMaster University

©Copyright by Rachel Ward, September 2011

MASTER OF SCIENCE (2011)
(Department of Physics and Astronomy)

McMaster University
Hamilton, Ontario

TITLE: Connecting the Dots: Comparing SPH Simulations and Synthetic
Observations of Star-forming Clumps in Molecular Clouds

AUTHOR: Rachel Ward, B.Sc. Spec. Hon., York University, 2009

SUPERVISOR: Alison Sills & James Wadsley

NUMBER OF PAGES: xiv, 129

Abstract

The gravitational collapse of a giant molecular cloud produces localized dense regions, called clumps, within which low-mass star formation is believed to occur. Recent studies have shown that limitations of current observing techniques make it difficult to correctly identify and measure properties of these clumps that reflect the true nature of the star-forming regions. In order to make a direct comparison with observations, we produced synthetic column density maps and a spectral-line cube from the simulated collapse of a large 5000 solar mass molecular cloud. The synthetic observations provide us with the means to study the formation of star-forming clumps and cores in our simulation using methods typically used by observers. Since we also have the full 3D simulation, we are able to provide a direct comparison of ‘observed’ and ‘real’ star-forming objects, highlighting any discrepancies in their physical properties, including the fraction of cores which are gravitationally bound. We have accomplished this by studying the global properties of the star-forming objects, in addition to performing a direct correlation of individual objects to determine the error in the observed mass estimates. By correlating the clumps found in the simulation to those found in the synthetic observations, we find that the properties of objects derived from the spectral-line data cube were more representative of the true physical properties of the clumps, due to effects of projection greatly impacting the estimates of clump properties derived from two-dimensional column density maps.

Acknowledgements

Firstly, I would like to thank my supervisors, Alison Sills and James Wadsley. To Alison, for being such a wonderful mentor and to James, for his great enthusiasm and creativity. I cannot thank you both enough for this opportunity and for your continued guidance and support.

To my committee member, Christine Wilson, for her wonderful input and advice, which helped make this thesis what it is today. I would also like to thank Mike Reid, for providing great insight and for being incredibly helpful, especially when I was first learning to use “observer’s tools”.

To my office mates, for getting me out of more segmentation faults than I can remember and for always keeping the laughs coming.

This work could not have been possible without the support of SHARCNET and Compute/Calcul Canada, which provided dedicated resources to run these simulations. I would like to thank Nicolas Petitclerc, who performed the simulations and upon whose PhD thesis, this work is built. I would also like to acknowledge NSERC for their support by funding this research.

To my friends and fellow grad students, for the lunch-time conversations, coffee runs, and softball games, which were enormous fun and made even the toughest times more bearable. I look forward to many more good times in the future.

I would like to thank my family, especially my parents, who have always supported me through every endeavour. I am so blessed to have their constant love, support, and unbroken promise that everything would always turn out okay.

Lastly, to Aaron, for being my constant. Thank you for making my day every day.

Dedicated to my everything, Aaron.

Table of Contents

Descriptive Notes	ii
Abstract	iii
Acknowledgements	iv
List of Figures	viii
List of Tables	xiv
Chapter 1 Introduction	1
Chapter 2 Star Formation: The Theoretical and Observational Perspective	9
2.1 Introduction	9
2.2 The Formation of Stars	10
2.3 Smoothed Particle Hydrodynamics	21
2.4 Summary	24
Chapter 3 Viewing the Simulation through the Observer's Eyes	33
3.1 Introduction	33
3.2 The Simulation	34
3.3 Synthetic Observations	39
3.4 Observer's Tools	50
3.4.1 Clumpfind	51

3.4.2	Starlink	54
3.5	Summary	56
Chapter 4 Analysis & Results		61
4.1	Introduction	61
4.2	Clump-Finding and Correlations	62
4.2.1	Studying Clumps in the Third Dimension	62
4.2.2	Clump Correlations, Round One: PP vs. PPP	68
4.2.3	Clump Correlations, Round Two: PPV vs. PPP	85
4.3	Boundedness	99
4.4	Connecting the Dots: Traceable Properties?	110
4.5	Summary	119
Chapter 5 Summary and Future Work		125

List of Figures

2.1	The Polaris flare - a prime example of the initial phase of molecular cloud formation - as observed using SPIRE in the far-infrared and sub-millimetre wavelengths (Figure credit: ESA/ Herschel/ SPIRE/ Ph. André (CEA Saclay) for the Gould Belt survey Key Programme Consortium and A. Abergel (IAS Orsay) for the Evolution of Interstellar Dust Key Programme Consortium).	16
2.2	Kernel function, $W(r,h)$, with a minimum smoothing length of $h = 50$ AU.	23
3.1	Visualisation of our simulation made using SPLASH (Price, 2007) of a dense core of gas forming in a molecular cloud collapse simulation. The colour scale shows density in units of M_{\odot}/AU^3 ($\approx 10^{17} \text{ cm}^{-3}$). The region shown is 1.5 pc by 1 pc in size, where, for comparison, a typical clump can be of order 1 pc in size and a typical core can be of order 0.1 pc in size.	35
3.2	The line of sight column density was divided up along a grid with the particle mass divided by the kernel weights. The lines of sight are taken to be the vertices where the grid intersects.	41
3.3	Two-dimensional column density map of spherical molecular cloud collapse. The resolution of the map is 6000 AU/pixel with projection along the z-axis onto a 500 x 500 grid. Note the filamentary structure comparable to that seen in observations. The column density is in units of solar mass per pixel.	44

3.4	Higher resolution two-dimensional column density map of spherical molecular cloud collapse. The resolution of the map is 2000 AU/pixel with projection along the z-axis onto a 1250 x 1250 grid. The column density is in units of solar mass per pixel.	45
3.5	Visualisation provided by the Joint Astronomy Centre (JAC) of a spectral-line data cube. The third dimension traces the velocity of the gas.	46
3.6	Column density maps produced from collapsed PPV data cubes. Figure 3.6(a) includes all of the emission along the line of sight and Figure 3.6(b) includes only the densest gas traced by the NH ₃ (1,1) molecular line transition.	50
3.7	A sample of spectral-line data from Smith (2009) displaying how Clumpfind identifies clumps from 3d data.	52
3.8	A sample contour map from Williams et al. (1994) displaying how Clumpfind identifies clumps. Clump A is identified at the highest contour level and clumps B, C, and D are identified at lower contour levels.	53
4.1	Clump mass function (CMF) derived from the PPP cube with a resolution of 6000 AU/pixel. The error bars correspond to \sqrt{N} counting statistics. The blue dotted line is the Salpeter (1955) IMF.	67

4.2	Cross-section slices of the simulation in the xz-plane. Large filaments of low density gas are present along the z-axis, chosen to be our line of sight, when observed in the xz-plane. These three cases show what could possibly be perceived as one clump in the xy-plane are more likely one clump (top), two clumps (middle), or no defined clumps (bottom) contaminated by excess low-density material along the line of sight. These slices have a width of 1.5×10^5 AU and a length of 2×10^6 AU, extending fully across the simulation.	70
4.3	Left: PP column density map of spherical molecular cloud collapse for a resolution of 6000 AU/pixel with projection along the z-axis onto a 500 x 500 grid. Right: The remaining emission contained in the clumps identified by CLUMPFIND for the PPP case after the cube has been collapsed.	73
4.4	Clump mass function of the clumps identified in the PP column density map using Clumpfind2d (red solid line) compared to a clump mass function of clumps identified from the same PP column density map using our ‘Correlation’ method (red dashed line).	75
4.5	Clump mass function of the clumps identified in the PPP data cube (blue solid line). Also shown is the clump mass function of the same clumps with their masses estimated from the 2D (x,y) projected PP image (red dotted line).	76

4.6	This figure from Alves et al. (2007) compares the dense core mass function (DCMF) from observations of star-forming regions in the Pipe Nebula to the stellar IMF of the Trapezium cluster. The authors suggest that the two mass functions differ only by a uniform star formation efficiency factor.	77
4.7	Plot of the “observed” mass (PP) vs. the “actual” mass (PPP). The dashed black line is the 1-to-1 line.	80
4.8	Log-log plot of the “observed” mass (PP) vs. the “actual” mass (PPP). A fit to the data is shown as a solid red line.	82
4.9	Log-log plot of the “observed” mass (PP) vs. the “actual” mass (PPP) for various cases. Regardless of the age of the clumps, orientation, or initial collapse condition (Spherical, Ribbon, Filament, or Sheet), the trend remains consistent.	83
4.10	Velocity spectrum for a single line of sight. The mean velocity, \bar{v}_z , and velocity ranges, $[\bar{v}_z - \sigma_z/2, \bar{v}_z + \sigma_z/2]$ and $[\bar{v}_z - \sigma_z, \bar{v}_z + \sigma_z]$, are shown to demonstrate the velocity cuts made by our correlation method.	88
4.11	A PPV clump visualised in three dimensions with XY (left), XZ (centre), and YZ (right) projections. Large amounts of extended emission are present along the line of sight (the z-axis). This particular clump has a radius of approximately 0.2 pc in the XY-plane, but it also includes material along the line of sight which spans a distance of 2.5 pc. This large column of gas is evident in Figure 4.11(b) and 4.11(c).	91

4.12	Clump mass function of the clumps identified in the PPP data cube (blue solid line) plotted with the clump mass function of the same clumps with their masses estimated from the (x,y,v_z) PPV data cube including all emission (red dotted line) for both the $\sigma_z/2$ case and the σ_z case.	92
4.13	Clump mass function of the clumps identified in the PPP data cube (blue solid line) compared to the clump mass function of the same clumps with their masses estimated from the NH_3 (1,1) emission of the (x,y,v_z) PPV data cube (red dotted line). . . .	94
4.14	Plots of the “observed” mass (PPV) vs. the “actual” mass (PPP) for the $\bar{v}_z \pm \sigma_z/2$ and $\bar{v}_z \pm \sigma_z$ cases. The dashed black line is the 1-to-1 line.	95
4.15	Log-log plots of the “observed” mass (PPV) vs. the “actual” mass (PPP) for the $\bar{v}_z \pm \sigma_z/2$ and $\bar{v}_z \pm \sigma_z$ cases. Fits to the data are shown as solid red lines.	97
4.16	Plots of the “observed” mass (PPV) vs. the “actual” mass (PPP) for the $\bar{v}_z \pm \sigma_z$ case comparing the PPV masses obtained using all emission and the PPV masses obtained from only the highest density gas traced by NH_3	98
4.17	Prestellar core mass function (purple dotted line) plotted along with the CMF for clumps identified in the PPP data cube (blue solid line) and the CMF of the same clumps with their masses estimated from the PP column density map (red dotted line).	107

4.18	Plot of the relation between the observed and theoretical virial parameters. All candidate clumps are included using their initial properties. The calculated theoretical virial parameter equals $ 2K/U $ and the observed virial parameter is equal to $5\sigma^2 R_{1/2}/GM_i$, where $R_{1/2}$ is the half-mass radius and M_i is the initial PPP mass. The dashed black line is the 1-to-1 line and a zoom-in of the plot is shown as an inset. The red symbols mark the 11 candidate clumps which will eventually be classified as bound prestellar cores.	112
4.19	Plot of the relation between the observed and theoretical virial parameters for the bound prestellar cores. An object can be defined as bound if $\alpha_{vir} \leq 1$ in either axis.	113
4.20	The size-linewidth relation for the prestellar cores. A fit to the data is shown as a red solid line and Larson's third law is shown as a blue dashed line.	115
4.21	Column density map, produced by collapsing the full PPP cube, shown with the corresponding mean velocity map and intensity-weighted velocity dispersion map for the molecular line emission along the line of sight.	116
4.22	Doppler-broadened velocity spectra map generated from a PPV data cube with a resolution of 2000 AU/pixel and a velocity channel width of 0.04 km s^{-1} . These maps include all of the emission of the gas along the line of sight.	117

List of Tables

3.1	Initial conditions of the SPH simulation of a giant molecular cloud	36
4.1	Total mass contained in clumps	65
4.2	Table of Clumpfind2d Parameter Sensitivity	69
4.3	Table of Best Fit Parameters to $M_{PP} = c(M_{PPP})^m$	82
4.4	Table of Best Fit Parameters to $M_{PPV} = c(M_{PPP})^m$	99
4.5	Table of Initial Boundedness Test Results	102
4.6	Table of PP Boundedness Test Results	103
4.7	Properties of the “Prestellar Cores” at 1.30 Myr	106
4.8	Table of Boundedness Test Results	108
4.9	Properties of the most massive “prestellar core” for various cases .	109
4.10	Evolution of σ & α_{vir} for the most massive “prestellar core” . . .	118

Chapter 1

Introduction

Stars are essential to our understanding of the Universe. Star formation is at the forefront of current research as there are still many unanswered questions regarding the conditions which lead to the origin of stars and, eventually, to the origin of life in the Universe. The earliest stages of stellar evolution offer an ideal laboratory for exploring the nature of these conditions and studying formation mechanisms on a stellar scale has reaching impact on many other areas of interest in astronomy, including multiple stellar systems, cluster environments, planet formation, and galaxy evolution.

It is believed that most, if not all, stars form in a cluster environment (Lada & Lada, 2003), where tens to millions of ‘sibling’ stars can all be born at approximately the same time, depending on the physical size of the cluster and the amount of available gas and dust. Within a galaxy, the interstellar medium (ISM) fills the “empty space” between stars and is composed of diffuse gas and dust. The stellar birth clusters are formed out of cold clouds of dense molecular hydrogen gas and dust found in certain regions of the ISM. These dense regions of the ISM are highly compressed from shocks due to supernova explosions, which occur when massive stars reach the end of their lifetime, or

from the spiral arms of the galaxy, which, from observations, are where star formation seems to be mostly concentrated (Larson, 2003). It is in these dense regions of self-gravitating molecular gas, known as giant molecular clouds or GMCs, where star clusters form (Bok, 1948; Ward-Thompson, 2002; Larson, 2003). With densities exceeding $100 \text{ particles cm}^{-3}$ (e.g. Blitz, 1993) and temperatures as cold as 10 K (e.g. Larson, 1969), these complexes of gas and dust typically reach sizes spanning hundreds of light-years across and masses up to 10^6 solar masses (Williams & McKee, 1997). Within this cloud, there are forming and newly-formed stars of various masses, which are created from small, compact regions of gas in the cloud. When observing star-forming regions, we look for evidence of these small, compact regions called “clumps” – localized dense regions in the giant molecular cloud which, it is believed, will collapse and fragment into protostellar cores. The centres of these cores reach very high temperatures and become hot enough to ignite nuclear fusion and form a star or multiple stellar system.

There is currently a great deal of excitement in the field of star formation as two new telescopes are poised to achieve both greater sensitivity and higher resolution observations. The Herschel Space Observatory was launched in 2009, and has already opened up new windows of the electromagnetic spectrum which are crucial for studying the cool dust found in star forming regions, but which are not easily observed from the ground. Early science is already underway on the Atacama Large Millimeter Array (ALMA), under construction in Chile, with full capabilities becoming available in 2013. This array of radio telescopes will provide incredible spatial resolution of star-forming

clouds, as well as very precise velocity measurements and spectral resolution of these important regions.

Studying these heavily-obscured star-forming regions is very difficult and there are many inherent biases in the current techniques that are used to observe them. Recent studies (Reid et al., 2010; Curtis & Richer, 2010; Shetty et al., 2010; Pineda et al., 2009; Smith et al., 2008) have shown that limitations of current observing techniques make it difficult to correctly identify and measure properties of these clumps and cores that reflect the true nature of the star-forming regions. Issues which arise from projection effects, assumptions regarding cloud properties, and methods used to extract and analyse data can impact the outcome and interpretation of results. While the Herschel and ALMA observations will disentangle some of these issues, the most self-consistent way to really understand the observational biases is by using large-scale simulations to model the collapse of a molecular cloud.

In recent years, many groups have been interested in studying star formation using simulations (e.g. Federrath et al., 2010; Offner et al., 2009; Bate, 2009; Tilley & Pudritz, 2004). These types of simulations are able to provide a complete picture of the collapse of the molecular cloud, revealing the various effects of turbulence and gravity. Simulations of star-forming clouds can also provide insight into physical parameters without confusion from projection effects. Although there are many physical effects involved in star formation, most simulations use reduced physics for simplicity, regarding only the most dominant physical processes. Provided that any effects which are acting in direct opposition to one another are both included, many goals can be addressed

using only hydrodynamics (turbulence) and self-gravity (e.g. Bate, 2009; Bonnell et al., 2003; Klessen, 2001).

Simulations of the earliest stages of star formation often exclude radiative transfer and the effects of radiative feedback. Radiative transfer becomes significantly important during the later stages of the clump evolution. As the density increases, the gas becomes ‘optically thick’ and the flux can no longer traverse freely through the gas from all depths of the cloud. Once a protostar is formed, it becomes the dominant source of radiation in the cloud and local regions of the gas can be subjected to heating due to the radiative feedback from newly-formed stars. However, for studies of the earliest phase of star formation, one can assume that the cloud is optically thin, thus removing the need for the implementation of radiative transfer and the effects of stellar feedback at this stage.

Using the Smoothed Particle Hydrodynamics (SPH) code, GASOLINE, Pettitlerc (2009) modelled the collapse of a large $5000 M_{\odot}$ molecular cloud. In order to make a direct comparison with observations, we produced synthetic observations from his results. We compare the clumps found using a modified version of a common observer’s tool – the publicly-available clump-finding algorithm, Clumpfind (Williams et al., 1994) – on the three-dimensional simulation to those found from the simulated observations to show the discrepancy between the properties of ‘observed’ clumps and ‘actual’ clumps. From these results, we investigate line-of-sight (LOS) properties which could be used to identify real clumps. Since we have the simulation, we are able to make a connection between observed LOS properties and the true three-dimensional

properties of the molecular cloud, which can provide observers with a context in which they can better interpret their results.

In Chapter 2, we describe the theory of star formation in detail with a discussion of the initial formation and dynamics of giant molecular clouds followed by an outline of the process by which stars are formed. The characteristics of clumps and cores are defined and observational and theoretical studies, including simulations, of star formation are discussed. Chapter 3 provides details of the Petitclerc (2009) simulation and explains the methods used to create our synthetic observations from his results. A detailed explanation of the various observer’s tasks, tools, and techniques we have used in our analysis is also provided. In Chapter 4, we develop an alternative clump extraction method and produce a model based on our results to more accurately represent the physical properties of clumps and cores. Additionally, we explore the nature of bound clumps and unbound clumps to determine whether there are characteristic properties which can be used to distinguish the clumps observationally. This is followed by a brief discussion on the determination of traceable properties which can be used to accurately identify clumps. We close in Chapter 5 with a summary of our results and a presentation of our goals for future research.

‘Observing’ the simulated clumps and following how they evolve will provide us with the answer to what occurs during the earliest stages in stellar evolution. The aim of this thesis is to study the global properties of these giant molecular clouds and determine the effect the environment has on these clumps and their subsequent condensation or fragmentation into even denser cores. Studying the earliest stages of star formation can provide clues as to

the origin of the stellar initial mass function, the distribution of the various stellar masses at the time of their birth. In order to understand the origin of stellar masses, we first need to understand the formation of these molecular cloud cores. We can also explore the origin of stellar multiplicity, such as the formation of binary and multiple star systems, and the origin and universality of the stellar initial mass function. This last question is possibly the most important question to be answered in the theory of star formation.

Bibliography

- Bate, M. R. 2009, MNRAS, 392, 590
- Blitz, L. 1993. Giant Molecular Clouds. In *Protostars and Planets III*, eds. E. H. Levy and J. I. Lunine (Tucson: University of Arizona Press), pp. 125-161
- Bok, B. 1948, Centennial Symp., Harvard Obs. Monogr. No. 7, 53
- Bonnell, I. A., Bate, M. R., & Vine, S. G. 2003, MNRAS, 343, 413
- Curtis, E. I. & Richer, J. S. 2010, MNRAS, 402, 603
- Federrath, C., Banerjee, R., Clark, P. C., & Klessen, R. S. 2010, ApJ, 713, 269
- Klessen, R. S. 2001, ApJ, 556, 837
- Lada, C. J. and Lada, E. A. 2003, ARA&A, 41, 57
- Larson, R. B. 1969, MNRAS, 145, 271
- Larson, R. B. 2003, Rep. Prog. Phys., 66, 1651
- Offner, S. S. R., Klein, R. I., McKee, C. F., & Krumholz, M. R. 2009, ApJ, 703, 131
- Petitclerc, N. 2009, PhD Thesis, McMaster University

Pineda, J. E., Rosolowsky, E. W., & Goodman, A. A. 2009, *ApJL*, 699, L134

Reid, M. A., Wadsley, J., Petitclerc, N., & Sills, A. 2010, *ApJ*, 719, 561

Shetty, R., Collins, D. C., Kauffmann, J., Goodman, A. A., Rosolowsky, E. W., & Norman, M. L. 2010, *ApJ*, 712, 1049

Smith, R. J., Clark, P. C., & Bonnell, I. A. 2008, *MNRAS*, 391, 1091

Tilley, D. A., & Pudritz, R. E. 2004, *MNRAS*, 353, 769

Ward-Thompson, D. 2002, *Science*, 295, 76

Williams, J. P., de Geus, E. J., & Blitz, L. 1994, *ApJ*, 428, 693

Williams, J. P. & McKee, C. F. 1997, *ApJ*, 476, 166

Chapter 2

Star Formation: The Theoretical and Observational Perspective

2.1 Introduction

In this chapter, we will discuss the formation of stars and the nature of the clouds, clumps and cores out of which stars form. Turbulence is a key factor in determining the morphology of a cloud, and its significance to star formation and its effect on the mass distribution of stars will also be discussed. We describe recent observational and theoretical studies, which include simulations of clouds and dense cores, and how these results have led to a better understanding of the earliest stages of star formation. We will also describe a computational technique, smoothed particle hydrodynamics, used to model fluid flows with details of its application to the formation of stars.

2.2 The Formation of Stars

In dense regions of self-gravitating molecular gas, known as giant molecular clouds or GMCs, star clusters form (Larson, 2003). These GMC complexes, which are primarily composed of molecular hydrogen (Stahler & Palla, 2004), can reach sizes spanning hundreds of light-years across and masses up to 10^6 solar masses (Williams & McKee, 1997). These molecular clouds form out of the diffuse interstellar medium (ISM) and have been shown to have a highly filamentary structure, thought to be largely due to turbulence (e.g. Miville-Deschênes et al., 2010; Men'shchikov et al., 2010; Schmalzl et al., 2010).

It is believed that turbulence, defined to be the multi-scale random motions of a fluid flow, is greatly significant in the early stages of star formation (Mac Low & Klessen, 2004; Ballesteros-Paredes et al., 2007). Non-uniform driven turbulence, which can be due to shocks from nearby supernovae explosions (Larson, 2003), can greatly compress the gas flows within the diffuse ISM. Velocity fluctuations from the driven turbulence create density enhancements in the diffuse ISM, leading to the formation of GMCs. Within a molecular cloud, turbulence is highly supersonic (Larson, 1981) and while it is believed that supersonic turbulence can globally support GMCs against gravitational collapse, it can also promote local collapse of small-scale regions within a molecular cloud (Elmegreen & Scalo, 2004; Mac Low & Klessen, 2004). The theory that star formation arises as a consequence of 'turbulent fragmentation' provides a valid explanation for the shape of the observed mass distribution of stars (Padoan & Nordlund, 2002).

Larson (1981) concluded that turbulent processes are incredibly important to the formation of substructure that is observed in giant molecular clouds. The key traits of GMC dynamics can be summarized by Larson’s three laws (Larson, 1981). Larson’s first law shows a size-linewidth relation, which indicates that the velocity dispersion of a cloud increases with increasing size of the cloud. Based on observational data, Larson’s first law is given by the equation:

$$\sigma \text{ (km s}^{-1}\text{)} = 1.10 L(\text{pc})^{0.38}$$

where σ is the 3d internal velocity dispersion and L is the maximum linear dimension. Further studies by Solomon et al. (1987) have shown that this relation can be more accurately represented as:

$$\sigma \text{ (km s}^{-1}\text{)} \propto L(\text{pc})^{0.5}$$

This law has been shown to apply to large length-scales all the way down to the small length-scales of the subcondensations within the cloud (0.1 – 1000 pc).

Larson’s second law states that GMCs are gravitationally bound and are in approximate virial equilibrium. The virial theorem relates the kinetic energy of the gas to the gravitational potential energy. For a self-gravitating object, the virial theorem states that

$$U = -2K$$

where U is the total gravitational potential energy and K is the total kinetic energy of the cloud. An object in virial equilibrium satisfies the virial theorem

and is said to be ‘virialised’. To test whether an object is bound, a parameter called α can be defined as

$$\alpha = |2K/U|$$

If $\alpha \leq 1$, then the object is bound; otherwise, it is unbound. This virial parameter, or α_{vir} , is a observational test of gravitational boundedness often used in the study of star formation (e.g. Bertoldi & McKee, 1992; Dib et al., 2007; Heyer et al., 2001; Krumholz & McKee, 2005).

Larson’s third law is the column density of the cloud is nearly independent of the cloud size. If GMCs have approximately constant column densities and are in virial equilibrium, then the size-linewidth relation can be expressed as $\sigma \propto L^{1/2}$, which Larson (1981) claims is not significantly different from the observed relation and is in greater agreement with the results of Solomon et al. (1987).

These three laws are thought to be fundamental to the dynamics of molecular clouds and star formation and are significant on all size scales. As such, we should expect that the size-linewidth relation and the virial parameter also apply to small dense substructures within the molecular cloud.

As these GMCs undergo gravitational collapse, clumpy and filamentary structure will begin to form. Large, overdense structures in the gas are often referred to as clumps. Current estimates of molecular cloud sizes are approximately 50 pc across with masses ranging from $10^4 - 10^6$ solar masses (Williams et al., 2000); however, star-forming clumps within a molecular cloud can be quite massive themselves, out of which entire stellar clusters can form. Since it is believed that more than 90% of stars form in clusters (Lada & Lada,

2003), these environments are excellent laboratories for studying star formation. These embedded clusters can have more than 100 stars with cluster masses greater than $50 M_{\odot}$; however, very few of these embedded clusters ($< 5\%$) will remain bound systems, likely due to the rapid dispersal of the surrounding gas from outflows from massive stars (Lada & Lada, 2003; Matzner & McKee, 2000). Deeply embedded in the clumps are the heavily-obscured dense cores – stars at their birth in the earliest stages of their formation. According to Bergin & Tafalla (2007), a clump is defined as having a size of 0.3 – 3 pc and containing 50 – 500 solar masses and a core is defined as being 0.03 – 0.2 pc in size and having a mass of 0.5 – 5 solar masses. As an example, the typical size of a core in the ρ Ophiuchus molecular cloud observed using the James Clerk Maxwell Telescope (JCMT) at $850 \mu\text{m}$ is 3×10^3 AU, or 0.01 pc, averaged from 93 identified cores with a total core mass of approximately 29 solar masses for cores ranging in mass from 0.1 – 10 solar masses (Simpson, Nutter, & Ward-Thompson, 2008).

A dense core is defined by Myers (1999) as a condensation with a mean H_2 density greater than 10^4 cm^{-3} and a size of ~ 0.1 pc across. A “clump” is defined as being ~ 1 pc across with a mean H_2 density $\gtrsim 10^3 \text{ cm}^{-3}$ and a region ~ 10 pc with a mean H_2 density $\gtrsim 10^2 \text{ cm}^{-3}$ is called a “complex” (Gammie et al., 2003; Myers, 1999). These definitions are also consistent with those presented by Bergin & Tafalla (2007). We have chosen to define any object identified in our simulation that is less than 0.1 pc in size and has a mean density greater than 10^4 cm^{-3} as a “core”. We also adopt the terminology often used in the literature for dense core classification. Any dense core which is without association to a young stellar object is considered to be a starless or

prestellar core (Di Francesco et al., 2007; Ward-Thompson et al., 2007). Often, starless cores are defined as being gravitationally unbound objects. Prestellar cores are often considered as starless cores which are gravitationally bound, but can also be described by emission of NH_3 , high densities ($10^5 - 10^6 \text{ cm}^{-3}$), and the presence of inflowing material (Di Francesco et al., 2007). Since it is difficult to determine observationally whether or not a core is bound, observers often use the latter criteria to classify prestellar cores. We have chosen to classify our dense cores using the boundedness criterion, as we are able to easily obtain this information from our simulation. Thus, any candidate objects will be either classified as a starless core if unbound, or prestellar core if bound, provided the sizes and densities satisfy the earlier definition.

Many nearby molecular clouds, such as Perseus (Kirk et al., 2006), Taurus (Onishi et al., 1998), ρ Ophiuchus (Motte et al., 1998; Johnstone et al., 2000), and Orion (Johnstone & Bally, 1999), have been mapped to search for star-forming cores. These regions exhibit varying degrees of star formation activity, with the Orion molecular cloud complex displaying the most active level of star formation present amongst these nearby clouds.

Alternatively, the Polaris flare, shown in Figure 2.1, displays little to no star formation activity. It is a Galactic cirrus cloud with a total mass of approximately 5500 solar masses (Heithausen & Thaddeus, 1990) and is located at a distance less than 150 pc away (Falgarone et al., 1998). The Polaris flare is an excellent example of the initial stage of molecular cloud formation, as it is in the process of transitioning from a diffuse gas to a molecular cloud (Miville-Deschênes et al., 2010). Dense molecular regions within the cloud

host many starless and prestellar cores, the precursors to stars; however, most of the cores found in the Polaris flare are unbound, meaning that there is no sign of any active star formation (André et al., 2010).

Our understanding of how stars form in cluster environments has greatly improved in recent years, particularly by studies of the ρ Ophiuchus cloud, which is the nearest example of clustered star formation. Studying different types of dark, dense clouds can lead to an even better understanding of the effects of environment on the formation of cores. Heavily-obscured forming and newly-formed stars are deeply embedded in a molecular cloud, where the dust and gas make these regions almost opaque in optical wavelengths. Therefore, observations of star-forming regions are made primarily in infrared, submillimetre, or radio wavelengths (e.g. Ward-Thompson et al., 2010; Di Francesco et al., 2007; Tachihara et al., 2002; Johnstone et al., 2000).

Observations of molecular hydrogen, H_2 , line emission are desired in order to trace the dense regions within molecular clouds; however, for observers, H_2 is generally not directly observable, as the gas does not reach temperatures which allow for emission to occur (Di Francesco et al., 2007). Fortunately, certain molecular line emission, such as from CO, and infrared emission from dust can act as proxies for molecular hydrogen to trace the dense gas in the interiors of molecular clouds.

Dust grains within a molecular cloud are thermally-heated by surrounding photons and emit infrared continuum emission, radiating as a modified blackbody at an average dust temperature. Observers are able to produce column density maps (see Figure 2.1) from sub-millimetre continuum emission

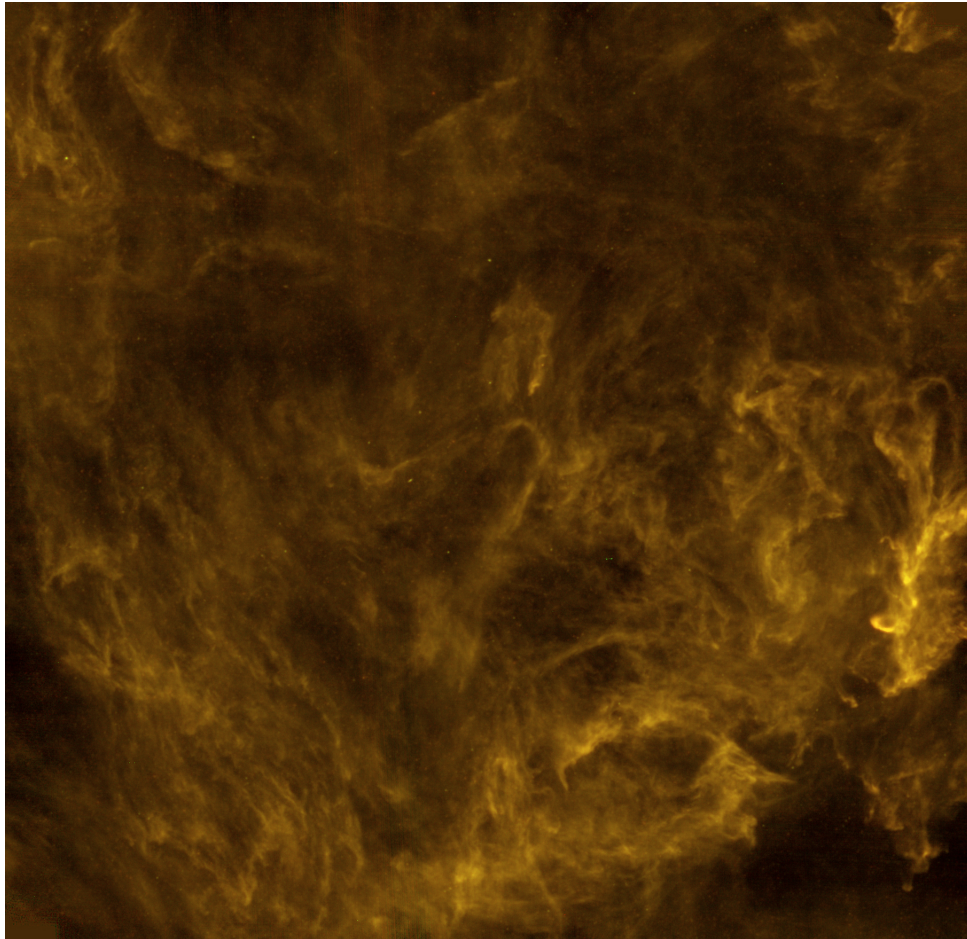


Figure 2.1: The Polaris flare - a prime example of the initial phase of molecular cloud formation - as observed using SPIRE in the far-infrared and sub-millimetre wavelengths (Figure credit: ESA/ Herschel/ SPIRE/ Ph. André (CEA Saclay) for the Gould Belt survey Key Programme Consortium and A. Abergel (IAS Orsay) for the Evolution of Interstellar Dust Key Programme Consortium).

observations, using measurements of the opacity of the dust grains. Since the dust is optically thin, the observed flux measurements include emission from all depths of the cloud. The dust opacity combined with the dust temperature provides an estimate of the dust column density (Hildebrand, 1983). If the gas and dust are assumed to be thermally coupled, the dust column density can be converted to H_2 column density by using an assumed constant gas-to-dust mass ratio (Ossenkopf & Henning, 1994).

Molecular hydrogen can also be traced by other molecules often found in the presence of H_2 , which are abundant and are directly observable. After H_2 , carbon monoxide (CO) is the second most abundant molecule in the universe (Wilson et al., 1970). The adopted value for $\alpha = N(\text{H}_2)/I_{\text{CO}}$ is $\alpha \approx (2 - 3) \times 10^{20} \text{ cm}^{-2} (\text{K km/s})^{-1}$ (Solomon et al., 1987; Young & Scoville, 1991; Henkel & Wiklind, 1997). The integrated intensity, I_{CO} , is derived from the following equation

$$I_{\text{CO}} = \int T(\text{CO}) dv$$

(Langer et al., 1989) where $T(\text{CO})$ is the brightness temperature of the CO species integrated over the velocities, v , where emission occurs. The temperature and velocities can be obtained from spectral-line observations. The column density of H_2 is thus effectively a mass estimate, as $N(\text{H}_2)/I_{\text{CO}}$ is approximately equal to M/L_{CO} , where M is the mass in M_{\odot} and L_{CO} is the luminosity in units of $\text{K km s}^{-1} \text{ pc}^2$.

Spectral-line observations of particular transitions of CO emission have a limited dynamic range, such as for the case of the ^{12}CO (1-0) rotational line transition, which maps densities in the range of $n_{\text{H}_2} \approx 10^{2.5} - 10^4 \text{ cm}^{-3}$.

The ^{13}CO isotope of CO is often used as a tracer for H_2 as it is optically thin and it can be excited to high densities. However, carbon-bearing species become depleted as they “freeze-out” or are adsorbed onto dust grains at high densities within the dense cores. Molecular nitrogen, N_2 , is slightly more volatile than CO and is the precursor to nitrogen-hydrogen molecules, such as NH_3 and N_2H^+ , which remain in a gaseous state to very high densities without being depleted (Caselli et al., 2002a). Nitrogen-bearing molecules are excellent tracers of dense cores and appear to survive to even higher densities than their carbon-bearing counterparts (Caselli et al., 2002c; Bergin & Tafalla, 2007). The NH_3 (1,1) line transition is excited at high densities in cloud cores at a critical excitation density of 1800 cm^{-3} (Tielens, 2005) and NH_3 is expected to deplete only at very high densities $\geq 10^6 \text{ cm}^{-3}$ (Bergin & Langer, 1997; Pagani et al., 2005). NH_3 is also in high abundance in dense cores and its continued presence at the high densities of core interiors makes NH_3 is one of the best tracers of the physical, chemical, and kinematic properties of dense cores.

Several key parameters which can be obtained from an observation of a star-forming region are its mass, radius, and velocity dispersion. These can be derived using measurements of the intensity of the region, which is commonly in units of K km s^{-1} , obtained from dust continuum maps or from spectral-line radio observations. Based on the masses derived from the measured column densities and integrated intensities of GMC observations, a mass distribution of the cloud substructure can be obtained. This is often referred to as the clump mass function or CMF. The CMF reflects very closely what is seen in the stellar initial mass function (IMF), the distribution of stellar masses at

the time of their birth. Since it has been shown that stars form from dense cores (e.g. Kirk et al., 2006; Motte et al., 1998; Johnstone et al., 2000), many believe that the form of the stellar IMF is fixed by the mass distribution of the clumps and cores.

A star’s mass at the time of its birth is determined from observations of clustered star formation and it appears that the stellar mass distribution seems to follow a multiple power law or log-normal trend. The functional form of the IMF was originally represented by Salpeter (1955) as

$$dN \propto m^{-\alpha} dm$$

where the best description for the high-mass end of the IMF was given by:

$$dN \propto m^{-2.35} dm, \quad 1 \leq m/M_{\odot} < 10$$

Since that time, there have been several alternative functional forms of the IMF, such as the Kroupa (2001) multiple power law IMF expressed as

$$dN \propto \begin{cases} m^{-0.3} dm, & 0.01 \leq m/M_{\odot} < 0.08 \\ m^{-1.3} dm, & 0.08 \leq m/M_{\odot} < 0.5 \\ m^{-2.3} dm, & 0.5 \leq m/M_{\odot} < 100 \end{cases}$$

and the Chabrier (2003) lognormal IMF for multiple systems. The lognormal form of the the IMF was first suggested by Miller & Scalo (1979), which has the functional form

$$\xi(\log m) = \frac{A}{\sqrt{2\pi}\sigma} \exp \left[-\frac{(\log m - \log m_c)^2}{2\sigma^2} \right]$$

where m_c is the mean mass and $\sigma^2 = \langle (\log m - \langle \log m \rangle)^2 \rangle$ is the variance of the mass. The lognormal form is a particularly good approximation of the IMF when extended to lower masses.

Motte et al. (1998) extracted a clump mass function from observations of the ρ Ophiuchi main cloud and were the first to note the similarity to the stellar IMF. Alves et al. (2007) suggested that the stellar IMF is a direct result of the CMF and that there exists a one-to-one correspondence. This assumption has largely been adopted as the explanation for the resemblance of the two mass distributions. However, many are now questioning whether this IMF is universal across all star-forming regions and if the CMF has a direct one-to-one correspondence with the IMF (e.g. Reid et al., 2010; Anathpindika, 2011; Swift & Williams, 2008; Smith et al., 2008). Reid et al. (2010) showed that the lognormal form of the CMF may simply be due to many independently-acting random processes and urged that great care must be taken when interpreting the CMF and comparing it to the stellar IMF.

Alternatively, it has been suggested that the shape of the CMF and IMF could be related to supersonic turbulence observed in molecular clouds (Padoan & Nordlund, 2002; Hennebelle & Chabrier, 2008). For this argument, the observed lognormal form of the IMF is a result of the hierarchical structure in molecular clouds and the formation of dense cores by turbulent fragmentation.

The origin of the stellar IMF is still much of a mystery and is one of the least understood aspects of astronomy today. Since stars form from dense cores, understanding the CMF and the formation of molecular cloud cores can lead to a better understanding of the earliest stages of star formation. The origin of the stellar IMF and its relationship to the CMF is perhaps the most important question to be answered by the theory of star formation.

2.3 Smoothed Particle Hydrodynamics

Smoothed particle hydrodynamics (SPH) is a computational technique used to model fluid flows wherein any physical function is expressed by interpolating over a set of points where the function values are known (Lucy, 1977; Gingold & Monaghan, 1977). This set of points or ‘particles’ are used to model fluid elements, which follow the flow of the gas. SPH is an extension of N-body methods with very large N and includes a finite pressure term and artificial viscosity to correctly model shocks. SPH codes solve the Euler equations using the Lagrangian formulation of hydrodynamics. The approach is considered Lagrangian as it defines the Euler equations in comoving coordinates and it solves for the derivatives of the physical quantities using the derivatives of the kernel function (Hernquist & Katz, 1989). Neighbouring particles are weighted by a smoothing kernel and local summations provide the local properties of the fluid.

The kernel converts the particle information into a smoothed estimate where the density gradually increases and the profile has a characteristic width, h , which is the smoothing length. The smoothing kernel can be as simple as a Gaussian for one-dimension. The smoothing kernel for three-dimensions which is often used in practice is based on spline functions (Monaghan & Lattanzio, 1985) and is defined by the kernel function:

$$W(\mathbf{r}, h) = \frac{1}{\pi h^3} \begin{cases} 1 - \frac{3}{2}q^2 + \frac{3}{4}q^3 & : 0 \leq q < 1, \\ \frac{1}{4}(2 - q)^3 & : 1 \leq q < 2, \\ 0 & : \text{otherwise} \end{cases}$$

where $q = r/h$. The advantage of using this smoothing kernel is that the errors from approximations are small and particle disorder is limited by the continuity of the second derivative (Monaghan, 1992; Bodenheimer et al., 2007). Using a smoothing kernel that covers a finite volume (goes to zero for $r > 2h$) results in a given particle interacting with only a subset of its neighbours. By limiting the number of interactions to include only non-negligible contributions to the computation, the computational efficiency of the calculations are greatly improved. The kernel function has been plotted in Figure 2.2 with a minimum smoothing length $h = 50$ AU. Any physical quantity, $A(\mathbf{r})$, associated with the gas, such as temperature or pressure, can be estimated using this kernel by a density-weighted interpolation between the known function values at the positions of the particles

$$A(\mathbf{r}) = \sum_i m_i \frac{A_i}{\rho_i} W(|\mathbf{r} - \mathbf{r}_i|, h)$$

where \mathbf{r} is the position of particle i and $\frac{\rho_i}{m_i}$ is the number of particles per unit volume.

One way to calculate the gravitational forces is to use a tree-solving method. For a given particle i , any particle with a kernel which is within a sphere of radius $2h_i$ around particle i is considered that particle's neighbour. By recording each particle's nearest neighbours within the tree, the computation is optimized, as forces are only calculated between neighbouring particles rather than between all particles. Gravitational softening is introduced to smooth the gravitational potential and forces. This helps to approximate a continuous density distribution from a system of N bodies.

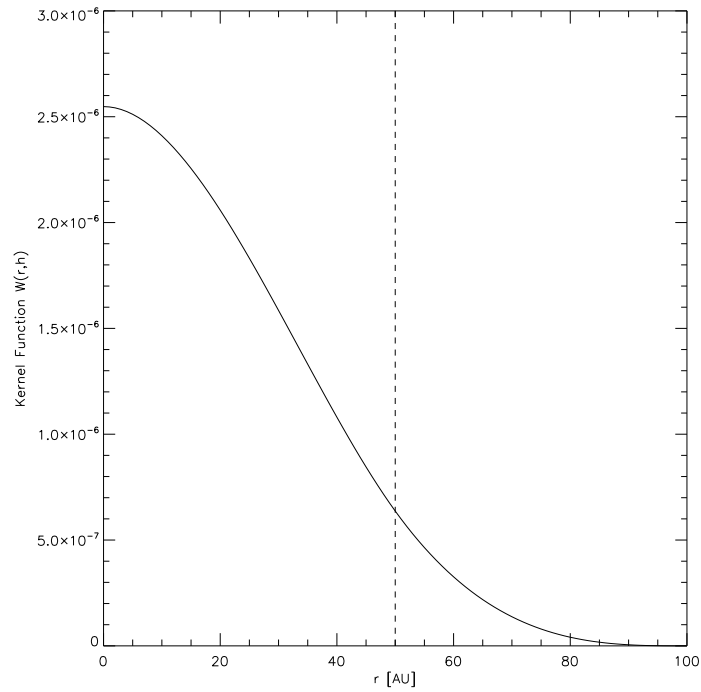


Figure 2.2: Kernel function, $W(r,h)$, with a minimum smoothing length of $h = 50$ AU.

The Truelove et al. (1997) criterion states that in order to avoid artificial fragmentation in an SPH code, one must resolve the Jeans mass and Jeans length. All scales larger than these values are unstable to gravitational collapse. Bate & Burkert (1997) specifically state that for SPH codes, the Jeans mass should be resolved by more than twice the number of neighbouring particles.

There are several advantages to SPH codes. These codes conserve the physical quantities of total energy and total linear and angular momenta, provided artificial viscosity is implemented, and are also able to adaptively resolve the fluid. As the density of the fluid increases, the smoothing length decreases which naturally improves the resolution. SPH codes are also excellent at handling dynamic astrophysical systems, such as collapse due to self-gravity (Bodenheimer et al., 2007).

2.4 Summary

In this chapter, we have provided a detailed description of the characteristics and dynamics of molecular clouds, clumps and cores. In particular, turbulence is especially significant in the earliest stages of star formation by influencing the formation of substructure in giant molecular clouds. GMC dynamics can be best summarized using Larson's three laws, one of which states that all GMCs are gravitationally bound and in virial equilibrium. Observational tests to determine whether star-forming clumps or cores are gravitationally bound often rely on the virial parameter, which is related to the kinetic and gravitational potential energies of the gas. The virial parameter will be

discussed in greater detail in Chapter 4 as we apply its test of boundedness to studies of our own.

Dust continuum and molecular line (eg. ^{12}CO (1-0), NH_3 (1,1)) observations of nearby star-forming regions have improved our understanding of how stars form in clustered environments. Current observations have seen molecular clouds which are highly filamentary in structure. It is believed that this morphology, which is also seen in theoretical simulations, is related to turbulence and may have a significant role in star formation. Smoothed particle hydrodynamics codes are often used to perform these types of molecular cloud collapse simulations, as SPH excels at handling astrophysical systems involving self-gravity.

The earliest stage of star formation is critical to our understanding of the transition from diffuse interstellar gas to dense molecular clouds, clumps, and cores. The dense molecular cores are the precursors to stars and, by studying these cores, we can learn more about the initial conditions of star formation, including the origin of the stellar initial mass function.

Bibliography

Alves, J., Lombardi, M. & Lada, C. J. 2007, *A&A*, 462, L17

Anathpindika, S. 2011, *New Astronomy*, 16, 477

André, P., Men'shchikov, A., Bontemps, S., Könyves, V., Motte, F., Schneider, N., Didelon, P., Minier, V., Saraceno, P., Ward-Thompson, D., Di Francesco, J., White, G., Molinari, S., Testi, L., Abergel, A., Griffin, M., Henning, T., Royer, P., Merín, B., Vavrek, R., Attard, M., Arzoumanian, D., Wilson, C. D., Ade, P., Aussel, H., Baluteau, J.-P., Benedettini, M., Bernard, J.-P., Blommaert, J. A. D. L., Cambrésy, L., Cox, P., di Giorgio, A., Hargrave, P., Hennemann, M., Huang, M., Kirk, J., Krause, O., Launhardt, R., Leeks, S., Le Penec, J., Li, J. Z., Martin, P. G., Maury, A., Olofsson, G., Omont, A., Peretto, N., Pezzuto, S., Prusti, T., Roussel, H., Russeil, D., Sauvage, M., Sibthorpe, B., Sicilia-Aguilar, A., Spinoglio, L., Waelkens, C., Woodcraft, A., & Zavagno, A. 2010, *A&A*, 518, 102

Ballesteros-Paredes, J., Klessen, R. S., Mac Low, M.-M., Vázquez-Semadeni, E. 2007. Molecular Cloud Turbulence and Star Formation. In *Protostars and Planets V*, eds. B. Reipurth, D. Jewitt, and K. Keil (Tucson: University of Arizona Press), pp.63-80

Bate, M. R. & Burkert, A. 1997, *MNRAS*, 288, 1060

Bergin, E. A. & Langer, W. D. 1997, *ApJ*, 486, 316

Bergin, E. A. & Tafalla, M. 2007, ARA&A, 45, 339

Bertoldi, F. & McKee, C. F. 1992, ApJ, 395, 140

Bodenheimer, P., Laughlin, G. P., Różyczka, M., & Yorke, H. W. 2007, *Numerical Methods in Astrophysics: An Introduction*, (New York: Taylor & Francis Group)

Caselli, P., Walmsley, C. M., Zucconi, A., Tafalla, M., Dore, L., & Myers, P. C. 2002a, ApJ, 565, 331

Caselli, P., Benson, P. J., Myers, P. C., & Tafalla, M. 2002c, ApJ, 572, 238

Chabrier, G. 2003, PASP, 115, 763

Di Francesco, J., Evans, II, N. J., Caselli, P., Myers, P. C., Shirley, Y., Aikawa, Y., & Tafalla, M. 2007. An Observational Perspective of Low-Mass Dense Cores I: Internal Physical and Chemical Properties. In *Protostars and Planets V*, eds. B. Reipurth, D. Jewitt, and K. Keil (Tucson: University of Arizona Press), pp.17-32

Dib, S., Kim, J., Vázquez-Semadeni, E., Burkert, A., & Shadmehri, M. 2007, ApJ, 661, 262

Elmegreen, B. G. & Scalo, J. 2004, ARA&A, 42, 211

Falgarone, E., Panis, J. -F., Heithausen, A., Perault, M., Stutzki, J., Puget, J. -L., & Bensch, F. 1998, A&A, 331, 669

Gammie, C. F., Lin, Y.-T., Stone, J. M., & Ostriker, E. C. 2003, ApJ, 592, 203

- Gingold, R. A. & Monaghan, J. J. 1977, MNRAS, 181, 375
- Heithausen, A. & Thaddeus, P. 1990, ApJ, 353, 49
- Henkel, C. & Wiklind, T. 1997, Space Sci. Rev., 81, 1
- Hennebelle, P. & Chabrier, G. 2008, ApJ, 684, 395
- Hernquist, L. & Katz, N. 1989, ApJS, 70, 419
- Heyer, M. H., Carpenter, J. M., & Snell, R. L. 2001, ApJ, 551, 852
- Hildebrand, R. H. 1983, QJRAS, 24, 267
- Johnstone, D., Wilson, C. D., Moriarty-Schieven, G., Joncas, G., Smith, G., Gregersen, E., & Fich, M. 2000, ApJ, 545, 327
- Johnstone, D. & Bally, J. 1999, ApJ, 510, 49
- Kirk, H., Johnstone, D., & Di Francesco, J. 2006, ApJ, 646, 1009
- Klein, R. I., Inutsuka, S.-I., Padoan, P., & Tomisaka, K. 2007. Current Advances in the Methodology and Computational Simulation of the Formation of Low-Mass Stars. In *Protostars and Planets V*, eds. B. Reipurth, D. Jewitt, and K. Keil (Tucson: University of Arizona Press), pp. 99-116
- Kroupa, P. 2001, MNRAS, 322, 231
- Krumholz, M. R. & McKee, C. F. 2005, ApJ, 630, 250
- Lada, C. J. & Lada, E. A. 2003, ARA&A, 41, 57
- Langer, W. D., Wilson, R. W., Goldsmith, P. F., & Beichman, C. A. 1989, ApJ, 337, 355

Larson, R. B. 1981, MNRAS, 194, 809

Larson, R. B. 2003, Rep. Prog. Phys., 66, 1651

Lucy, L. B. 1977, AJ, 82, 1013

Mac Low, M.-M. & Klessen, R. S. 2004, Rev. Mod. Phys., 76, 125

Matzner, C. D. & McKee, C. F. 2000, ApJ, 545, 364

Men'shchikov, A., André, P., Didelon, P., Könyves, V., Schneider, N., Motte, F., Bontemps, S., Arzoumanian, D., Attard, M., Abergel, A., Baluteau, J.-P., Bernard, J.-P., Cambrésy, L., Cox, P., di Francesco, J., di Giorgio, A. M., Griffin, M., Hargrave, P., Huang, M., Kirk, J., Li, J. Z., Martin, P., Minier, V., Miville-Deschênes, M.-A., Molinari, S., Olofsson, G., Pezzuto, S., Roussel, H., Russeil, D., Saraceno, P., Sauvage, M., Sibthorpe, B., Spinoglio, L., Testi, L., Ward-Thompson, D., White, G., Wilson, C. D., Woodcraft, A., & Zavagno, A. 2010, A&A, 518, 103

Miller, G. & Scalo, J. 1979, ApJS, 41, 513

Miville-Deschênes, M.-A., Martin, P. G., Abergel, A., Bernard, J.-P., Boulanger, F., Lagache, G., Anderson, L. D., André, P., Arab, H., Baluteau, J.-P., Blagrove, K., Bontemps, S., Cohen, M., Compiègne, M., Cox, P., Dartois, E., Davis, G., Emery, R., Fulton, T., Gry, C., Habart, E., Huang, M., Joblin, C., Jones, S. C., Kirk, J., Lim, T., Madden, S., Makiwa, G., Menshchikov, A., Molinari, S., Moseley, H., Motte, F., Naylor, D. A., Okumura, K., Pinheiro Gonçalves, D., Polehampton, E., Rodón, J. A., Rus-

- seil, D., Saraceno, P., Schneider, N., Sidher, S., Spencer, L., Swinyard, B., Ward-Thompson, D., White, G. J., & Zavagno, A. 2010, *A&A*, 518, 104
- Monaghan, J. J. 1992, *ARA&A*, 30, 543
- Monaghan, J. J. and Lattanzio, J. C. 1985, *A&A*, 149, 135
- Motte, F., André, P., & Neri, R. 1998, *A&A*, 336, 150
- Myers, P. C. 1999, *The Physics and Chemistry of the Interstellar Medium, Proceedings of the 3rd Cologne-Zermatt Symposium*, Eds.: V. Ossenkopf, J. Stutzki, and G. Winnewisser, GCA-Verlag Herdecke, 227
- Onishi, T., Mizuno, A., Kawamura, A., Ogawa, H., & Fukui, Y. 1998, *ApJ*, 502, 296
- Ossenkopf, V. & Henning, Th. 1994, *A&A*, 291, 943
- Padoan, P. & Nordlund, A. 2002, *ApJ*, 576, 870
- Pagani, L., Pardo, J.-R., Apponi, A. J., Bacmann, A., & Cabrit, S. 2005, *A&A*, 429, 181
- Reid, M. A., Wadsley, J., Petitclerc, N., & Sills, A. 2010, *ApJ*, 719, 561
- Salpeter, E. E. 1955, *ApJ*, 121, 161
- Schmalzl, M., Kainulainen, J., Quanz, S. P., Alves, J., Goodman, A. A., Henning, T., Launhardt, R., Pineda, J. E., & Román-Zúñiga, C. G. 2010, *ApJ*, 725, 1327
- Simpson, R. J., Nutter, D., & Ward-Thompson, D. 2008, *MNRAS*, 391, 205

- Smith, R. J., Clark, P. C., & Bonnell, I. A. 2008, MNRAS, 391, 1091
- Solomon, P. M., Rivolo, R., Barrett, J., & Yahil, A. 1987, ApJ, 319, 730
- Stahler, S. W. & Palla, F. 2004. *The Formation of Stars*, Wiley-VCH
- Swift, J. J. & Williams, J. P. 2008, ApJ, 679, 552
- Tachihara, K., Onishi, T., Mizuno, A., & Fukui, Y. 2002, A&A, 385, 909
- Tielens, A. G. G. M. 2005. *The Physics and Chemistry of the Interstellar Medium*, Cambridge University Press
- Truelove, J. K., Klein, R. I., McKee, C. F., Holliman, J. H., Howell, L. H., & Greenough, J. A. 1997, ApJL, 489, L179
- Ward-Thompson, D., Kirk, J. M., André, P., Saraceno, P., Didelon, P., Könyves, V., Schneider, N., Abergel, A., Baluteau, J.-P., Bernard, J.-P., Bontemps, S., Cambrésy, L., Cox, P., di Francesco, J., di Giorgio, A. M., Griffin, M., Hargrave, P., Huang, M., Li, J. Z., Martin, P., Men'shchikov, A., Minier, V., Molinari, S., Motte, F., Olofsson, G., Pezzuto, S., Russeil, D., Sauvage, M., Sibthorpe, B., Spinoglio, L., Testi, L., White, G., Wilson, C., Woodcraft, A., & Zavagno, A. 2010, A&A, 518, 92
- Ward-Thompson, D., André, P., Crutcher, R., Johnstone, D., Onishi, T., & Wilson, C. 2007. An Observational Perspective of Low-Mass Dense Cores II: Evolution Toward the Initial Mass Function. In *Protostars and Planets V*, eds. B. Reipurth, D. Jewitt, and K. Keil (Tucson: University of Arizona Press), pp. 33-46

M.Sc. Thesis — Rachel Louise Ward — McMaster University - Physics and Astronomy — 2011

Williams, J. P., Blitz, L., & McKee, C. F. 2000, *Protostars and Planets IV*, 97

Williams, J. P. & McKee, C. F. 1997, *ApJ*, 476, 166

Wilson, R. W., Jefferts, K. B., & Penzias, A. A. / 1970, *ApJ*, 161, 43

Young, J. S. & Scoville, N. Z. 1991, *ARA&A*, 29, 581

Chapter 3

Viewing the Simulation through the Observer's Eyes

3.1 Introduction

In this chapter, we will give a brief overview of the simulation completed by Petitclerc (2009) which is the basis for this work. We will then describe the methods used to produce synthetic observations from the simulation. Synthetic observations provide a way of determining the effects of projection and studying various biases which may result from the use of common observer's tools and techniques. We have created synthetic observations from the simulation for several different cases, including for various orientations, output times, resolutions, and collapse cases. Since we have access to the simulation, we are able to “observe” line-of-sight properties, as well as the true three-dimensional properties of the molecular cloud.

3.2 The Simulation

Our group has previously simulated star formation in molecular clouds using the smoothed particle hydrodynamics (SPH) code, GASOLINE (Wadsley et al., 2004). We modelled the isothermal collapse of a $5000 M_{\odot}$ giant molecular cloud, initially 8 pc across, using approximately 36 million particles. These simulations were run by Nicolas Petitclerc using dedicated resources from SHARCNET, and formed the basis of his PhD thesis (Petitclerc, 2009) and subsequent work (Reid et al., 2010; Wadsley et al., 2011). The cloud is initially a sphere with uniform density of 300 cm^{-3} and it reaches a maximum density of approximately $10^{-15} \text{ g cm}^{-3}$ (or $\sim 10^8 \text{ cm}^{-3}$) by the simulation stopping point. We use a polytropic equation of state, which describes the dependence of pressure on density, to model the thermal behaviour of the gas. The equation of state from Bate & Bonnell (2005) is

$$P = \kappa \rho^{\eta} \quad \eta = \begin{cases} 1. & \rho \leq 10^{-13} \text{ g cm}^{-3}, \\ 7/5 & \rho > 10^{-13} \text{ g cm}^{-3} \end{cases}$$

where κ is defined as $\kappa = c_s^2$ for an isothermal gas with the sound speed $c_s = 1.84 \times 10^4 \text{ cm s}^{-1}$ at 10 K and η is the polytropic exponent. We have chosen this equation of state, as it mimics the behaviour of temperature and density seen in spherically-symmetric collapses of molecular clouds using radiative transfer (Bate et al., 2003).

The value of $10^{-13} \text{ g cm}^{-3}$ in this equation of state is taken to be the opacity limit for fragmentation (Bate et al., 2003; Bate & Bonnell, 2005). Once the opacity limit is reached, the gas becomes optically thick, allowing very little flux through the material; fragmentation of objects is suppressed

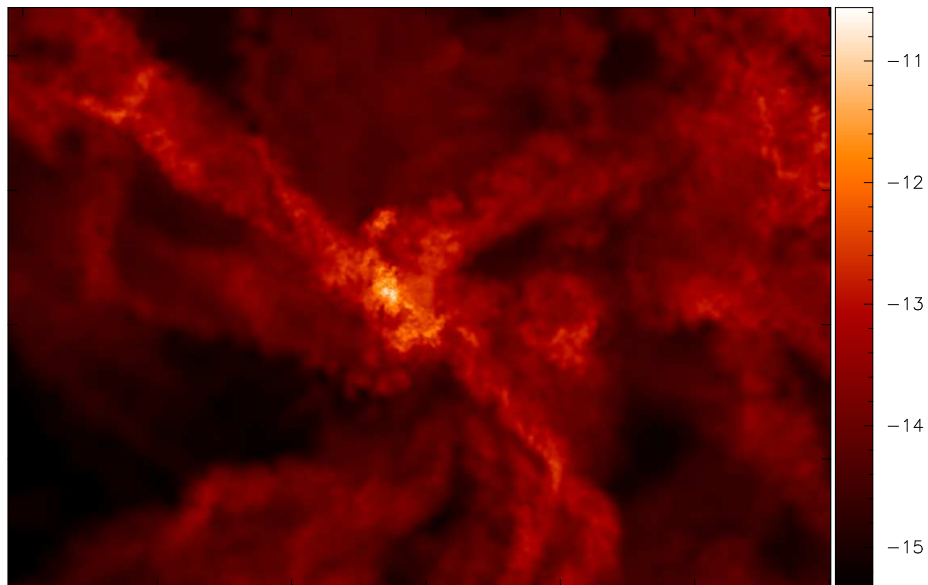


Figure 3.1: Visualisation of our simulation made using SPLASH (Price, 2007) of a dense core of gas forming in a molecular cloud collapse simulation. The colour scale shows density in units of M_{\odot}/AU^3 ($\approx 10^{17} \text{ cm}^{-3}$). The region shown is 1.5 pc by 1 pc in size, where, for comparison, a typical clump can be of order 1 pc in size and a typical core can be of order 0.1 pc in size.

Table 3.1: Initial conditions of the SPH simulation of a giant molecular cloud

Mass	5000 M_{\odot}
Particles	36 088 472
Diameter	8 pc
Initial uniform density	300 cm^{-3}
Particle mass	$1.3855 \times 10^{-4} M_{\odot}$
Free-fall time	1.9 Myr
Temperature	10 K
Minimum Jeans mass	0.01 M_{\odot}
Minimum smoothing length	50 AU
Minimum spatial resolution	100 AU

and heating of the molecular gas will begin. Since our maximum density is well below this density limit of $10^{-13} \text{ g cm}^{-3}$, the isothermal approximation of 10 K and the assumption that the emission is optically thin are justified. Our simulations were evolved for ~ 1.35 million years – 70 percent of the 1.9 Myr free-fall time ($t_{ff} = \sqrt{3\pi/32G\rho_{init}}$). Therefore, we are focussing on the earliest stages of star formation before adiabatic heating and stellar feedback become important. These simulations had open boundary conditions, unlike the periodic boxes that are commonly used (Klessen, 2001), allowing us to simulate an entire molecular cloud undergoing gravitational collapse, rather than just a small portion within it. Other simulations have tended to focus solely on sub-regions within the clouds with masses only reaching as high as 100 solar masses (e.g. Bate, 2009; Smith et al., 2008; Tilley & Pudritz, 2004). However, in order to more accurately represent what is seen in observations, it is necessary to move to larger scales. It is remarkable that the norm in computational star formation seems to be to run simulations with atypically low masses, making it difficult to connect theory to observations under these

conditions. Bate and coworkers (e.g. Bate, 2009) have run some of the most state-of-the-art computational simulations of star formation; however, their ‘giant’ molecular clouds are only 500 solar masses at most, which is the typical size of a single clump seen in observations (Bergin & Tafalla, 2007). It is therefore vital that simulations of star formation move to much larger scales than previously considered. The key specifications of the simulation are listed in Table 3.1.

GASOLINE is capable of achieving very high spatial resolution. Previous runs have shown that our molecular cloud collapse simulations can have a minimum spatial resolution of 100 AU, allowing us to compare them with confidence to observations of molecular clouds, which, at their most resolved, can have a resolution of ~ 1000 AU. The Perseus Molecular Cloud, at a distance of 240 pc (Lada et al., 2009), has been observed at a resolution of 1500 AU using the Spitzer Space Telescope (Jørgensen et al., 2007) and also at a resolution of 1200 AU using the Owens Valley Radio Observatory (OVRO) by Olmi et al. (2005). More nearby molecular clouds such as the ρ Ophiuchus cloud complex or the Taurus-Auriga molecular cloud at ~ 140 pc can be resolved in the far-IR using Herschel ($17''$ at $250\mu\text{m}$), which can probe spatial scales down to ~ 2000 AU (André & Saraceno, 2005). ALMA will be able to achieve an incredibly high angular resolution of $\sim 0.01''$, making it possible to resolve objects with a radius of 10 AU or less in clouds less than 0.2 kpc away (van Dishoeck & Jørgensen, 2008; Fukui, 2005).

An important component in these simulations is determining an appropriate initial velocity structure of the cloud, with important implications for

the subsequent shape. Our simulations were run for four different initial anisotropic velocity fields: spherical, ribbon, filament, and sheet collapse cases. These velocity fields differ in the direction of the largest-scale velocity modes of the turbulence – inward or outwards – along the principle axis of the simulations. To generate more realistic cloud collapse, these large scale turbulent velocity modes were included in the initial conditions on scales larger than the entire cloud. The large-scale compressive modes which produce molecular clouds can greatly affect the morphology of the cloud (Ballesteros-Paredes et al., 2007). Recent studies (Schmalzl et al., 2010; Men’shchikov et al., 2010) have shown that filaments are very common in molecular clouds and may have a significant role in star formation. Dense cores have been observed by Herschel to be embedded in the filamentary structure of the cloud (Men’shchikov et al., 2010). Filaments are created when material is pushed inwards in two dimensions, creating a string-like shape. Additionally, supernovae explosions are also inferred to trigger star formation (Larson, 2003), as the pressure of the expanding wave can cause localized regions to become overdense and collapse into stars along the shock front, which would produce a sheet – flattened in one dimension but large in the other two. Petitclerc (2009) determined that the case that was statistically most likely was the ribbon, in which material along one axis is driven to the centre of the cloud, material along another axis is pushed outwards, and the third is static (which can appear observationally similar to a filament).

In this thesis, we concentrate on the idealised spherical collapse case, where a sphere of uniform density undergoes gravitational collapse to form dense cores in the molecular cloud. For the purpose of studying the effects of pro-

jection and biases in the clump-finding algorithms on different types of observations (see Section 4.1), the turbulent structure of the cloud is not significant. The nature of the cloud collapse becomes important when studying the boundedness of the clumps. We analyse the ribbon, filament, and sheet collapse cases to make specific comparisons with the spherical case to learn about the importance of initial geometry.

3.3 Synthetic Observations

In order to compare the results of the simulation with observations, we have created synthetic observations by producing a ‘three-dimensional’ (position-position-velocity or ‘PPV’) spectral-line data cube and a two-dimensional (position-position or ‘PP’) column density map. As discussed in Chapter 2, column density maps and spectral-line data cubes are the most useful types of observations for the study of star formation. These data are a more realistic representation of observations, as observers can never know the physical position of an object along the line of sight. The synthetic observations were made using the library of routines, CFITSIO¹, to write the simulation output in the FITS (Flexible Image Transport System) format. The FITS format is very often the format of observations; thus, the conversion of our outputs to this format allowed for the use of standard observer’s tools to analyse our data.

To create the two-dimensional (PP) column density map, the projection was produced from our simulation by integrating the density along the line of

¹ Made available to the public at <http://heasarc.gsfc.nasa.gov/fitsio/>

sight (LOS) and mapping the particles from the simulation to grid cells on a plane. The column density, N , is given by

$$N = \int n \, dl$$

where n is the density as a function of the height of the column and dl is the path length along the LOS.

As mentioned in Chapter 2, any physical quantity associated with the gas can be estimated by interpolating between the function values at the known positions of the particles. Since each particle represents a density distribution, the interpolations are density-weighted. For the creation of simulated observations, one option would be to interpolate the particles to a full position-position-position (PPP) grid to obtain a 3D smoothed representative mapping of the gas in the simulation. However, it is rather intensive to interpolate the particles to a PPP grid and then collapse that mapping to a projection. Instead, we chose to first integrate the spherically symmetric SPH smoothing kernel along the line of sight and interpolate from the resultant two-dimensional kernel (Smith et al., 2008). Each particle has a smoothing kernel and the particle mass is divided up into grid cells by their specific weights (Figure 3.2). For each line of sight the smoothed particle distribution intersects, the particle distance from the line of sight is calculated. If that distance is less than twice the smoothing length, a contribution from that particle is added to that line of sight. The weighting determines what fraction of the particle mass will contribute to a line of sight. The sum of the kernel weights is normalized to ensure the total mass of the particle is counted only once. The diameter of the i th particle in grid units, h_i , is twice the smoothing length. If the size of

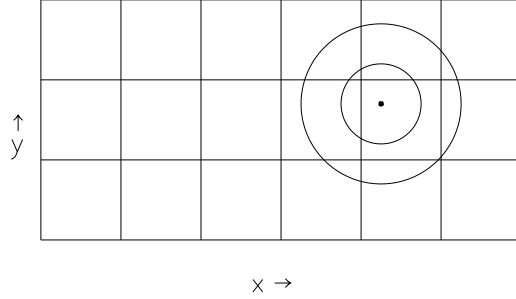


Figure 3.2: The line of sight column density was divided up along a grid with the particle mass divided by the kernel weights. The lines of sight are taken to be the vertices where the grid intersects.

the particle carries it off the edge of the grid, it is assigned to the edge of the grid and if there are no lines of sight intersecting the smoothing sphere, the particle weight will be assigned to the nearest line of sight.

The most dense gas in the simulation is $10^{-11} M_{\odot} \text{ AU}^{-3}$ or $\sim 10^6$ atoms cm^{-3} and the background of the simulation, quantified as the “noise” by measurements of off-source regions, has a density of $10^{-18} M_{\odot} \text{ AU}^{-3}$ or ~ 1 -2 atoms cm^{-3} . This is consistent with our definition of a dense core, as well as with the typical background ISM density, which averages around 1 atom cm^{-3} . Our synthetic observations are in units of solar mass per pixel. For a synthetic column density map with a resolution of 6000 AU/pixel, the densest gas would correspond to a column density of $\sim 1 M_{\odot}/\text{pixel}$ or 10^{23} cm^{-2} . These peak values are comparable to estimates from real observations, as starless cores have been observed to have typical column densities $< 10^{23} \text{ cm}^{-2}$ (Caselli et al., 2002a).

The spatial resolution of a 500 x 500 grid is 6000 AU/pixel using a map size of 3.0×10^6 AU per side. The two-dimensional column density map produced can be seen in Figure 3.3. To better reproduce an observation of a molecular cloud, the resolution was initially chosen to be comparable to that of an observation of the active Orion star-forming region using the Submillimetre Common-User Bolometer Array 2 (SCUBA-2 Holland et al., 2003, 2006) instrument on the James Clerk Maxwell Telescope (JCMT). The SCUBA-2 instrument is expected to perform with an angular resolution of 14" while operating at a wavelength of 850 μm (MacKenzie et al., 2011). The Orion cloud complex is at a distance of approximately 450 pc (Genzel & Stutzki, 1989) and, for this distance, our spatial resolution corresponds to an angular resolution on the sky of 13.3"/pixel.

In radio and sub-millimetre observations, the beam is the minimum angular resolution of the telescope on the sky. The beam defines the resolution, because all of the flux within the beam size is included, limiting the sensitivity of observations. Convolution of an observation can smooth an image to a specified resolution. Images are often convolved with a Gaussian to represent the beam profile. The full-width-half-maximum (FWHM) of the Gaussian profile determines how much or how little the image is smoothed. Rather than smoothing our maps with a Gaussian, we are able to specify the desired resolution when the column density map is initially created. An observation of Orion at 850 μm using SCUBA-2 on the JCMT with a 14" beam size would correspond to a full-width-half-maximum (FWHM) of 1.05 pixels (or ~ 1 pixel) for the given spatial resolution of the image (6000 AU/pixel). Thus, the spatial resolution

of 6000 AU/pixel that we have selected is representative of an observation of a molecular cloud at the distance of the Orion cloud complex.

A higher resolution column density map was also produced to use as a demonstration of the robustness of our method (see Figure 3.4). The spatial resolution of the 1250 x 1250 grid is 2000 AU/pixel using a map size of 2.5×10^6 AU per side. This resolution was initially chosen to be comparable to that of an observation of the ρ Ophiuchus star-forming region using SCUBA-2 on the JCMT. The ρ Ophiuchus star-forming region is at a distance of approximately 160 pc (Motte et al. 1998). For this distance, our spatial resolution corresponds to an angular resolution on the sky of $12.5''$ /pixel (compared to the minimum angular resolution on the sky of $14''$ for SCUBA-2). We once again consider the FWHM of the beam and it is determined to be 1.1 pixels (or ~ 1 pixel) for the given spatial resolution of the image (2000 AU/pixel). By comparison, the resolution of an observation of ρ Ophiuchus would be 2240 AU/pixel. Thus, our chosen spatial resolution of 2000 AU/pixel is a representative example of an observation of a molecular cloud at the distance of the ρ Ophiuchus. Both of our synthetic observations are slightly more resolved than an actual observation, meaning that our results provide an upper limit on what is achievable by current cutting-edge telescopes and instruments. In particular, spatial scales of 2000 AU or ~ 0.01 pc are at the lower limit of what is currently attainable by the Herschel Space Observatory for observations of ρ Ophiuchus (André & Saraceno, 2005).

Submillimetre observations using spectral imaging systems, such as the HARP (Heterodyne Array Receiver Programme) and ACSIS (AutoCorrela-

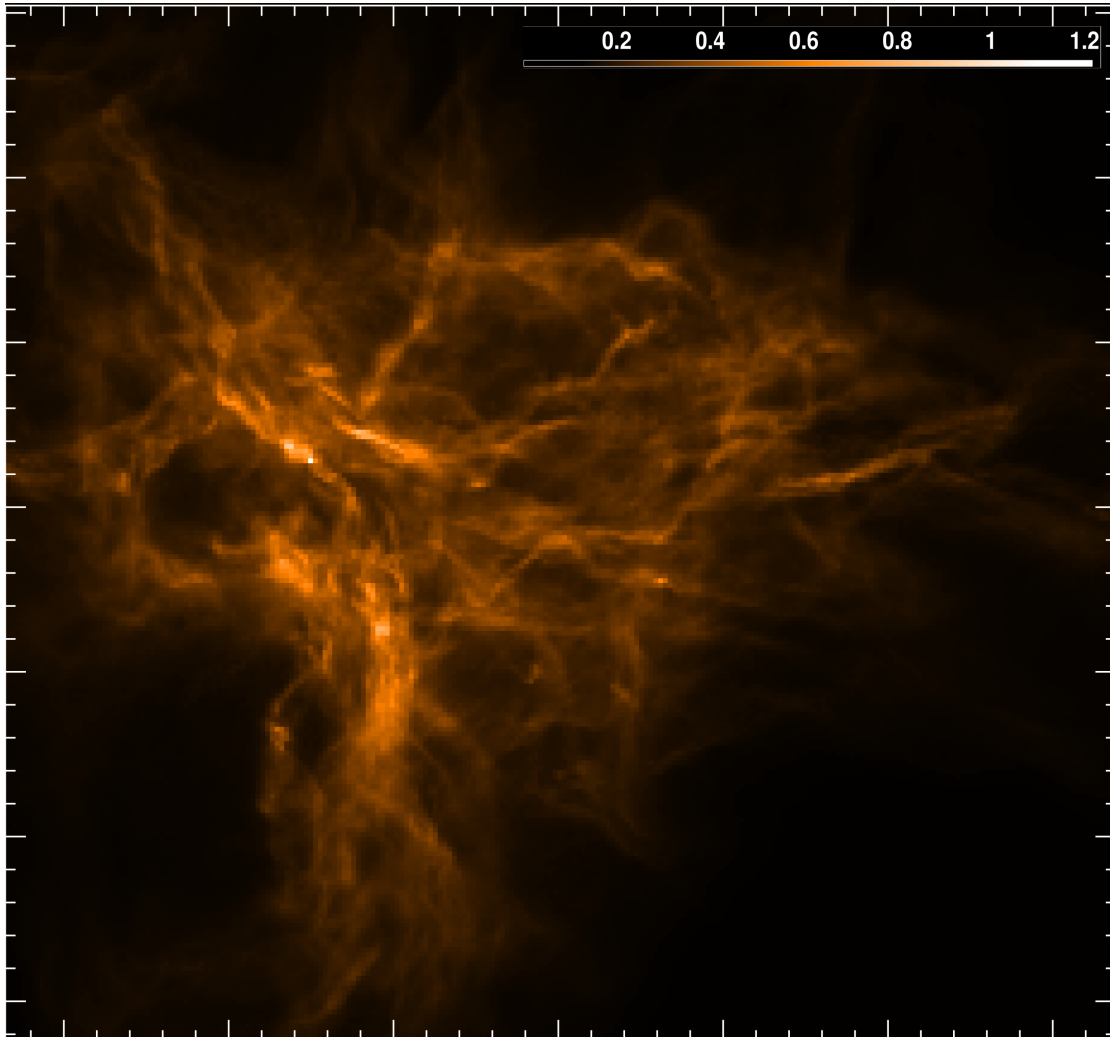


Figure 3.3: Two-dimensional column density map of spherical molecular cloud collapse. The resolution of the map is 6000 AU/pixel with projection along the z-axis onto a 500 x 500 grid. Note the filamentary structure comparable to that seen in observations. The column density is in units of solar mass per pixel.

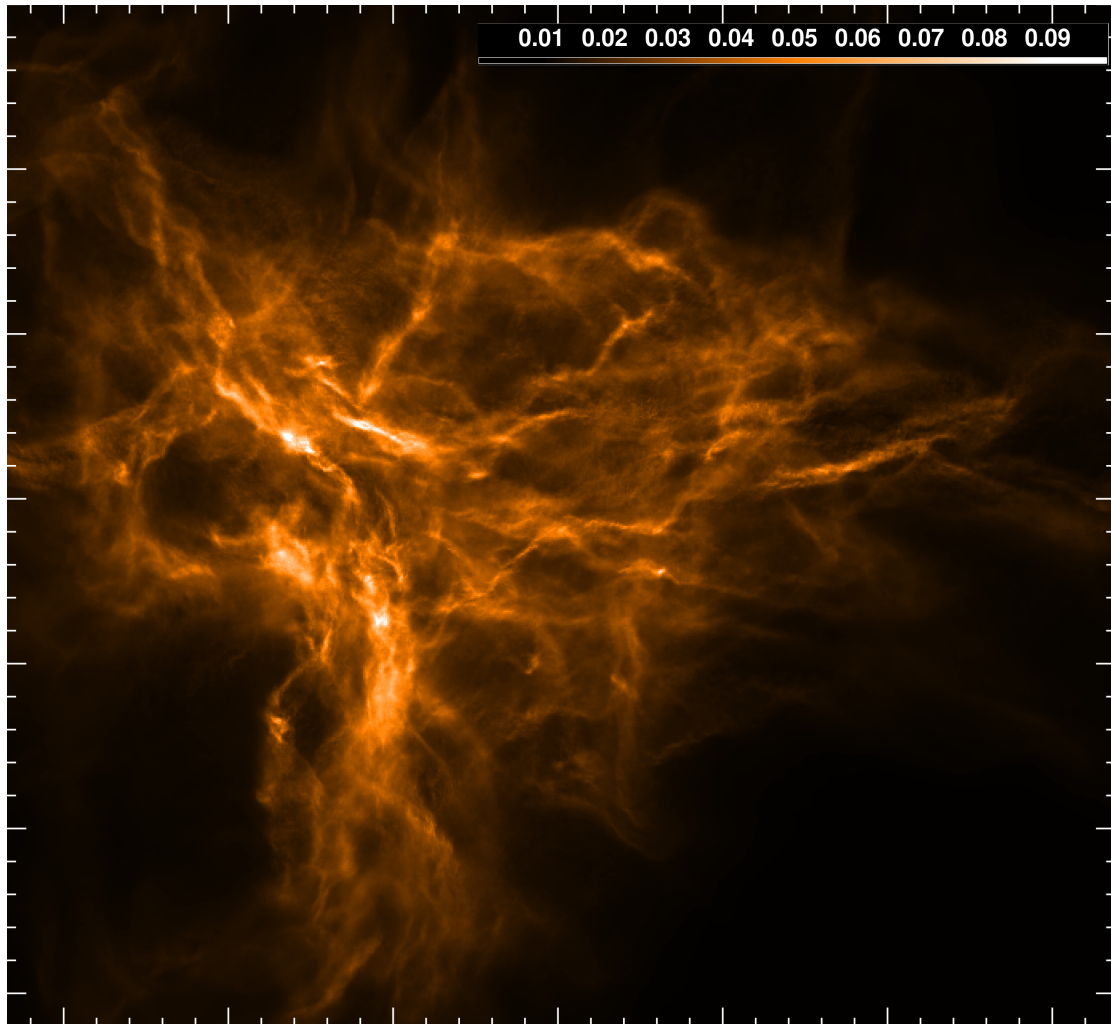


Figure 3.4: Higher resolution two-dimensional column density map of spherical molecular cloud collapse. The resolution of the map is 2000 AU/pixel with projection along the z -axis onto a 1250 x 1250 grid. The column density is in units of solar mass per pixel.

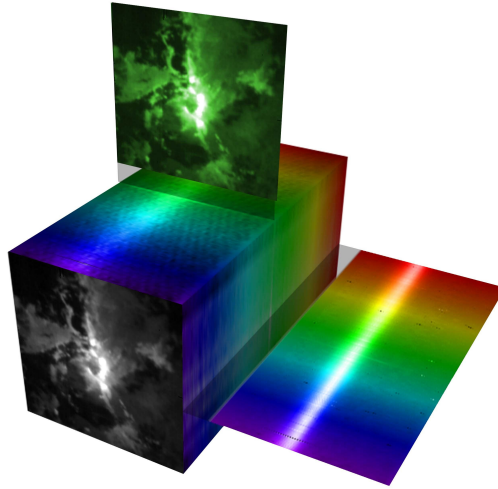


Figure 3.5: Visualisation provided by the Joint Astronomy Centre (JAC – <http://outreach.jach.hawaii.edu>) of a spectral-line data cube. The third dimension traces the velocity of the gas.

tion Spectrometer and Imaging System) instruments on the JCMT, allow astronomers to record a third dimension. This third dimension is not a spatial dimension, but rather it traces the motion of the gas along the line of sight. These systems can produce images at various wavelengths to form a spectral-line data cube. Figure 3.5 shows a schematic of a data cube with two spatial dimensions and one wavelength dimension. The wavelength or frequency dimension can trace molecular line emission and provide information of the velocity of the gas towards and away from us. When the cube is collapsed, the emission is combined to show the total intensity of the object, but we are also able to look at a single slice of the cube for a given wavelength or look at the spectra across the entire object.

To create the ‘three-dimensional’ (PPV) spectral-line data cube, we use the velocities of the particles to simulate the motion of the gas along the third dimension. The synthetic PPV spectral-line cube was produced by dividing up the intrinsic velocity of each of the particles along the line of sight, v_z . For each particle, the contribution was added to the appropriate velocity bins (or channels) for all lines of sight the particle intersects. This produces infinitely sharp ‘spectral lines’. For a given velocity channel, each contributing particle mass in that bin is divided up into grid cells by their specific weights. This method to obtain the column density per velocity channel is very similar to the method used to create the PP column density maps. Combining each ‘frame’ of column density per velocity channel results in a cube with two spatial dimensions and one velocity dimension and the PPV cube was normalized to contain a total mass of $5000 M_\odot$ to ensure that the total mass of each particle was counted only once.

Our aim is to model molecular line emission along the line of sight; therefore, we require a molecular tracer to simulate the spectral-line emission. We have chosen the NH_3 (1,1) transition as our molecular line tracer, as we recall from Chapter 2 that NH_3 is an excellent tracer of dense cores, as it is present at very high densities. Since actual molecular lines are not infinitely sharp and have a finite width, we must introduce a method to broaden our lines. We have chosen to use Doppler broadening as the mechanism by which we determine our line shape.

Doppler broadening is a result of thermal motions of the particles. The frequency of the line emission in the rest-frame of a moving particle, ν_0 , will differ

from the frequency of the emission of that particle detected by an observer, ν . Since Doppler broadening depends on the frequency of the spectral line, it is useful to express the third dimension of the cube as a frequency dimension instead of a velocity dimension. We determined the change in frequency from the v_z velocity component of the particles using the following formula:

$$\nu - \nu_0 = \frac{\nu_0 v_z}{c}$$

where ν_0 is the rest-frame frequency of the NH_3 (1,1) line emission. The rest frequency depends on the velocity range (v_z to $v_z + \Delta v_z$) and frequency range (ν to $\nu + \Delta\nu$) where Δv_z is the width of the velocity bin and $\Delta\nu$ is the corresponding bin width in units of frequency. Our PPV cube is highly resolved with 148 velocity bins with a resolution of 0.04 km s^{-1} per bin, which corresponds to a 3.050 kHz channel separation for the NH_3 spectra. This was chosen such that it would approximately match that in the NH_3 observations of a dense core used by Pineda et al. (2010). The rest frequency can be written as:

$$\nu_0 = \frac{c\Delta\nu}{\Delta v_z}$$

In order to model the Doppler broadening of the NH_3 line emission, the probability that the line-of-sight velocity of a particle, v_z , will fall in a velocity bin of width Δv_z is represented by the line profile function of the strength of the emission

$$\phi(\nu) = P(\nu)d\nu = \frac{1}{\Delta\nu_D\sqrt{\pi}} \exp\left(-\frac{(\nu - \nu_0)^2}{\Delta\nu_D^2}\right)$$

The Doppler width, $\Delta\nu_D$, is determined by the normalization condition that $\int \phi(\nu)d\nu = 1$ where $\phi(\nu)$ is integrated over all space. The Doppler width is given by

$$\Delta\nu_D = \frac{\nu_0}{c} \sqrt{\frac{2kT}{m_a}}$$

where T is the temperature of the gas, m_a is the mass of the molecule, and ν_0 is the rest frequency of the molecule. Based on this definition of the Doppler width, it is evident that the line broadening only depends on the frequency of the line emission, the mass, and the temperature of the NH_3 molecule. To determine the Doppler width of our broadened lines, we used the temperature of the isothermal gas in our simulation (10 K) and the molecular mass of NH_3 ($17m_H$). Using our velocity bin width (0.04 km s^{-1}) and corresponding frequency channel separation (3.050 kHz), we obtained the rest frequency of NH_3 and determined the Doppler width to be $\sim 7.6 \text{ kHz}$ or 0.1 km s^{-1} . This Doppler width, together with the line-of-sight velocities (and corresponding frequencies) of the particles, allow us to broaden each of the spectral lines in our PPV cube.

By incorporating this line profile function, $\phi(\nu)$, into our synthetic observation of a PPV cube, we are able to successfully model the NH_3 (1,1) molecular line emission. For our PPV cube, all of the emission along the LOS is traced to provide an upper limit on the properties of identified dense objects in the cloud. A less-idealized case can be produced where only the gas emission traced by the NH_3 (1,1) line transition is included ($1.8 \times 10^3 < \rho < 10^6 \text{ cm}^{-3}$). Figure 3.6 demonstrates the significant difference between the two cases, where

Figure 3.6(a) shows all the gas emission and Figure 3.6(b) only traces the NH_3 (1,1) line emission.

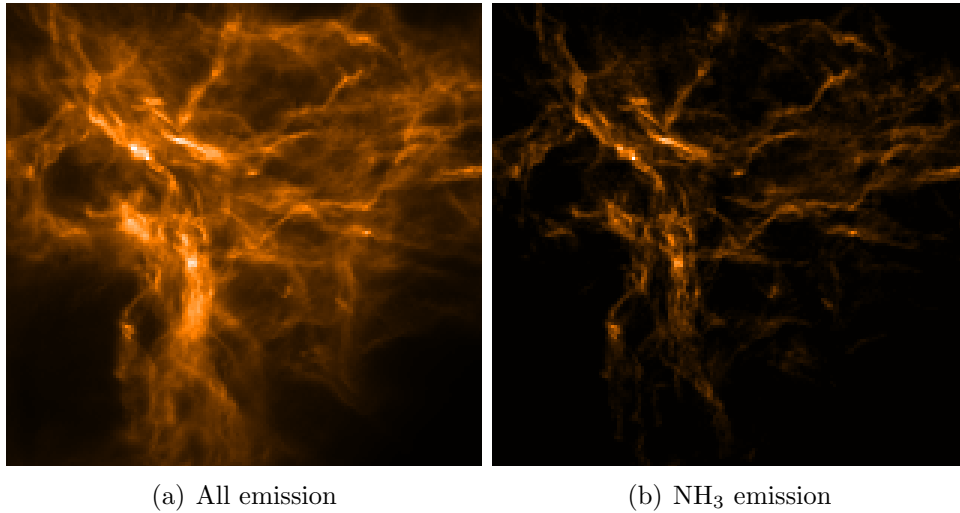


Figure 3.6: Column density maps produced from collapsed PPV data cubes. Figure 3.6(a) includes all of the emission along the line of sight and Figure 3.6(b) includes only the densest gas traced by the NH_3 (1,1) molecular line transition.

We are interested in whether the use of a particular tracer responds better in the identification of dense objects that are correlated in the two-dimensional PP and three-dimensional PPP cases. By testing the NH_3 (1,1) transition as a molecular line tracer, we can determine whether the identified clump properties have any dependence on the limited density range of the traced gas.

3.4 Observer's Tools

There are many tools and techniques which can be used to extract information from an observation. These tools are dependent on the type of instrument,

the wavelength of the observation, and the information required from the observation. In this section, we will discuss the source extraction method and the suite of software packages that we used to analyse our simulated observations. By using the same tools and methods observers use, we are able to provide a direct link between our simulations and actual observations.

3.4.1 Clumpfind

Clumpfind is a method introduced by Williams et al. (1994) which allows for the automated detection of star-forming “clumps” in molecular clouds. Clumps appear as overdensities in the molecular cloud and, by detecting these clumps, we are determining the location of candidates for star formation in their earliest stages. This algorithm was originally developed for the analysis of radio observations of ‘three-dimensional’ spectral-line data cubes. The data cube of intensity in position and velocity is read into a three-dimensional array by Clumpfind. The clumps are identified by searching for local peaks in emission and contouring down to lower intensity levels, marking as clumps all connected areas of pixels above the contour. Clumpfind then decomposes the image into clumps of arbitrarily complex shapes. The output is a companion cube of the clump assignments, which is identical to the original data cube, except instead of intensity values at each pixel there are clump assignment numbers.

There are two key user-defined Clumpfind parameters: the lowest brightness contour level and the contour interval. Clumpfind locates the position of the peak intensity value in the data cube and contours in specified inter-

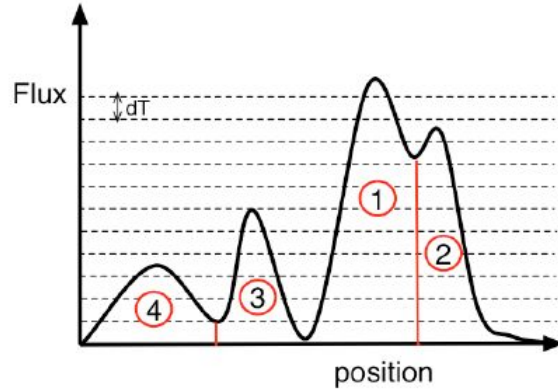


Figure 3.7: A sample of spectral-line data from Smith (2009) displaying how Clumpfind identifies clumps from 3d data.

vals down to the specified minimum contour level (see Figure 3.7). As the algorithm works its way down through the contour levels by set increments, Clumpfind evaluates all connected areas of pixels that have intensity values above each contour level and determines whether these pixels belong to the same clump. If no pixel within a set of adjacent pixels has previously been assigned to a clump (which was initially identified at a higher contour level), then that set is isolated and assigned to be a new clump. If there are pixels within a set which have already been assigned to a clump, then all of the pixels in that set will also be assigned to that clump. For the case where a set includes pixels which have already been assigned to two or more clumps, Clumpfind divides the set by assigning each of the unassigned pixels in that set to whichever previously-identified clump they are nearest. Williams et al. (1994) refer to this as a “friends-of-friends” method.

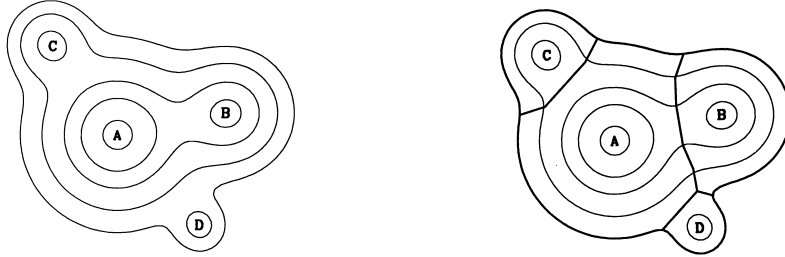


Figure 3.8: A sample contour map from Williams et al. (1994) displaying how Clumpfind identifies clumps. Clump A is identified at the highest contour level and clumps B, C, and D are identified at lower contour levels.

The choice of values for the Clumpfind parameters can have a great impact on the number of clumps identified, as well as the veracity of the clumps. A contour interval that is too small can result in background noise being interpreted as real peaks, where a contour level that is too large can result in real peaks becoming merged together with neighbouring peaks. The lowest contour level is generally set to twice the background noise, σ , for 3d data cubes (Williams et al., 1994); however, there may be cases where the emission should not be followed to the lowest contour level. The optimal size for the increment is also 2σ (Williams et al., 1994). An additional parameter sets the minimum number of pixels per clump. Submillimetre and radio observations use a beam with a fixed size. The beam is the minimum angular resolution of the antenna used in observations and the beam profile can be represented as a Gaussian. The minimum number of pixels should be set to one-third to one-half the number of pixels in this beam, which has an area equal to $1.133 \text{ FWHM} \times \text{FWHM}$, where FWHM is the full-width half-maximum of the beam profile. This prevents clumps smaller than the beam from being identified.

Clumpfind2d² has also been made available by popular request and has been coded in the IDL (Interactive Data Language) programming language for use with two-dimensional continuum data. Clumpfind2d also uses a “friends-of-friends” method to search for local peaks in density and decompose them into individual “clumps” as shown in Figure 3.8. Clumpfind2d differs from Clumpfind by requiring that the structures be identified by eye using user-specified contour levels to divide up the intensity. However, it is often the case that observers will identify the clumps and cores in continuum data using automated algorithms, similar to Clumpfind, such as those built into the Starlink data analysis package, CUPID.

3.4.2 Starlink

Starlink³ is a software environment maintained by the Joint Astronomy Centre and contains very useful software packages often used by many observers to reduce and analyse their data. All subsequent data analysis in this thesis is done using packages from the Starlink collection. All clumps were identified using the *findclumps* task from the source extraction software package, CUPID, which is a part of the Starlink software collection.

The *findclumps* task is designed to run the 2006 modified version of the Clumpfind algorithm, which accepts clumps that do not extend above the second contour level, resulting in the identification of many more low mass objects. This is the version of Clumpfind that is currently used in IDL. We

² Made available to the community at <http://www.ifa.hawaii.edu/users/jpw/clumpfind.shtml>

³ Made available to the community at <http://starlink.jach.hawaii.edu>

have chosen to use CUPID Clumpfind as opposed to IDL Clumpfind, as CUPID provides the option to use the original algorithm as it was described in the published paper by Williams et al. (1994). The original 1994 version of Clumpfind differs in several ways from the IDL implementation. The original version ensures that all peaks must extend beyond the second contour interval and rejects any clumps that do not, where the IDL version omits this restriction. The IDL version also allocates pixels within merged clumps differently than described in Williams et al. (1994). By choosing to use original 1994 version of Clumpfind, we can be certain that we fully understand the method by which Clumpfind identifies and assigns its clumps as it is well-documented in the published paper (Williams et al., 1994). The *findclumps* task also has the capability to run various other clump-finding algorithms, such as Gauss-clumps (Stutzki & Güsten, 1990), in addition to the two versions of Clumpfind. Clumpfind is one of the most widely-used clump-finding algorithms, so we have chosen to focus solely on this algorithm in this thesis.

The *findclumps* task can identify clumps of emission within both a 2d continuum map and 3d spectral-line data cube, as well as within a full three-dimensional data cube produced from the simulation. The default Clumpfind setting in *findclumps* for both the contour interval and lowest contour level parameters is 2σ , twice the background noise, as discussed previously in Section 3.3.1. These criteria will still often find objects that are not believable and would require manual rejection, particularly for cases with a broad dynamic range such as continuum data. A stricter criteria of 5σ for the lowest contour level and 3σ for the contour increment can be used for the 2d case to produce results which are more reliable.

There are many useful packages in the Starlink software environment, including those which allow for direct manipulation of the 2d maps and 3d data cubes. Tasks such as *gausmooth* and *skynoise* allow for the effect of smoothing and noise to be introduced to a simulated observation by convolving the image with a circular Gaussian beam and adding artificial background noise. Although these options are available, we have chosen to study the raw synthetic observations in order to reach the highest achievable resolution.

Starlink also has a built-in image and data cube display and analysis tool, GAIA (Graphical Astronomy and Image Analysis). GAIA can display individual slices of a data cube as well as show the spectra for each line of sight. We are able to display our synthetic observations using GAIA and visualise and analyse them in ways that actual observations are studied.

3.5 Summary

In this chapter, we have described in detail the simulation completed by Petitclerc (2009), our methods to produce synthetic observations from the simulation, and the tools which we used to study and analyse our observations. The synthetic observations provide us with the means to study the effects and biases which may result from the use of common observer's tools, such as Clumpfind. This study is particularly significant with current observations by Herschel and upcoming observations using SCUBA-2 and ALMA set to reach greater resolutions and higher sensitivities than have previously been attainable.

Bibliography

- André, P. & Saraceno, P. 2005. in *The Dusty and Molecular Universe: A Prelude to Herschel and ALMA*, ESA SP-577, 179
- Ballesteros-Paredes, J., Klessen, R. S., Mac Low, M.-M., Vázquez-Semadeni, E. 2007. Molecular Cloud Turbulence and Star Formation. In *Protostars and Planets V*, eds. B. Reipurth, D. Jewitt, and K. Keil (Tucson: University of Arizona Press), pp.63-80
- Bate, M. R. 2009, MNRAS, 392, 590
- Bate, M. R. & Bonnell, I. A. 2005, MNRAS, 356, 1201
- Bate, M. R., Bonnell, I. A., & Bromm, V. 2003, MNRAS, 339, 577
- Bergin, E. A. & Tafalla, M. 2007, ARA&A, 45, 339
- Caselli, P., Walmsley, C. M., Zucconi, A., Tafalla, M., Dore, L., & Myers, P. C. 2002a, ApJ, 565, 331
- Fukui, Y. 2005. in *The Dusty and Molecular Universe: A Prelude to Herschel and ALMA*, ESA SP-577, 81
- Genzel & Stutzki 1989, ARA&A, 27, 41
- Holland, W. S., Duncan, W., Kelly, B. D., Irwin, K. D., Walton, A. J., Ade, P. A. R., & Robson, E. I. 2003, SPIE, 4855, 1

Holland, W., MacIntosh, M., Fairley, A., Kelly, D., Montgomery, D., Gostick, D., Atad-Ettedgui, E., Ellis, M., Robson, I., Hollister, M., Woodcraft, A., Ade, P., Walker, I., Irwin, K., Hilton, G., Duncan, W., Reintsema, C., Walton, A., Parkes, W., Dunare, C., Fich, M., Kycia, J., Halpern, M., Scott, D., Gibb, A., Molnar, J., Chapin, E., Bintley, D., Craig, S., Chylek, T., Jenness, T., Economou, F., & Davis, G. 2006, SPIE, 6275, 45

Jørgensen, J. K., Johnstone, D., Kirk, H., & Myers, P. C. 2007, ApJ, 656, 293

Klessen, R. S. 2001, ApJ, 556, 837

Lada, C. J., Lombardi, M., & Alves, J. F. 2009, ApJ, 703, 52

Larson, R. B. 2003, Rep. Prog. Phys., 66, 1651

MacKenzie, T., Braglia, F. G., Gibb, A. G., Scott, D., Jenness, T., Serjeant, S., Thompson, M., Berry, D., Brunt, C. M., Chapin, E., Chrysostomou, A., Clements, D., Coppin, K., Economou, F., Evans, A., Friberg, P., Greaves, J., Hill, T., Holland, W., Ivison, R. J., Knapen, J. H., Jackson, N., Joncas, G., Morgan, L., Mortier, A., Pearson, C., Pestalozzi, M., Pope, A., Richer, J., Urquhart, J. S., Vaccari, M., Weferling, B., White, G. & Zhu, M. 2011, MNRAS, 415, 1950

Men'shchikov, A., André, P., Didelon, P., Könyves, V., Schneider, N., Motte, F., Bontemps, S., Arzoumanian, D., Attard, M., Abergel, A., Baluteau, J.-P., Bernard, J.-P., Cambrésy, L., Cox, P., di Francesco, J., di Giorgio, A. M., Griffin, M., Hargrave, P., Huang, M., Kirk, J., Li, J. Z., Martin, P., Minier, V., Miville-Deschênes, M.-A., Molinari, S., Olofsson, G., Pezzuto, S., Roussel, H., Russeil, D., Saraceno, P., Sauvage, M., Sibthorpe, B., Spinoglio,

- L., Testi, L., Ward-Thompson, D., White, G., Wilson, C. D., Woodcraft, A., & Zavagno, A. 2010, *A&A*, 518, 103
- Olmi, L., Testi, L., & Sargent, A. I. 2005, *A&A*, 431, 253
- Pineda, J. E., Goodman, A. A., Arce, H. G., Caselli, P., Foster, J. B., & Rosolowsky, E. W. 2010, *ApJ*, 712, L116
- Petitclerc, N. 2009, PhD Thesis, McMaster University
- Price, D. J. 2007, *PASA*, 24, 159
- Reid, M. A., Wadsley, J., Petitclerc, N., & Sills, A. 2010, *ApJ*, 719, 561
- Schmalzl, M., Kainulainen, J., Quanz, S. P., Alves, J., Goodman, A. A., Henning, T., Launhardt, R., Pineda, J. E., Román-Zúñiga, C. G. 2010, *ApJ*, 725, 1327
- Smith, R. J., Clark, P. C., & Bonnell, I. A. 2008, *MNRAS*, 391, 1091
- Smith, R. J. 2009, PhD Thesis, University of St. Andrews
- Stutzki, J. & Güsten, R. 1990, *ApJ*, 356, 513
- Tilley, D. A., & Pudritz, R. E. 2004, *MNRAS*, 353, 769
- van Dishoeck, E. F. & Jørgensen, J. K. 2008. in *Science with the Atacama Large Millimeter Array*, pp.15-22
- Wadsley, J., Reid, M., Qamar, F., Sills, A., & Petitclerc, N. 2011, *IAU Symposium 270*, 129
- Wadsley, J. W., Stadel, J., & Quinn, T. 2004, *New Astronomy*, 9, 137

M.Sc. Thesis — Rachel Louise Ward — McMaster University - Physics and Astronomy — 2011

Williams, J. P., de Geus, E. J., & Blitz, L. 1994, ApJ, 428, 693

Chapter 4

Analysis & Results

4.1 Introduction

In this chapter, we will describe the analysis performed on the synthetic observations we have created, which were described in Chapter 3. We used the popular clump-finding algorithm, Clumpfind (Williams et al., 1994), which has been discussed previously in Chapter 3, to identify dense regions in our simulated cloud. In doing so, we are able to isolate areas which are candidates for star-forming regions. We will henceforth refer to these candidates as “clumps”. This definition differs slightly from the observer definition of a clump presented in Chapter 2. Here, we are defining a clump as anything that Clumpfind identifies, regardless of its size and density. Once we identified these clumps, we studied their global and individual properties, including mass distribution, size, velocity dispersion, and boundedness. To test the boundedness, we returned to the true nature of the clumps in the simulation – the particles from which they are composed. Using the energies of these particles, we are able to divide these clump candidates into one of two classes: a starless

core or a prestellar core (See Chapter 2). A comparison of these properties follows, leading to a discussion of the most likely traceable properties of bound cores.

4.2 Clump-Finding and Correlations

With our simulation of molecular cloud collapse for the spherical collapse case, we have “observed” the clumps formed within the cloud using the clump-finding algorithm, Clumpfind (Williams et al., 1994). Although it has been argued that certain algorithms can be useful tools for cloud comparisons even if one does not believe the clumps within the clouds are physically real (Scalo, 1990), one of the main goals of this research was to determine how often a clump observed in PP and PPV corresponded to something that is physically real in the simulation. We define an object as a physically real star-forming core if it is resolved to more than 750 particles (minimum mass of $0.1 M_{\odot}$ (Simpson, Nutter, & Ward-Thompson, 2008)), has a radius less than 0.1 pc and mean densities exceeding 10^4 cm^{-3} (Bergin & Tafalla, 2007; Myers, 1999), and is gravitationally bound.

4.2.1 Studying Clumps in the Third Dimension

In order to compare real objects found in our simulations to objects seen in our simulated observations, we need to characterize the simulation in a way that is complementary to the observations. Therefore, we interpolated the SPH particles to a full position-position-position (PPP) grid and created a 3D cube

which provides the desired third physical dimension. As discussed previously in Chapter 2, each particle has a smoothing kernel. We have divided up the particle mass into grid ‘cubes’ by their specific weights. Instead of normalizing the 2D kernel weights over the grid, the weights were used to divide up the position of the particles along the line of sight (z -direction). The resolution is the same in every direction, allowing the cube to be rotated and “observed” along any line of sight. For this thesis, the line of sight axis is always chosen to be the z -axis, the time is 1.30 Myr from initial collapse, and the collapse case is spherical collapse (Run D from Table 4.1) unless otherwise stated. By creating a PPP cube in the FITS format, we were able to still use Clumpfind and other Starlink tools, as well as use GAIA to study the cube as a 3D volume rendering. This allowed us to determine where long filaments along the line of sight may occur.

The PPP cube was normalized to contain a total mass of $5000 M_{\odot}$ to ensure that the total mass of each particle is counted only once. Collapsing the cube along the z -axis line of sight using the *collapse* task from the KAPPA software package, a part of the Starlink software environment, produces a column density map similar to that created in Chapter 3. The difference between this collapsed cube and the column density map described in Chapter 3 arises from the methods by which they were made. The PP column density map was created using the 2D kernel as an approximation, where the collapsed cube was derived from direct interpolation of the particles to a grid. This difference is minimal, as the residual has a pixel median of $10^{-7} M_{\odot}/\text{pixel}$, compared to a typical pixel median of $10^{-4} M_{\odot}/\text{pixel}$ for our synthetic maps. Since the result of the residual is negligible, we treat the two maps as though they are the

same; however, in most cases, we note that we have used the collapsed cube for the analysis. The maximum pixel value in the PP column density map was $\sim 1.2 M_{\odot}/\text{pixel}$ for a coarse resolution of $6000 \text{ AU}/\text{pixel}$ at a time 1.30 Myr after initial cloud collapse. By comparison, the maximum pixel value in the PPP data cube was $\sim 0.8 M_{\odot}/\text{pixel}$ using the same resolution. As a preliminary test, this shows that it is quite possible that the PP column density map may be overestimating the mass by $\sim 50\%$. To obtain an estimate of the rms noise for both the PPP cube and the collapsed PP column density map, we divided the maximum pixel values by a typical dynamic range. The dynamic range is defined as the ratio between the brightest intensity and the background noise. In observations, the dynamic range specifies the range of intensity values an instrument can achieve based on its spectral resolution and flux sensitivity. As an example, the dynamic range on the Herschel instruments, PACS and SPIRE, are 1000 and 200, respectively (Motte et al., 2010). A conservative estimate of 200 was used as the dynamic range for the PPP cube, resulting in an rms noise value of approximately $0.005 M_{\odot}/\text{pixel}$ for a resolution of $6000 \text{ AU}/\text{pixel}$. Setting the lowest density contour level in Clumpfind to 3σ and the contour increment to 2σ results in the identification of 499 clumps which contain $\sim 430 M_{\odot}$ of material or $\sim 9\%$ of the total mass in the simulation. All identified clumps were included in our sample, as there was no manual rejection of any of the clumps.

Using the PPP cube, we can explore the role of orientation and test its effect on clump identification. We ran the Clumpfind algorithm and, by rotating the PPP cube and using a fixed set of parameters, we were able to compare our results as a test to confirm that all of our results are consistent and trustworthy.

Table 4.1: Total mass contained in clumps

Run	Description	# of clumps	Mass in clumps	% of M_{total}
A	1.25 Myr	435	334 M_{\odot}	7%
B	1.30 Myr (x)	499	430 M_{\odot}	9%
C	1.30 Myr (y)	498	430 M_{\odot}	9%
D	1.30 Myr (z)	499	430 M_{\odot}	9%
E	1.35 Myr	543	546 M_{\odot}	11%
F	1.30 Myr (Ribbon)	900	860 M_{\odot}	17%
G	1.30 Myr (Sheet)	742	736 M_{\odot}	15%
H	1.30 Myr (Filament)	935	1076 M_{\odot}	22%

We rotated the PPP cube to reorient the line of sight axis first along the x-direction and then along the y-direction and ran Clumpfind on these rotated cubes. We compared these with the previous Clumpfind results for the line of sight along the z-direction (Table 4.1). We found the total mass in clumps differed by $\pm 0.02 M_{\odot}$, the maximum pixel was consistently located at the pixel coordinate (198, 260, 265), and the number of clumps identified varied by only ± 1 clump. This test provides a reasonable estimate of the uncertainty in the simulation and in the number of clumps identified in the PPP cube.

Table 4.1 also shows the evolution of the clumps and the dependence of dense core formation on the initial collapse condition of the cloud. We have provided run identifiers to simplify references to each case. At an earlier time (1.25 Myr after initial collapse), there were fewer identified dense objects than seen at later times. Since the number of dense objects identified by Clumpfind increased as time evolved and the mass of the cloud contained in clumps also increased, this suggests that the densest objects are growing in size and mass and that more dense regions are forming in the cloud as it continues to collapse.

This is especially evident when we study the effect of the initial turbulent velocity spectrum on the formation of dense cores. Using identical parameters as used for the spherical collapse case, the ribbon, sheet, and filament collapse cases all found significantly more dense clumps and more mass contained in clumps than that seen for the spherical case. This result implies that dense cores in the cloud are more inclined to form in filamentary-like structure, which is in agreement with conclusions drawn from recent observations of star-forming regions (Arzoumanian et al., 2011; Schmalzl et al., 2010; Men’shchikov et al., 2010).

The mass distribution of the identified objects for Run D are plotted in Figure 4.1. This clump mass function (CMF) closely reflects the power-law trend at high mass seen in the stellar IMF (Salpeter, 1955). The line of best fit at the high-mass end has a slope of -2.27 ± 0.07 for masses greater than $0.5M_{\odot}$, compared to the power-law Salpeter (1955) slope of -2.35 . This is also in good agreement with the Kroupa (2001) IMF, where

$$dN \propto m^{-2.3} dm \quad m \geq 0.5M_{\odot}$$

and also with the results by Motte et al. (1998) who extracted a clump mass function from dust continuum observations of the ρ Ophiuchi main cloud to show that the slope of the power law at the high-mass end can range depending on the cut-off mass

$$\begin{aligned} dN/dm &\sim m^{-1.5} & 0.1M_{\odot} < m \leq 0.5M_{\odot} \\ dN/dm &\sim m^{-2.5} & 0.5M_{\odot} < m \leq 3M_{\odot} \end{aligned}$$

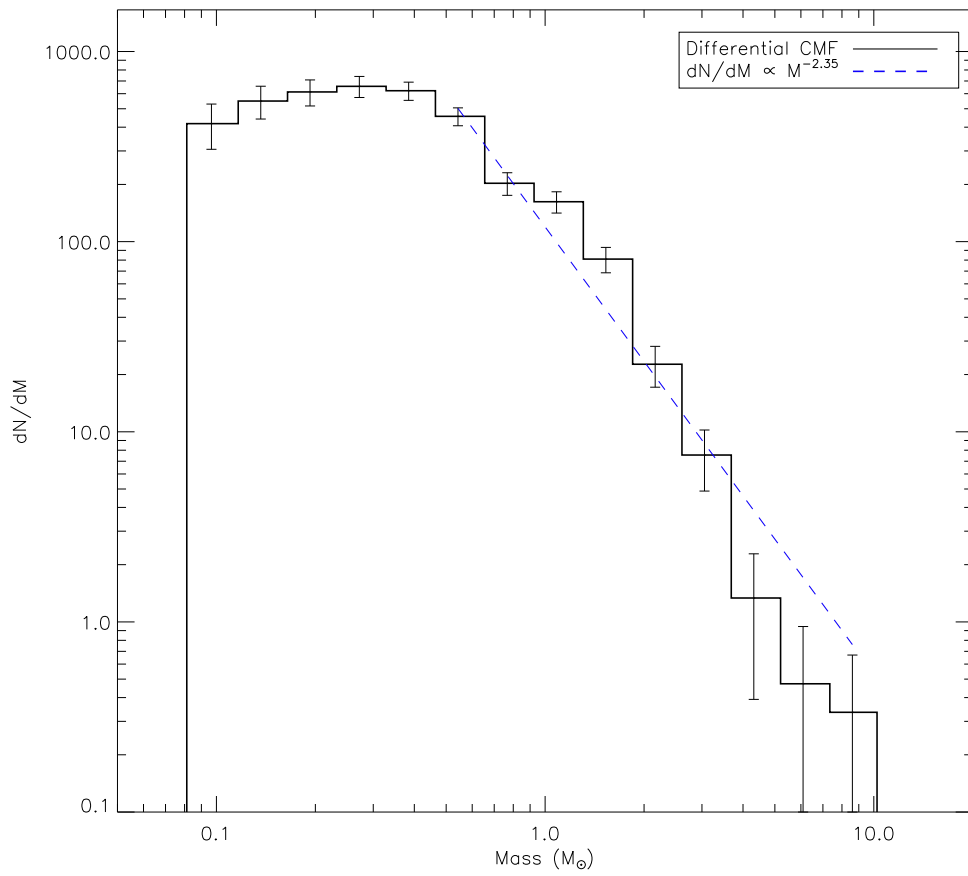


Figure 4.1: Clump mass function (CMF) derived from the PPP cube with a resolution of 6000 AU/pixel. The error bars correspond to \sqrt{N} counting statistics. The blue dotted line is the Salpeter (1955) IMF.

Our simulations look and behave like real molecular clouds. Our clouds are visually similar to observations, exhibit the same characteristic mass distribution, and show the presence of turbulent substructure. Based on all of these results, we can compare our simulation to observations with confidence.

4.2.2 Clump Correlations, Round One: PP vs. PPP

Our aim is to directly compare clumps identified in a PPP cube with those identified in a projected PP synthetic observation. We start by running an automated version of Clumpfind2d on the synthetic column density map, as this is the method predominantly used by observers to identify dense structures in continuum data. When Clumpfind2d was initially developed, it relied on the dense structures being identified by eye using user-specified contour levels. This can prove to be very tedious work, especially for very large data sets, and many observers have relied on automated algorithms, including automated versions of Clumpfind2d, to identify structures in dust continuum maps. Using the PP column density map with a resolution of 6000 AU/pixel, we ran Clumpfind2d for a variety of different parameters to demonstrate the strong dependence of the choice of parameters on the number of clumps identified. Our results are shown in Table 4.2, where ‘Low’ is the lowest brightness contour level and ‘Step’ is the contour interval. Although a change of parameter can cause the number of identified clumps to vary greatly, the amount of mass in clumps is independent of the parameters chosen. The mass in clumps is staggeringly large and makes up $> 90\%$ of the mass of the entire cloud. Clumpfind2d decomposes the cloud into clumps similar to how a picture can

Table 4.2: Table of Clumpfind2d Parameter Sensitivity

RMS (σ)	Low	Step	# of clumps	Mass in clumps	% of M_{total}
0.005 M_{\odot}/px	3σ	2σ	886	4936.7 M_{\odot}	99%
0.006 M_{\odot}/px	3σ	2σ	558	4776.9 M_{\odot}	96%
0.007 M_{\odot}/px	3σ	2σ	532	4723.1 M_{\odot}	94%
0.006 M_{\odot}/px	5σ	3σ	455	4558.3 M_{\odot}	91%
0.005 M_{\odot}/px	5σ	3σ	503	4648.1 M_{\odot}	93%

be carved into pieces of a puzzle. For this reason, many of these clumps may not necessarily connect to any physical structures within the cloud.

Since Clumpfind2d locates clumps by identifying local peaks in density in PP dust continuum maps, observers have no precise method to distinguish which material along the line of sight should belong to a clump and, therefore, all dust emission along the line of sight is included. The inclusion of all emission, even low-density gas unassociated with the dense region, affects the determination of clump properties. One advantage of our simulation is that we can rotate the cloud and look at the column of gas from another perspective (Figure 4.2). This allows us to see that there is a great deal of low-density emission that is very filamentary in its nature along the line of sight. When the simulation is integrated along this axis to produce a two-dimensional column density map, all of this emission is summed up resulting in an identified object with a mass which is larger than the real star-forming clump.

We have shown for the case of dust continuum observations, clump identification can be entirely arbitrary. Not only is all the emission along the line of sight included in the mass estimate (see Figure 4.2), but the choice of user-defined parameters has an extreme effect on the outcome. It has previ-

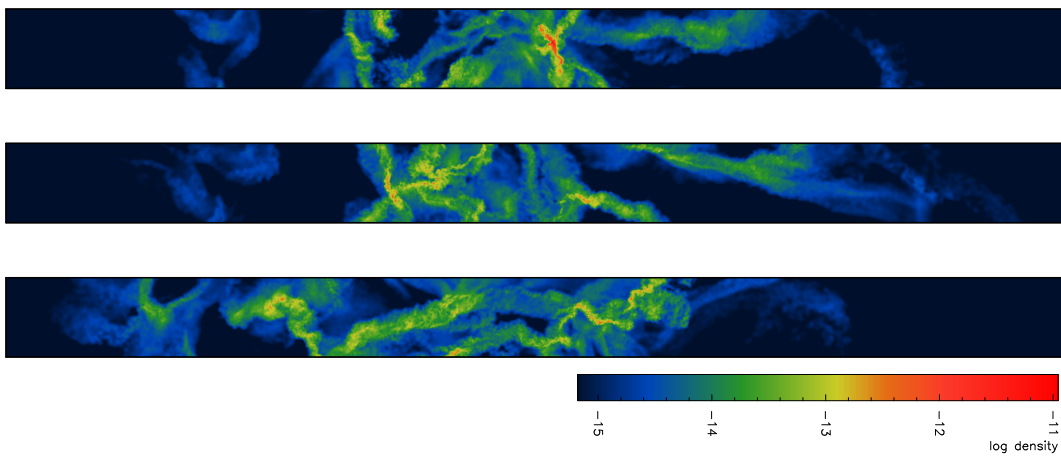


Figure 4.2: Cross-section slices of the simulation in the xz -plane. Large filaments of low density gas are present along the z -axis, chosen to be our line of sight, when observed in the xz -plane. These three cases show what could possibly be perceived as one clump in the xy -plane are more likely one clump (top), two clumps (middle), or no defined clumps (bottom) contaminated by excess low-density material along the line of sight. These slices have a width of 1.5×10^5 AU and a length of 2×10^6 AU, extending fully across the simulation.

ously been shown that clump properties determined from Clumpfind2d can be unreliable (Kainulainen et al., 2009). Our results confirm that the slightest change of a parameter in a clump-finding algorithm can drastically alter both the number of clumps located and the properties of those clumps. It would be difficult to obtain sets of parameters for Clumpfind for both PP and PPP that were comparable to one another and which would produce the same statistical result. Rather than identify clumps independently in both PP and PPP using Clumpfind, we have taken the clumps that we trust the most (i.e. those located in a true three-dimensional volume) and measure the global properties of the *projection* of those clumps. Our method of achieving this is by using a mask to track the exact clumps from the PPP cube and trace them directly onto the PP map. This ensures that the clumps identified in PPP are compared to the exact same clumps in PP.

4.2.2.1 Global Properties

For the case studied in Section 4.2.1, Clumpfind identified 499 clumps in the PPP cube and returned the integrated intensity and the peak (x,y,z) positions of each of these clumps. Due to our choice of units for the synthetic observations, the integrated intensity provided for each clump is already a mass estimate for that clump in units of solar masses. In order to obtain a mask to mark the positions of the desired clumps, we removed all “background” emission from the PPP cube which had not been assigned to a clump. Clumpfind assigns an identification number to each clump, often listing the clump with the greatest density peak as Clump 1. The clump assignment file

produced as output is also a 3D data cube, identical to the original except there are clump assignment numbers in place of intensities. This clump assignment file was used as a pixel mask to select only the emission in clumps and to set every other unassigned pixel value equal to ‘Null’. We were able to collapse this masked cube along the line of sight to produce the map shown in Figure 4.3(b), which includes only the emission from the clumps identified in PPP. From this map, we now have the (x,y) coordinates of every pixel that belongs to a clump. We used the (x,y) pixel coordinates of the PPP clumps to create a new 2D mask, which we applied to the original PP column density map. The resultant map left behind only the emission from the 3D PPP clumps *as they would be observed in 2D*. This ‘correlation’ method effectively ensures that the clumps have an equal projected area and pixels with identical (x,y) coordinates.

A key goal in the theory of star formation is to understand the distribution of stellar masses at the time of their birth. In order to reach this goal, many observational and theoretical studies of the early phases of star formation involve the distribution of clump masses or the clump mass function (CMF) (e.g. Motte et al., 1998; Alves et al., 2007). Since CMFs are very often derived from continuum maps (Di Francesco et al., 2007), we have produced a CMF from our column density map, shown in Figure 4.4. Figure 4.4 compares the CMFs of clumps identified in the PP map using the Clumpfind2d method and our correlation method described above. The correlation method finds the *projected* masses of the PPP clumps by including all the emission along the line of sight. The result of this method is a distribution of 499 clump masses. Since the number of clumps identified using the Clumpfind2d method

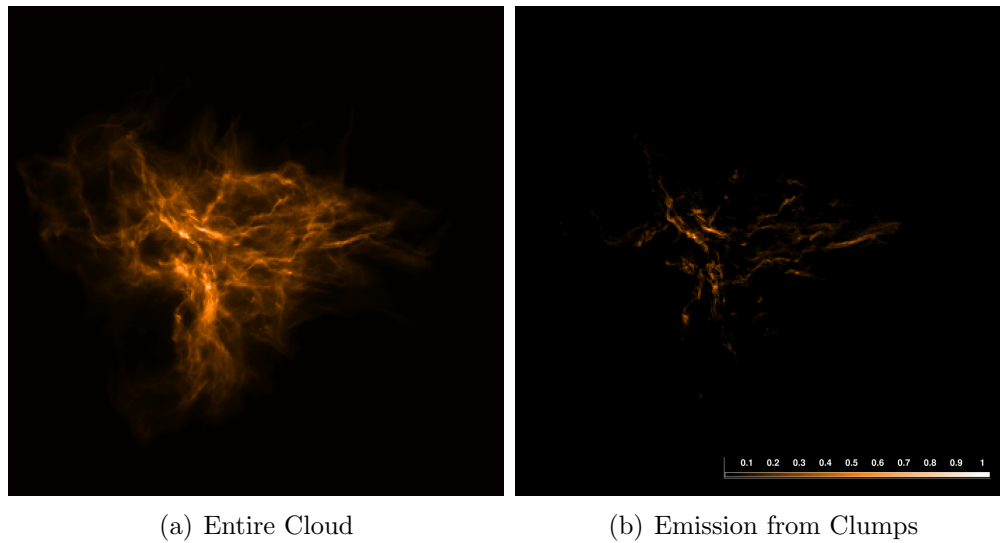


Figure 4.3: Left: PP column density map of spherical molecular cloud collapse for a resolution of 6000 AU/pixel with projection along the z-axis onto a 500 x 500 grid. Right: The remaining emission contained in the clumps identified by CLUMPFIND for the PPP case after the cube has been collapsed.

can vary greatly depending on the parameters chosen, we have attempted to select parameters which result in a similar number of clumps. We have chosen a minimum contour level of 5σ with a contour interval of 3σ , where $\sigma=0.005 M_{\odot}/\text{pixel}$ was the estimated rms noise for a resolution of $6000 \text{ AU}/\text{pixel}$.

Figure 4.4 shows that the two distributions are very similar where the only significant difference is the CMF produced by the Clumpfind2d method is shifted to slightly higher masses compared to the correlation method CMF. This comparison demonstrates that our correlation method is comparable to the Clumpfind2d method and both methods will produce a statistically similar result. Since we can expect the results from the correlation method to be similar to the results obtained from Clumpfind2d, our correlation method is justified and it is ensured that our results have application to observations.

We have seen that the total mass contained in clumps in the PPP cube is $\sim 430 M_{\odot}$. Using the correlation method, the total mass contained in clumps from the masked PP map, which has an equal area in the XY-plane to the clumps in the PPP cube (2.7% of the total area), is $1647 M_{\odot}$. This is not surprising as large amounts of low density material along the line of sight are now contributing to the mass estimate of the clumps in those columns (see Figure 4.2). The interesting part is how significant this contribution is. The mass between the true PPP clumps and the estimates made from a PP “observation” of these very clumps differs by a factor of 3 to 4. Figure 4.5 shows the mass distribution of the 499 clumps for both the PPP case and the PP projection.

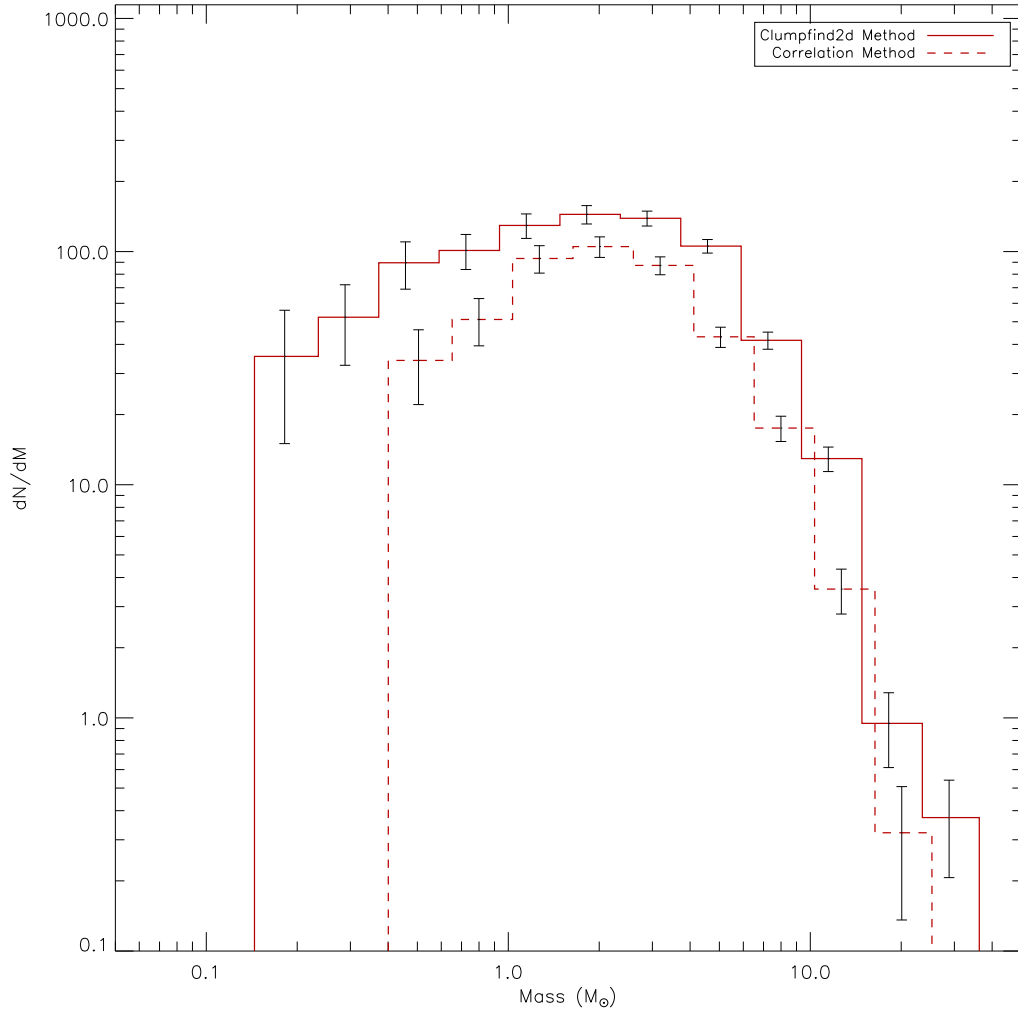


Figure 4.4: Clump mass function of the clumps identified in the PP column density map using Clumpfind2d (red solid line) compared to a clump mass function of clumps identified from the same PP column density map using our ‘Correlation’ method (red dashed line).

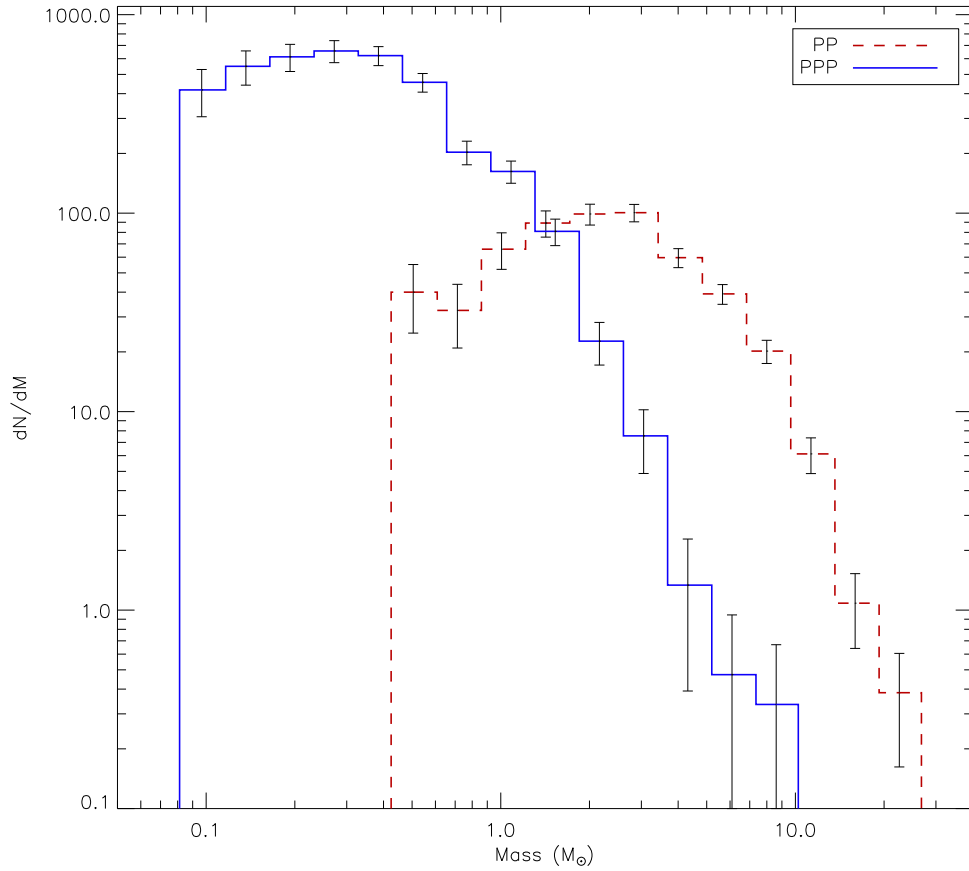


Figure 4.5: Clump mass function of the clumps identified in the PPP data cube (blue solid line). Also shown is the clump mass function of the same clumps with their masses estimated from the 2D (x,y) projected PP image (red dotted line).

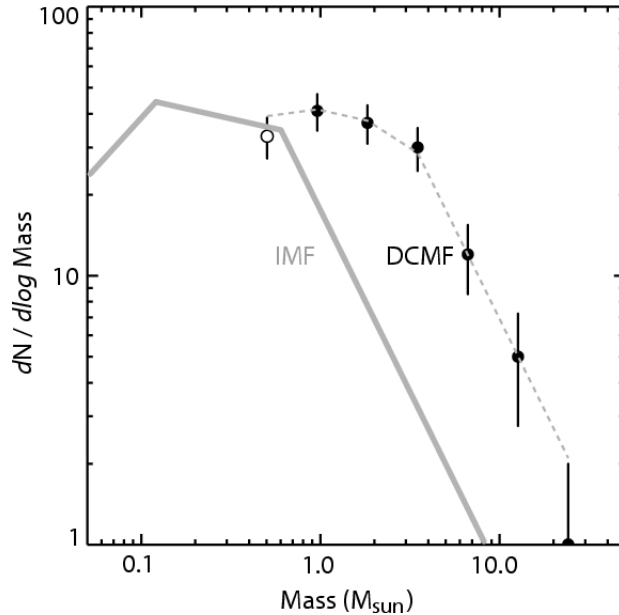


Figure 4.6: This figure from Alves et al. (2007) compares the dense core mass function (DCMF) from observations of star-forming regions in the Pipe Nebula to the stellar IMF of the Trapezium cluster. The authors suggest that the two mass functions differ only by a uniform star formation efficiency factor.

This result is curiously familiar (See Figure 4.6 taken from Alves et al. (2007)). Figure 4.6 compares the Pipe Nebula dense core mass function (DCMF) to the Trapezium cluster stellar IMF (Muench et al., 2002) and finds that the DCMF is shifted from the IMF to higher masses by a factor of 4. A background-subtracted DCMF was constructed and Alves et al. (2007) found from their observations of the Pipe Nebula that their DCMF was remarkably similar in shape to the stellar IMF. However, they concluded that the DCMF was still shifted upwards in mass from the IMF by a factor of 3 once the correction for the extended background emission was included.

Alves et al. (2007) argue that the similarity between the DCMF (Dense Core Mass Function) and the stellar IMF is due to the stellar IMF being a direct result of the distribution of the dense cores and assumes a one-to-one correspondence. This factor of 3 has been used to infer a uniform star formation efficiency of $\sim 30\%$. Rathborne et al. (2009) repeated the analysis of the Pipe Nebula performed by Alves et al. (2007) using more recent observations and confirmed that the shape of the CMF is indeed similar to the stellar IMF, but found a larger scale factor to higher masses of ~ 4.5 . However, Reid et al. (2010) argue that the shape itself is a result of the central limit theorem and that this similarity is not significant. Although there is much debate over whether the CMF and IMF have a direct one-to-one correspondence (Reid et al., 2010; Anathpindika, 2011; Swift & Williams, 2008), no other alternative explanation for the factor of 3 difference has been offered and many authors continue to cite this factor of 3 as a core-to-star conversion factor (e.g. Enoch et al., 2008; Offner et al., 2009). Figure 4.5 shows that this apparent “efficiency” factor of 30% is solely due to an effect of projection. According to our simulation, low density gas and multiple cores along a single line of sight will contribute to a mass which will be consistently overestimated by a factor of 3 to 6, depending on the method of binning and the initial collapse condition. A similar multiplicative factor was also seen in independent analysis of our data by Petitclerc (2009), where the median mass of their clump mass distribution was approximately a factor of 4 larger than the median mass of the Chabrier (2005) IMF for multiple systems.

4.2.2.2 Clump-by-Clump Comparison

Using the masses obtained for each of the 499 clumps from the correlation method described above, we have plotted the “observed” masses of each clump (in PP) against their corresponding “actual” masses (in PPP). Rather than plotting the mass function to compare the distributions, we performed a direct clump-to-clump comparison of the masses. The “actual” mass is defined as the mass of a clump measured from the full 3d PPP simulation. This is based only on the results of Clumpfind, as we are not yet considering boundedness as an issue. The “observed” mass is defined to be the mass of the same clump as it would be measured from the projected PP column density map. Figure 4.7 shows the relationship between the masses. We note that as the objects become more massive in physical space, they are also measured to be more massive in projected space. However, these observed masses are, on average, ~ 6 times larger than the actual masses. If the masses measured from a column density map were true representations of the mass of the object, we would expect all of the data points in Figure 4.7 to fall on or near the one-to-one line, shown as a dashed black line in Figure 4.7.

The data definitely does not lie on or near the one-to-one line. There are a limited number of data points at the high mass end due to fewer high mass objects being formed. One noticeable effect is that it appears that regardless of the true mass of the object, additional mass along the line of sight can contribute enormously to the estimated mass of the object.

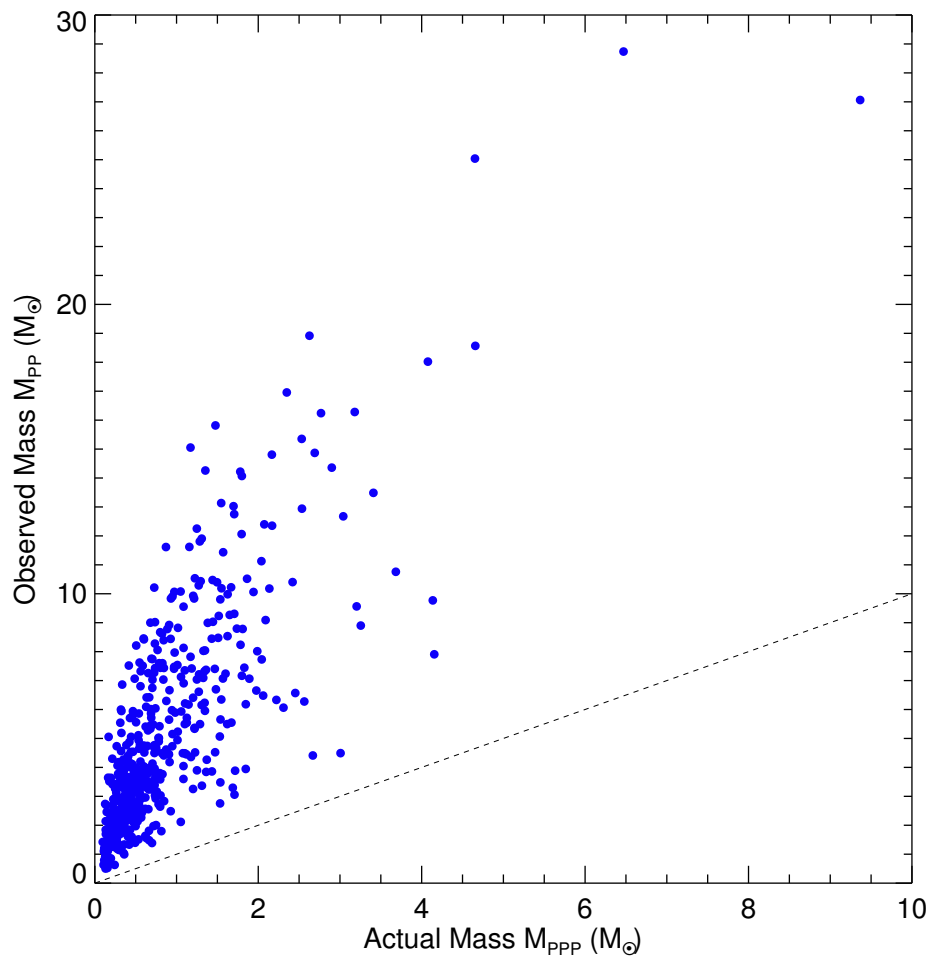


Figure 4.7: Plot of the “observed” mass (PP) vs. the “actual” mass (PPP). The dashed black line is the 1-to-1 line.

If we plot the data on a log-log plot, a power-law trend emerges (Figure 4.8). The function which best fits the data, $\log M_{\text{PP}} = m \log M_{\text{PPP}} + b$, can also be written as

$$M_{\text{PP}} = c (M_{\text{PPP}})^m$$

where $c = 10^b$ is a constant in units of solar masses. A function of

$$M_{\text{PP}} = 6 (M_{\text{PPP}})^{0.7}$$

was fit to the data with a reduced chi-squared of 3.5×10^{-2} . For a given PPP mass between $2M_{\odot}$ and $10M_{\odot}$, this function can provide a range of possible PP masses that are ~ 3 -5 times greater, which is again comparable to the factor of three often quoted in other works with regard to the CMF (Alves et al., 2007; Enoch et al., 2008; Offner et al., 2009). The estimated PP masses can be even more than 3-5 times greater than the ‘actual’ mass for objects with lower PPP masses.

Figure 4.9 shows that this relation between the “observed” masses and “actual” masses is present at different evolutionary stages, for different orientations, and for different initial collapse conditions. Table 4.3 summarizes the best fit parameters for each case. The best fit parameters and uncertainties are calculated using a non-linear least-squares curve-fitting algorithm, CURVEFIT, from IDL. The errors listed in Table 4.3 are the standard deviations of the best fit parameters.

When we compared the best fit parameters, we noticed that slope of the log-log plot for each case listed in Table 4.3 is approximately equal to $2/3$. Our interpretation is that this power-law trend is related to the surface area and volume of the clump.

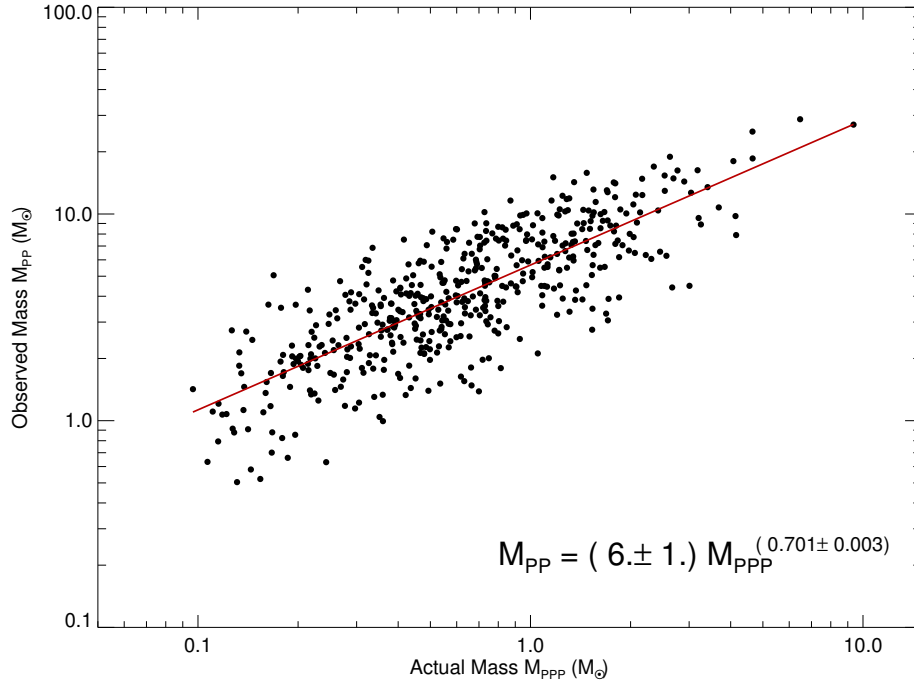


Figure 4.8: Log-log plot of the “observed” mass (PP) vs. the “actual” mass (PPP). A fit to the data is shown as a solid red line.

Table 4.3: Table of Best Fit Parameters to $M_{PP} = c (M_{PPP})^m$

	c	m
1.25 Myr	6 ± 1	0.7 ± 0.1
1.30 Myr (x)	8 ± 1	0.7 ± 0.1
1.30 Myr (y)	6 ± 1	0.7 ± 0.1
1.30 Myr (z)	6 ± 1	0.701 ± 0.003
1.35 Myr	6 ± 1	0.69 ± 0.05
1.30 Myr (Ribbon)	8 ± 1	0.79 ± 0.09
1.30 Myr (Sheet)	7 ± 1	0.7 ± 0.1
1.30 Myr (Filament)	7 ± 1	0.71 ± 0.06

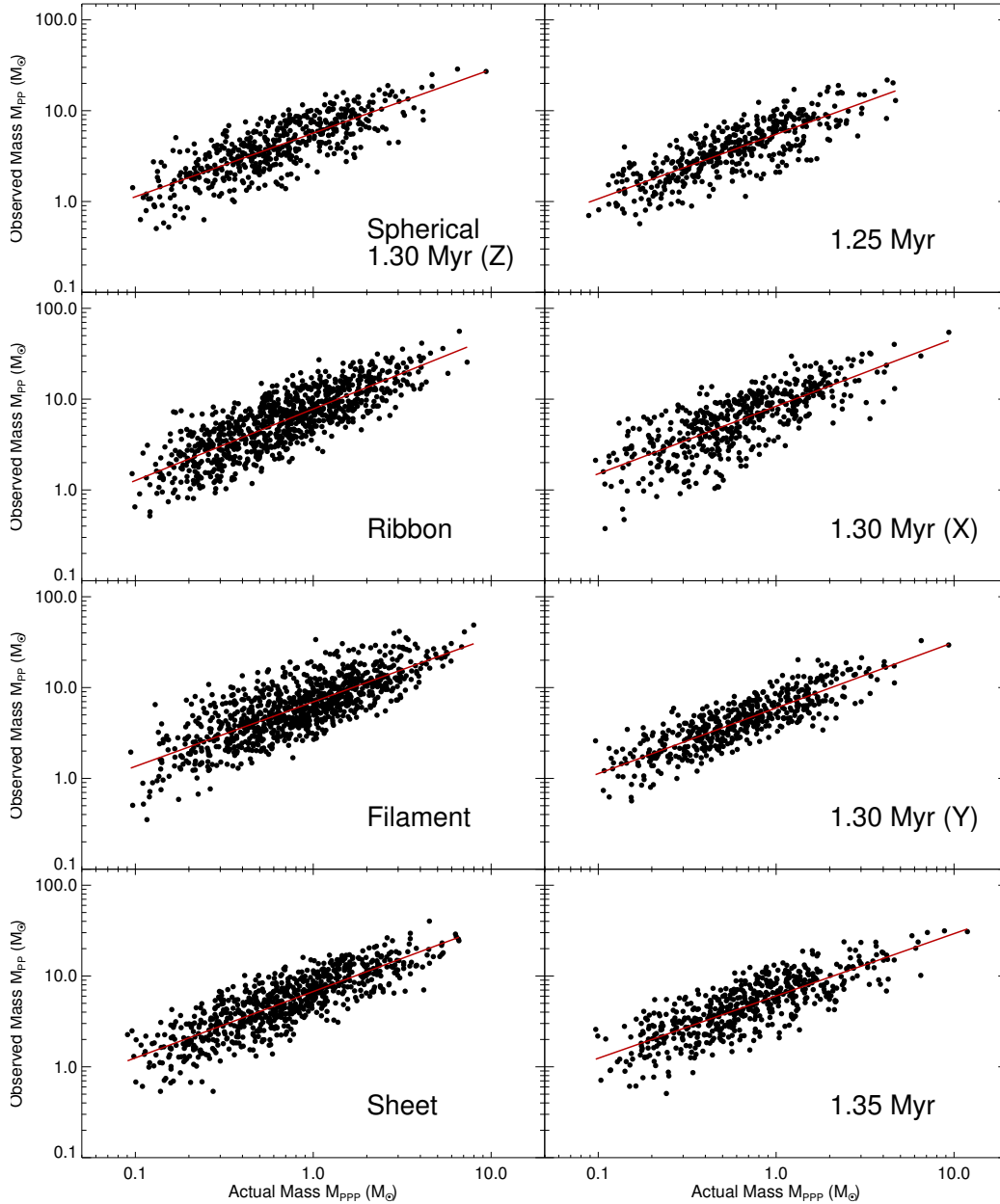


Figure 4.9: Log-log plot of the “observed” mass (PP) vs. the “actual” mass (PPP) for various cases. Regardless of the age of the clumps, orientation, or initial collapse condition (Spherical, Ribbon, Filament, or Sheet), the trend remains consistent.

The ‘actual’ mass of the clump can be represented as:

$$M_{\text{PPP}} \propto \rho (R_{\text{PPP}})^3$$

where ρ is the density of the clump. The ‘observed’ mass is calculated using the column density, Σ , and the projected radius, R_{PP} :

$$M_{\text{PP}} \propto \Sigma (R_{\text{PP}})^2$$

If we assume that the actual radius, R_{PPP} is approximately equal to the projected radius, R_{PP} , then we have the following relation:

$$M_{\text{PP}} \propto (M_{\text{PPP}})^{2/3}$$

This relation is within the uncertainties of the best functional fits from our data plots in Figures 4.8 and 4.9.

Based on this interpretation, the proportionality constant is equal to $\Sigma/\rho^{2/3}$ which is in units of $M_{\odot}^{1/3}$. From the best fit parameters, this proportionality constant is equal to $(7 \pm 1) M_{\odot}^{1/3}$ on average. This constant is likely related to the contribution from the column of gas along the line of sight. It is possible that an accurate estimate of the core mass can be obtained by utilizing the relationship between the surface area and the volume of the core. If we rearrange the formula for the projected mass, M_{PP} in units of solar masses, to solve for the physical mass, M_{PPP} , we find

$$M_{\text{PPP}} = \left(\frac{M_{\text{PP}}}{(7 \pm 1) M_{\odot}^{1/3}} \right)^{3/2}$$

The proportionality constant may also be related to the ratio of the mean observed mass of the identified clumps to the mean actual mass, $\bar{M}_{\text{PP}}/\bar{M}_{\text{PPP}}$.

As mentioned previously, the observed masses are, on average, ~ 6 times larger than the actual masses for the 1.30 Myr (z) case, and the proportionality constant, c , also happens to be equal to 6 ± 1 for the same case.

It is very likely that the proportionality constant does have a dependence on other factors than those mentioned previously, such as the turbulent velocity spectrum of the cloud. However, there has yet to be a proven method of determining the proportionality constant observationally. Regardless of the particular nature of the factor, our results have shown that clump mass estimates extracted from continuum data will be consistently overestimated due to low density gas and multiple objects along a line of sight. Since we have also shown that we are able to produce a similar result as Alves et al. (2007), where we identified a shift between mass functions by a factor of approximately 3 – 4, it is not practical to draw conclusions from continuum data regarding the star formation efficiency, due to the effects arising from projection.

4.2.3 Clump Correlations, Round Two: PPV vs. PPP

Our goal is to directly compare clumps identified in a PPP cube with those identified in a PPV spectral line data cube. We wish to compare physical properties of PPP clumps to the observed properties of the same clumps represented in a PPV data cube, thus a modified correlation method is necessary. Using a method similar to the correlation method proposed in Section 4.2.2.1, we are able to achieve this by using a mask to track the exact clumps from the PPP cube and trace them onto the PPV cube.

In order to obtain a PPV mask of the desired clumps from the PPP cube, we first removed all emission from the PPP cube which had not been assigned to a clump. The clump assignment file, used previously to create the PP mask, was used to select only the pixels which had been assigned to clumps. Using the same correlation method as before, we obtained the (x,y) pixel coordinates of the PPP clumps to create a 2D mask. However, we also need to determine the mean velocities of the PPP clumps in order to correlate the clumps in (x,y,z) coordinate space to (x,y,v_z) coordinate space.

The mean velocity and velocity dispersion of each of the PPP clumps were determined using the intrinsic velocities of the particles in the simulation. The mean velocity for each clump, \bar{v} , was calculated relative to the centre of mass velocity, $\vec{v}_{CoM} = \sum_i m_i \vec{v}_i / \sum_i m_i$. We are only concerned with the mean velocity along the line-of-sight, \bar{v}_z , for comparison with the PPV cube. We calculate \bar{v}_z using the following equation:

$$\bar{v}_z = \sum_i (v_{zi}) / N_c$$

The velocity dispersion, σ_z , was determined by the equation

$$\sigma_z^2 = \sum_i \frac{(v_{zi} - \bar{v}_z)^2}{N_c}$$

All summations are over the total number of particles, N_c , belonging to that clump. Once the mean velocity and velocity dispersion of each clump are known, we use these values to estimate two ranges of velocities, $[\bar{v}_z - \sigma_z/2, \bar{v}_z + \sigma_z/2]$ and $[\bar{v}_z - \sigma_z, \bar{v}_z + \sigma_z]$ to represent the range of velocity channels spanned by a Doppler-broadened line profile in the velocity spectrum. We have chosen two ranges of velocities to demonstrate the effect a velocity cut can have on

the outcome of clump properties. Figure 4.10 shows the velocity spectrum for a given line of sight which intersects the most massive clump identified in the PPP data cube.

The *collapse* task from the KAPPA software package of Starlink allows the user to extract a section of the cube and collapse the extracted slab over a limited range of values. For each clump, we are able to specify the specific velocity bins we would like to extract from the PPV cube. The resultant cube is then collapsed over this limited range. This removes all gas moving along the line of sight at velocities outside of the designated range of values. All that remains in the collapsed PPV cube is emission from particles moving at line-of-sight velocities between $\bar{v}_z - \sigma_z/2$ and $\bar{v}_z + \sigma_z/2$ (or $\bar{v}_z - \sigma_z$ and $\bar{v}_z + \sigma_z$).

We then applied the 2D mask with the (x,y) pixel coordinates of the PPP clumps to the collapsed PPV cube. Most clump-finding algorithms assume that the velocity coordinate, v_z , of a clump is somehow linked to its position along the line of sight, z . Thus, the mass of a clump can be over-estimated by including material which may happen to be moving at the same velocity as the clump, but is spatially separated along the line of sight. The mass estimates of the PPV correlated clumps can provide insight into how much additional unbound material may be moving at similar velocities as identified clumps.

4.2.3.1 Global Properties

Our first goal is to study the effect of a molecular tracer on clump identification using Clumpfind on our synthetic PPV data cubes. We have produced two PPV data cubes (see Chapter 3): one containing all of the emission along

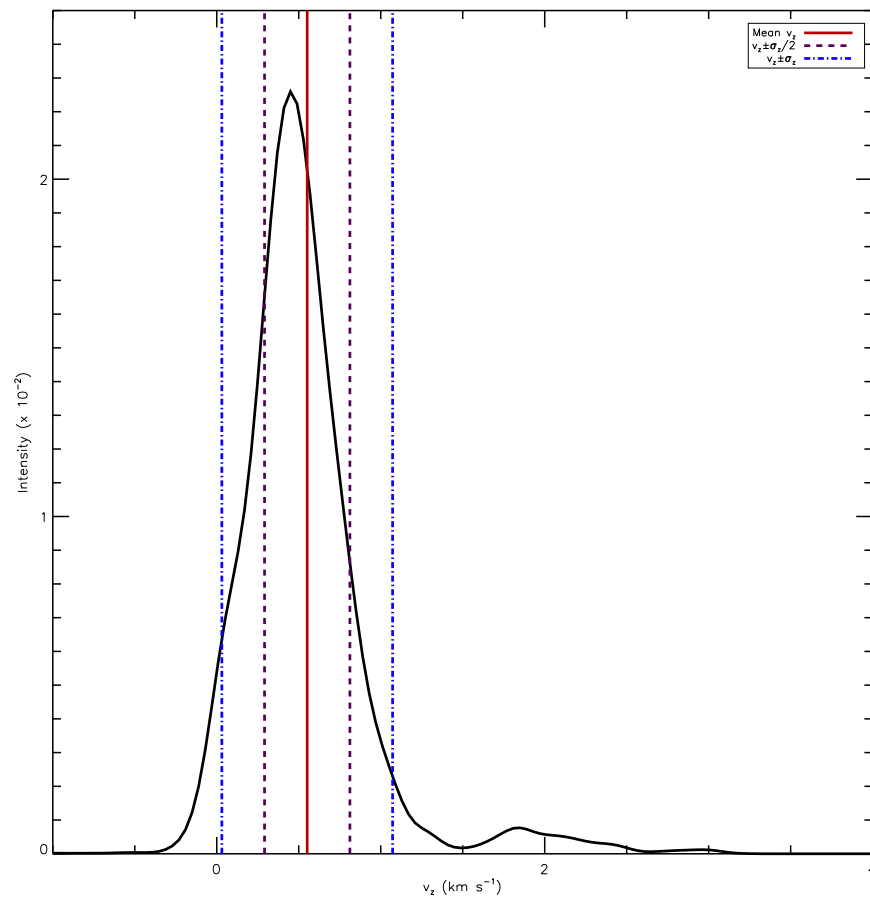


Figure 4.10: Velocity spectrum for a single line of sight. The mean velocity, \bar{v}_z , and velocity ranges, $[\bar{v}_z - \sigma_z/2, \bar{v}_z + \sigma_z/2]$ and $[\bar{v}_z - \sigma_z, \bar{v}_z + \sigma_z]$, are shown to demonstrate the velocity cuts made by our correlation method.

the line of sight and one with a density range of $1.8 \times 10^3 - 10^6 \text{ cm}^{-3}$, containing only the gas emission traced by the NH_3 (1,1) line transition.

The maximum pixel value in the synthetic PPV data cube containing all of the gas is approximately $0.05 \text{ M}_\odot/\text{pixel}/\text{velocity channel}$ and, since most PPV spectral-line observations tend to have a very limited dynamic range of 10 – 100, we used an rms noise value of $0.005 \text{ M}_\odot/\text{pixel}/\text{velocity channel}$ for a PPV cube with a spatial resolution of $6000 \text{ AU}/\text{pixel}$ and a velocity resolution of 0.04 km s^{-1} . Setting the lowest density contour level to 3σ and the contour increment to 2σ resulted in the identification of 50 clumps by Clumpfind which contain $\sim 175 \text{ M}_\odot$ of material or $\sim 3.5\%$ of the total mass in the simulation. Clumpfind returned the ‘integrated intensity’, or mass, and peak (x,y,v_z) positions of each clump.

We find that for the PPV case where only the densest gas is traced by the NH_3 molecule ($1.8 \times 10^3 < \rho < 10^6 \text{ cm}^{-3}$), 18 clumps were identified with a total clump mass of $\sim 24 \text{ M}_\odot$. The total clump mass is approximately 0.5% of the total mass in the simulation. While there are 32 fewer clumps than found in the idealized case (a reduction of 65%), the total clump mass is reduced by approximately 90% . This mass difference indicates that, although the gas may be confined in velocity space, there is a great dependence on the molecular tracer, as there are still contributions from low density gas contaminating the data.

Clumpfind identifies objects in PPV data cubes and assumes that material moving at the same velocity is not confused in projection. Figure 4.11 shows that, even though large amounts of material may be moving at the same

velocity as a clump, this material can still be spatially separated from the clump along the line of sight. Since Clumpfind cannot distinguish where the gas is positioned along the line of sight, the additional material is included in clump mass estimates and the determination of other clump properties.

From Section 4.2.1, the total mass contained in clumps in the PPP cube is $\sim 430 M_{\odot}$. Using the correlation method (described in Section 4.2.3) to locate PPP clumps in the PPV data cube, the total mass contained in clumps from the masked PPV cube is $\sim 445 M_{\odot}$ within $\sigma_z/2$ and $\sim 825 M_{\odot}$ within σ_z . A precise velocity cut can have the desired effect and produce a PPV ‘observed’ mass which is very near to the PPP ‘actual’ mass. Most of the extended emission moving at a similar line-of-sight velocity as the clump does not appear to contribute significantly in this case. As we widen the range of velocities to include more of the peaked distribution, the total PPV mass estimate increases to be greater than the total PPP mass estimate. This indicates that there is material comoving with the clumps, which are confused in projection along the line of sight. This additional material contributes to the mass estimate of the clumps, as the mass between the true PPP clumps and the estimates made from a PPV “observation” of these very clumps differs by a factor of 1 – 2. Figure 4.12 shows the mass distributions of the 499 clumps comparing PPP and PPV for both the $\sigma_z/2$ case and the σ_z case. Although the mass distribution created using the correlation method includes many more clumps than identified in the PPV cube using Clumpfind (50 or 18, depending on the case), our goal is to test the validity of Clumpfind and show whether or not it is a sensible method for identifying the *properties* of objects from PPV data cubes, regardless of the number of objects found.

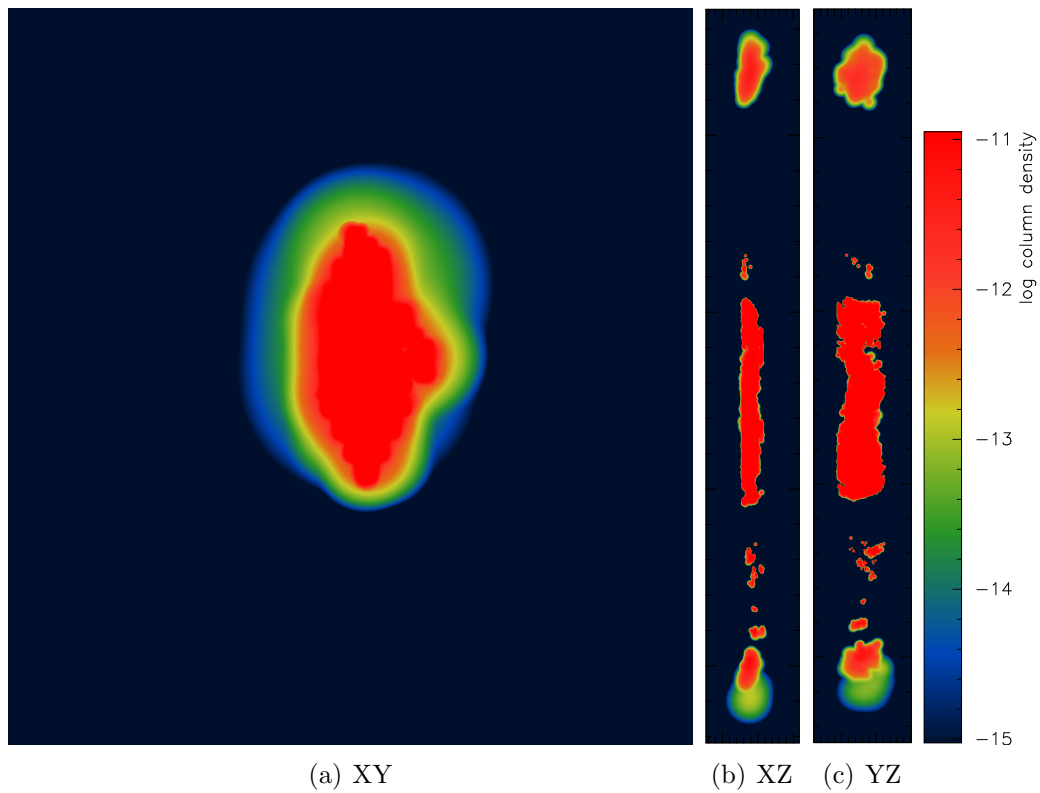


Figure 4.11: A PPV clump visualised in three dimensions with XY (left), XZ (centre), and YZ (right) projections. Large amounts of extended emission are present along the line of sight (the z-axis). This particular clump has a radius of approximately 0.2 pc in the XY-plane, but it also includes material along the line of sight which spans a distance of 2.5 pc. This large column of gas is evident in Figure 4.11(b) and 4.11(c).

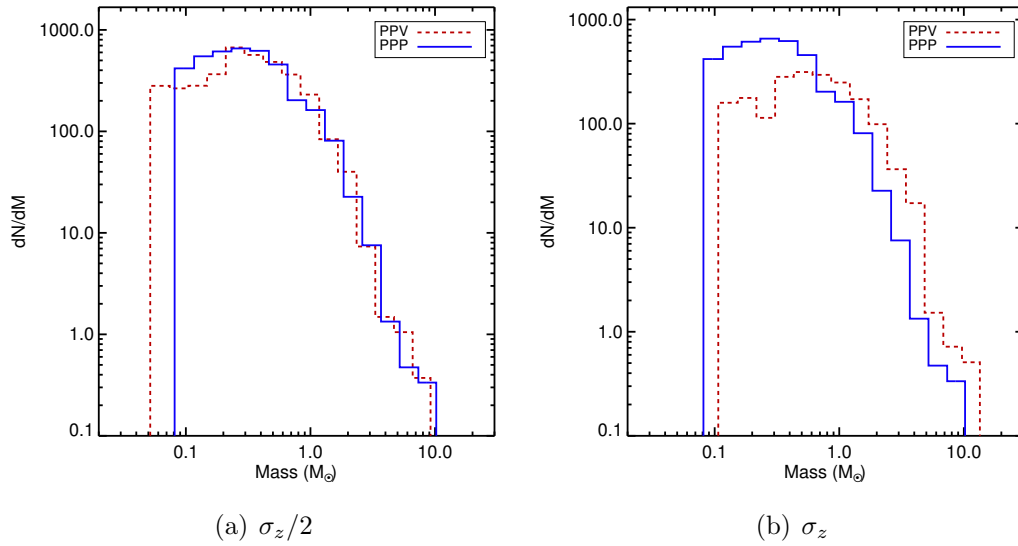


Figure 4.12: Clump mass function of the clumps identified in the PPP data cube (blue solid line) plotted with the clump mass function of the same clumps with their masses estimated from the (x,y,v_z) PPV data cube including all emission (red dotted line) for both the $\sigma_z/2$ case and the σ_z case.

This is a great improvement over the clump mass estimates from the correlated PP ‘observation’, especially for the $\sigma_z/2$ velocity range where there does not appear to be any significant difference between the mass distributions. We recall that this is an idealized case where all emission is included. For the PPV case where only the densest gas is traced by NH_3 , the total mass contained in clumps from this masked PPV cube is $439 M_\odot$. We have produced a clump mass function for the 499 clumps identified in the NH_3 PPV data cube, shown in Figure 4.13.

The PPV clump mass functions for both the idealized case using the $\sigma_z/2$ velocity range and the case where only NH_3 (1,1) emission is traced using the σ_z velocity range exhibit a remarkable correspondence to the true PPP clump mass function. We performed a two-sided Kolmogorov-Smirnov Test (KS-Test) to compare the PPV and PPP masses and determine whether they were drawn from the same distribution. For the $\sigma_z/2$ case and the case where only NH_3 (1,1) emission is traced, there was a 14% probability and an 81% probability, respectively, that the PPV and PPP masses were drawn from the same distribution. Based on these results, it appears that clump properties derived from PPV spectral-line data cubes are capable of being quite representative of the true physical properties of the clumps.

4.2.3.2 Clump-by-Clump Comparison

Using the masses obtained for each of the 499 clumps from the correlation method, we plotted the “observed” PPV masses of each clump against their corresponding “actual” PPP masses to perform a direct clump-to-clump com-

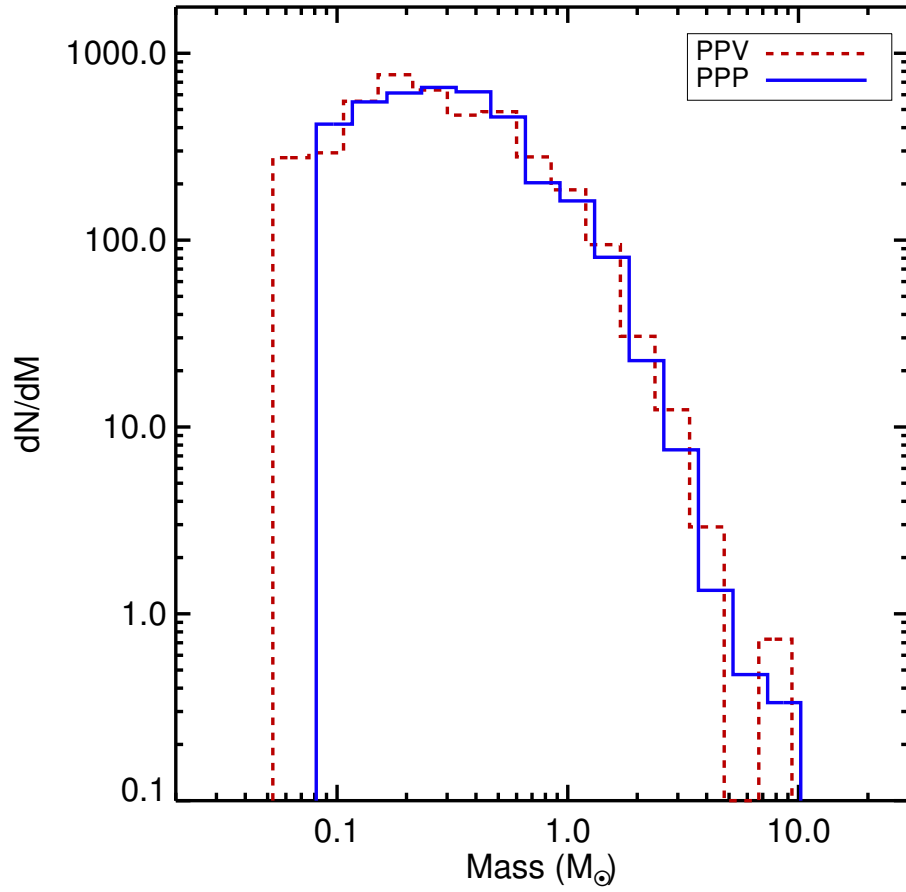


Figure 4.13: Clump mass function of the clumps identified in the PPP data cube (blue solid line) compared to the clump mass function of the same clumps with their masses estimated from the NH_3 (1,1) emission of the (x,y,v_z) PPV data cube (red dotted line).

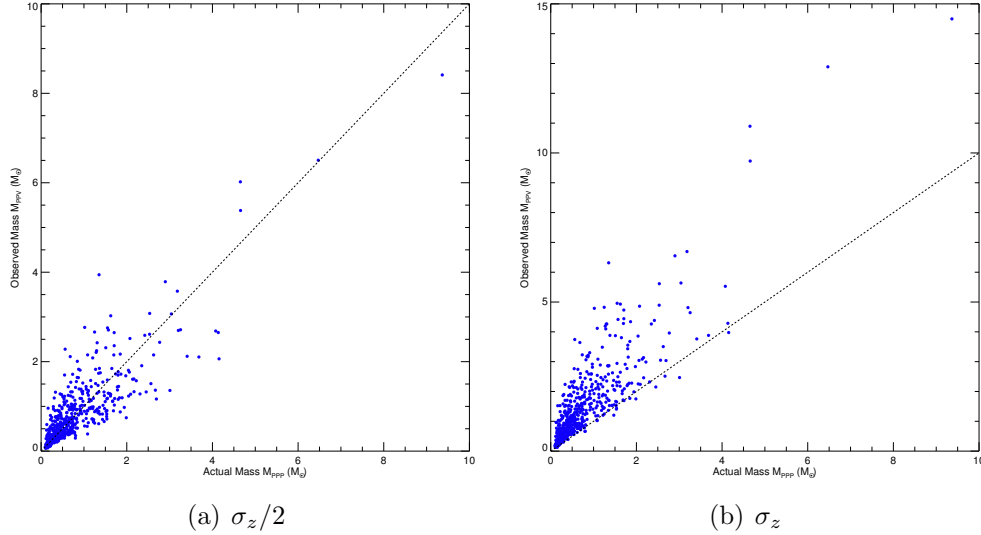


Figure 4.14: Plots of the “observed” mass (PPV) vs. the “actual” mass (PPP) for the $\bar{v}_z \pm \sigma_z/2$ and $\bar{v}_z \pm \sigma_z$ cases. The dashed black line is the 1-to-1 line.

parison of the masses. Figure 4.14 shows the relationship between the masses for both the $\bar{v}_z \pm \sigma_z/2$ and $\bar{v}_z \pm \sigma_z$ cases. We note that in both cases as the objects become more massive in PPP space, the PPV masses also increases. For the $\bar{v}_z \pm \sigma_z/2$ case, the ratio between the observed masses and actual masses are approximately 1:1 on average. The ratio is slightly larger for the $\bar{v}_z \pm \sigma_z$ case, where the observed masses are, on average, ~ 2 times larger than the actual masses. For this case, the observed masses appear to be an upper bound on the true masses of the objects. If the masses measured from a PPV data cube are true representations of the mass of the object, we would expect all of the data points to fall on or near the one-to-one line, shown as a dashed black line in Figure 4.14, which they do for the $\bar{v}_z \pm \sigma_z/2$ case.

The data lie very near to the one-to-one line, with linear fits to the data for each case of

$$\begin{aligned}
M_{\text{PPV}} &= (0.10 \pm 0.04) + (0.75 \pm 0.06)M_{\text{PPP}} & \bar{v}_z - \frac{\sigma_z}{2} < v_z < \bar{v}_z + \frac{\sigma_z}{2} \\
M_{\text{PPV}} &= (0.19 \pm 0.06) + (1.41 \pm 0.09)M_{\text{PPP}} & \bar{v}_z - \sigma_z < v_z < \bar{v}_z + \sigma_z
\end{aligned}$$

where the uncertainties are the standard deviations of the best fit parameters. These results demonstrate once again that the observed PPV masses are well-matched to the actual PPP masses of the clumps.

We have also plotted the data on a log-log plot in Figure 4.15 for comparison to our M_{PP} vs. M_{PPP} results from Section 4.2.2.2. A function of

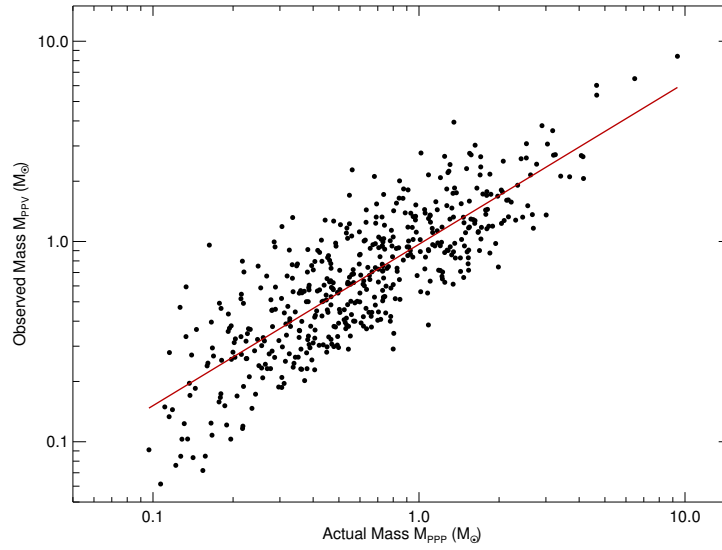
$$M_{\text{PPV}} = (M_{\text{PPP}})^{0.8}$$

was fit to the data for the $\bar{v}_z \pm \sigma_z/2$ case with a reduced chi-squared of 3.9×10^{-2} and a function of

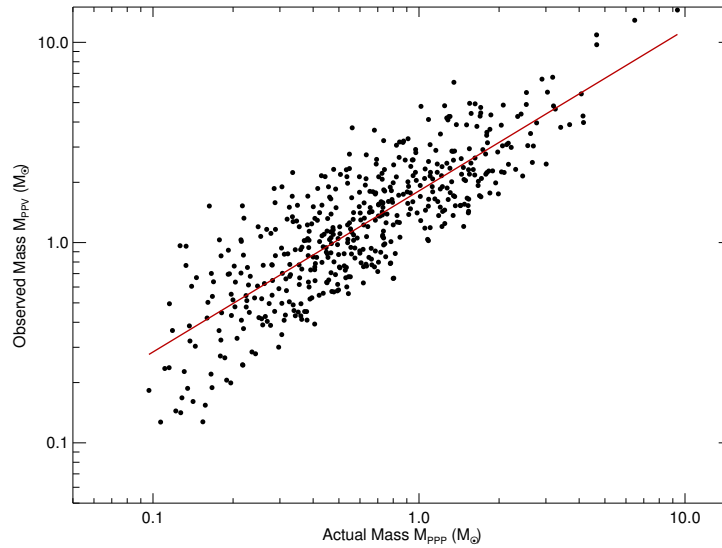
$$M_{\text{PPV}} = 2(M_{\text{PPP}})^{0.8}$$

was fit to the data for the $\bar{v}_z \pm \sigma_z$ case with a reduced chi-squared of 3.7×10^{-2} . The relation has considerable scatter and is not as tightly correlated as seen previously with the PP – PPP comparison, thus it seems that a linear fit is better suited to these data.

For the $\bar{v}_z \pm \sigma_z$ case, Figure 4.16 compares the relationship between the observed and actual masses derived from the idealized PPV cube, shown in Figure 4.14(b), to the relationship between the masses estimated from the

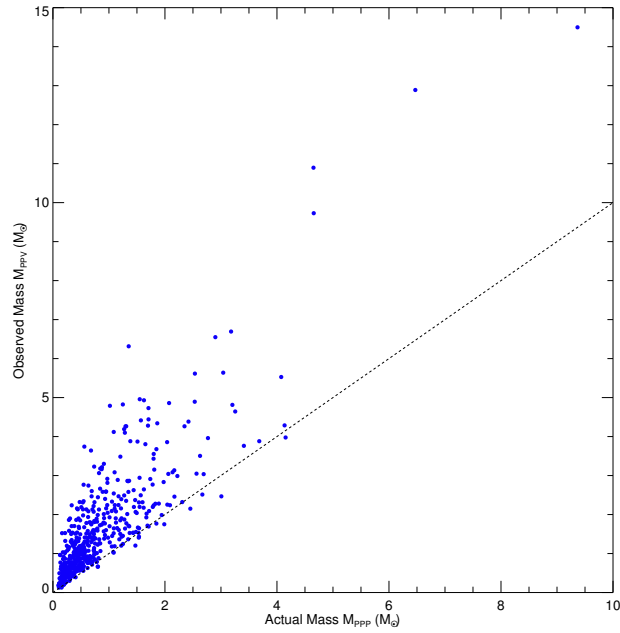


(a) $\sigma_z/2$

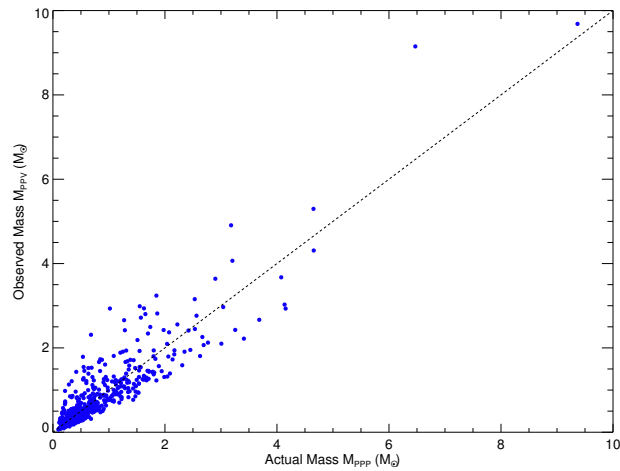


(b) σ_z

Figure 4.15: Log-log plots of the “observed” mass (PPV) vs. the “actual” mass (PPP) for the $\bar{v}_z \pm \sigma_z/2$ and $\bar{v}_z \pm \sigma_z$ cases. Fits to the data are shown as solid red lines.



(a) All Emission



(b) NH₃

Figure 4.16: Plots of the “observed” mass (PPV) vs. the “actual” mass (PPP) for the $\bar{v}_z \pm \sigma_z$ case comparing the PPV masses obtained using all emission and the PPV masses obtained from only the highest density gas traced by NH₃.

Table 4.4: Table of Best Fit Parameters to $M_{\text{PPV}} = c(M_{\text{PPP}})^m$

	$c (M_{\odot})$	m
All emission	2 ± 1	0.8 ± 0.1
NH ₃ emission	1 ± 1	0.9 ± 0.1

NH₃ (1,1) emission of the PPV data cube. Table 4.4 summarizes the best fit parameters for the two cases.

Although Table 4.4 summarizes the best fit parameters to the function, $M_{\text{PPV}} = c(M_{\text{PPP}})^m$, the data shown in Figure 4.16(b) can also be represented very accurately by a linear fit:

$$M_{\text{PPV}} = (0.01 \pm 0.04) + (0.90 \pm 0.07)M_{\text{PPP}} \quad \bar{v}_z - \sigma_z < v_z < \bar{v}_z + \sigma_z$$

Our results demonstrate that the mass estimates of clumps identified in three spatial dimensions correlate well with the mass estimates determined using velocity cuts of a PPV data cube, as they differ by only a factor of 1 – 2.

We see that for the clump-to-clump comparisons, as for the clump mass functions, the observed PPV masses derived from both the idealized case using the $\sigma_z/2$ velocity range and the case where only NH₃ (1,1) emission is traced using the σ_z velocity range follow a one-to-one relationship with the actual PPP masses of the clumps and are the best methods for accurate estimation of clump properties.

4.3 Boundedness

Up until this point, we have assumed that the clumps identified are candidates for star formation. However, it is quite difficult to tell observationally

whether a clump is transient in nature and will dissipate, or whether it is gravitationally bound and will continue to collapse and form stars. Clumpfind is an automated algorithm and thus each clump identified may not necessarily be bound. It is for this reason we have previously used the term, ‘candidates’, when describing the clumps identified by Clumpfind. In this section, we are able to use the properties of the SPH particles assigned to our clumps to divide our clump candidates from the PPP cube into one of two classifications: an unbound, starless core or a bound, prestellar core. The boundedness test demonstrates the frequency at which clumps observed in PP and PPV correspond to physical objects in the simulation, tests the robustness of the clump-finding methods, and can also give an indication of how often multiple objects are confused in projection along the line of sight in observations.

The main purpose of creating the PPP cube is to answer two key questions: what fraction of clumps are bound, and what fraction of particles are bound to each clump? Using the clumps, as they have been identified by Clumpfind in the PPP cube, we are able to determine which particles in the simulation contribute to each clump. By knowing this information, we can calculate many properties of the clumps using the known properties of the particles.

The first question we asked was whether each clump was bound as a whole. This gives an indication as to the fraction of clumps which are bound in the sample. For each clump, we calculated the energies relative to the centre of

mass position, \vec{x}_{CoM} , and centre of mass velocity, \vec{v}_{CoM} , of the clump, given by

$$\begin{aligned}\vec{x}_{CoM} &= \frac{\sum_i m_i \vec{x}_i}{\sum_i m_i} \\ \vec{v}_{CoM} &= \frac{\sum_i m_i \vec{v}_i}{\sum_i m_i}\end{aligned}$$

which sum over the total number of particles belonging to that clump. The potential energy, kinetic energy, and thermal energy of each clump were then calculated using the following formulae:

$$\begin{aligned}U &= - \sum_{i=0}^{N_c-1} \frac{G m_i M_{tot}}{|\vec{x}_i - \vec{x}_{CoM}|} \\ K &= \frac{1}{2} \sum_{i=0}^{N_c-1} m_i (\vec{v}_i - \vec{v}_{CoM})^2 \\ E_{th} &= \sum_{i=0}^{N_c-1} m_i u_i\end{aligned}$$

where N_c is the number of particles in the clump and u_i is the internal energy density of the gas. The internal (or thermal) energy density is given by

$$u_{th} = \frac{3}{2} \frac{kT}{\mu m_H} = \frac{3}{2} c_s^2$$

where $c_s = 1.84 \times 10^4$ cm/s is the speed of sound in an isothermal gas at 10 K (Bate & Bonnell, 2005). The mean molecular weight, μ , is chosen to be 2.46, resulting in a value of $u_{th} = 5.0 \times 10^8$ ergs g^{-1} .

An object which is gravitationally bound satisfies the following equation:

$$E_{tot} = U + K + E_{th} < 0$$

Table 4.5: Table of Initial Boundedness Test Results

	# of clumps	# of bound clumps
Spherical	499	61 (12%)
Ribbon	900	112 (12%)
Filament	935	137 (15%)
Sheet	732	97 (13%)

We found the fraction of clumps which were initially bound overall for the clumps identified by Clumpfind in the PPP cube (Section 4.2.1). Out of 499 clumps, 61 clumps or $\sim 12\%$ were determined to be bound for the spherical collapse case. Table 4.5 compares this result to the number of initially bound clumps found for the other collapse cases. Each collapse case was at the same stage of cloud evolution and the clumps were identified from each PPP data cube using identical Clumpfind parameters. It is interesting to note that the filament case shows the highest number of initially bound clumps, especially considering that filaments are currently believed to be a key component of star formation.

This analysis was repeated for clumps identified by Clumpfind2d in the PP column density map. The fraction of bound clumps in the PPP cube is much larger than the fraction of bound clumps identified in the PP column density map at 0.2%. Table 4.6 shows how the fraction of bound clumps identified from the PP column density map is not affected by changes in the Clumpfind2d parameters. However, on inspection of these bound ‘clumps’, we notice that not only are they located at the outer edges of the cloud, but they are also very large and primarily composed of diffuse gas, far from regions

Table 4.6: Table of PP Boundedness Test Results

RMS (σ)	Low	Step	# of clumps	# of bound clumps
0.005 M_{\odot}/px	3σ	2σ	886	2 (0.2%)
0.006 M_{\odot}/px	3σ	2σ	558	4 (0.7%)
0.007 M_{\odot}/px	3σ	2σ	532	4 (0.7%)
0.006 M_{\odot}/px	5σ	3σ	455	4 (0.7%)
0.005 M_{\odot}/px	5σ	3σ	503	3 (0.6%)

of high-density. These results indicate that Clumpfind2d is not an effective method of identifying truly bound structures in continuum data.

For the clumps identified by Clumpfind in the PPV data cube, there were initially 4 bound clumps out of 50 identified clumps for the case with total emission and initially 2 bound clumps out of 18 identified clumps for the case with only NH_3 (1,1) emission. The introduction of a molecular tracer does not seem to significantly increase the fraction of bound clumps identified for the PPV case. Although the effect of low density gas contributing to clump mass estimates is minimized when a dense gas tracer is used, in terms of boundedness, there seems to be little improvement to the identification of bound clumps from a PPV data cube, regardless of the molecular tracer used.

The second question we explored was whether a large fraction of the particles in a clump were bound together or if some particles were, in fact, entirely unbound based on their individual energies rather than the total energy of the clump as a whole. By determining the fraction of particles bound to each clump, we are able to understand the transience of objects evident in this early stage of star formation. Many dense bound objects appear to form during the collapse of the molecular cloud, but it is possible that they may be

only transient in nature if their evolution was followed further. The fraction of bound objects which still remain bound several free-fall times later is an interesting idea to explore; however, it is beyond the scope of this thesis and the simulation we are analysing.

For each clump identified by Clumpfind in the PPP cube, we determined which particles in the simulation contributed to that clump. We used these particle identifiers to select only the particles of interest in the simulation and we were able to extract the properties of these particles from the diagnostic output of the simulation itself.

In order to determine whether a particle is bound to a specific clump, we used previously-calculated centre of mass position, \vec{x}_{CoM} , and centre of mass velocity, \vec{v}_{CoM} , of the clump. The energies of the particles were calculated relative to this position and velocity.

The potential energy, kinetic energy, and thermal energy of each particle were calculated using the following formulae:

$$\begin{aligned} U(i) &= m_i \phi_i \\ K(i) &= \frac{1}{2} m_i (\vec{v}_i - \vec{v}_{CoM})^2 \\ E_{th}(i) &= m_i u_i \end{aligned}$$

where ϕ is the potential of the particle calculated by Gasoline using the tree-solving method discussed in Chapter 2.

Particles which do *not* have a total energy less than zero are removed from the calculation. All other particles with negative total energies contribute to a new centre of mass velocity and the energies are recalculated with these

remaining particles. The particles with positive total energies continue to be removed until every particle that remains is bound to the centre of mass of the clump. We then re-ran this iterative test of boundedness with the final centre of mass velocity fixed to ensure that particles were not unnecessarily removed from the clump, due to variations in the centre of mass during the multiple calculations.

The new final total energies were calculated by

$$\begin{aligned}
 U &= \frac{1}{2} \sum_{i=0}^{N_c-1} m_i \phi_i \\
 K &= \frac{1}{2} \sum_{i=0}^{N_c-1} m_i (\vec{v}_i - \vec{v}_{CoM})^2 \\
 E_{th} &= \sum_{i=0}^{N_c-1} m_i u_i
 \end{aligned}$$

Once we were able to determine the fraction of particles bound to each clump, we were able to determine estimates for many of the clump's properties. By calculating the final mass (M_f), the radius that encloses half the total mass ($R_{1/2}$), and total energy, we are able to classify these objects as starless or prestellar cores, based on their boundedness, size (< 0.1 pc), and average density ($> 10^4 \text{ cm}^{-3}$). Out of the 499 clumps identified from the PPP cube at 1.30 Myr from initial collapse, there were 11 bound clumps remaining. The boundedness test showed that, although a clump may seem initially bound as a whole, it is actually composed of many particles which do not have strong enough gravitational potential energies to withstand their escape. The majority of clumps have their particles kicked out by our algorithm until there are no particles remaining.

Table 4.7 lists several properties of the 11 bound prestellar cores, including the centre of mass velocity $((v_x, v_y, v_z)_{com})$, the non-thermal one-dimensional velocity dispersion (σ_{1d}) , the half-mass radius $(R_{1/2})$, the mean density $(\bar{\rho} = M_f/R_{1/2}^3)$, and the virial parameter (α_{vir}) , which was previously discussed in Chapter 2.

Table 4.7: Properties of the ‘‘Prestellar Cores’’ at 1.30 Myr

Core	M_f (M_\odot)	$(v_x, v_y, v_z)_{com}$ (km/s)	σ_{1d} (km/s)	$R_{1/2}$ (AU)	$\bar{\rho}$ (cm^{-3})	α_{vir}
1	7.57	(-0.32, -0.46, 0.41)	0.29	12979	1.2×10^6	0.988
2	3.38	(-0.15, 0.02, 0.80)	0.22	10599	1.0×10^6	1.072
3	2.83	(-1.16, -0.42, 2.43)	0.19	10488	8.7×10^5	0.976
4	2.82	(-1.39, -1.62, 0.73)	0.18	12325	5.4×10^5	0.966
5	2.60	(-0.19, -0.58, 0.50)	0.19	9552	1.1×10^6	0.966
6	2.22	(-0.26, 0.18, 0.67)	0.17	11202	5.6×10^5	0.950
7	1.98	(-1.31, 0.02, 1.45)	0.16	9518	8.2×10^5	0.822
8	1.95	(-1.19, -0.22, 1.38)	0.15	10776	5.5×10^5	0.882
9	1.55	(-0.85, -0.41, 2.12)	0.15	9010	7.5×10^5	0.888
10	1.48	(-1.68, 1.64, 1.35)	0.12	7538	1.2×10^6	0.560
11	1.11	(-0.89, -1.95, 2.27)	0.11	7603	9.0×10^5	0.650

Each bound clump is less than 0.1 pc in size, has a density of $\sim 10^6 \text{ cm}^{-3}$, and has $\alpha_{vir} = |2K/U| \leq 1$, which are all characteristics of prestellar cores. The mass function of the 11 bound prestellar cores is plotted in Figure 4.17 along with the mass functions of the 499 candidate clumps identified in the PPP data cube and in the PP column density map, shown previously in Figure 4.5. We see that the prestellar cores are at the high-mass end of the PPP CMF, indicating that the largest clumps are often bound and the remaining clumps are less massive, unbound, starless cores.

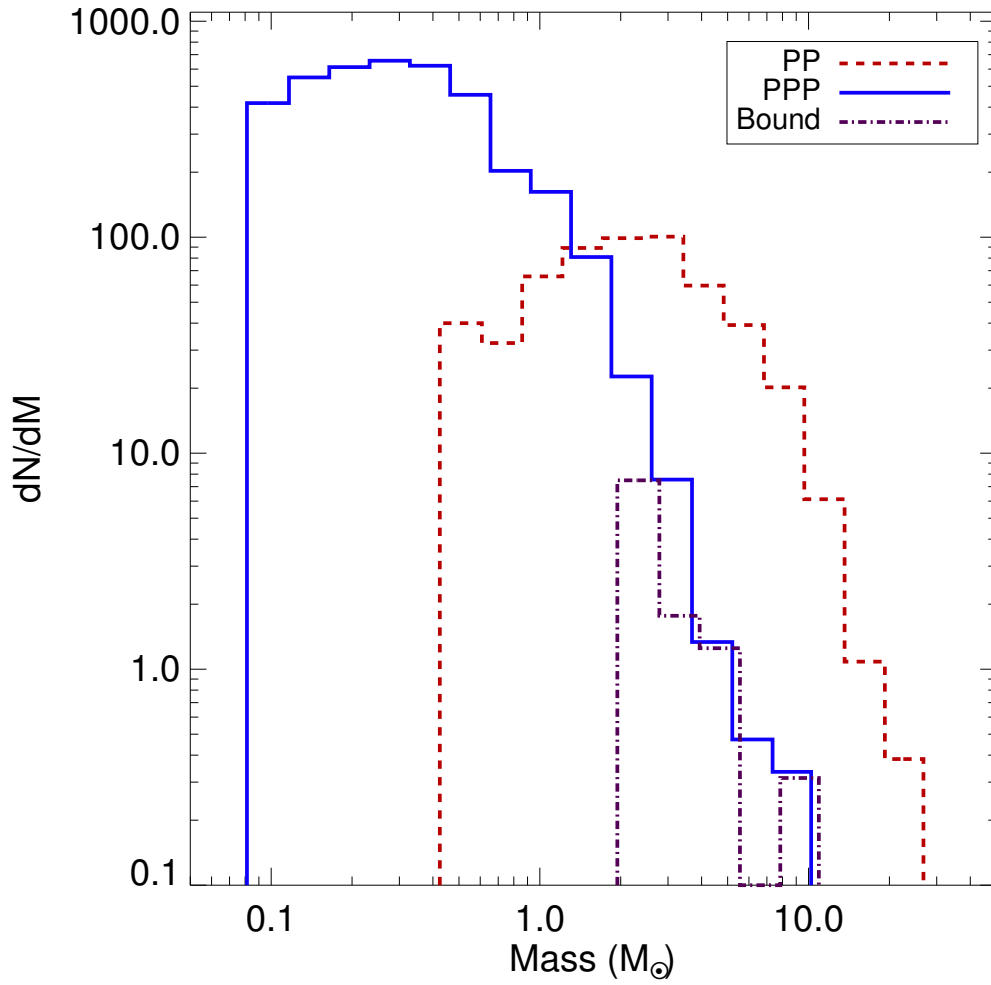


Figure 4.17: Prestellar core mass function (purple dotted line) plotted along with the CMF for clumps identified in the PPP data cube (blue solid line) and the CMF of the same clumps with their masses estimated from the PP column density map (red dotted line).

Table 4.8: Table of Boundedness Test Results

	# of clumps	# of bound clumps
1.25 Myr	435	3 (0.7%)
1.30 Myr (x)	499	11 (2.2%)
1.30 Myr (y)	498	11 (2.2%)
1.30 Myr (z)	499	11 (2.2%)
1.35 Myr	543	16 (2.9%)
1.30 Myr (Ribbon)	900	25 (2.7%)
1.30 Myr (Sheet)	742	23 (3.1%)
1.30 Myr (Filament)	935	35 (3.7%)

The boundedness test was applied to the other initial collapse cases (Ribbon, Sheet, and Filament) and also to earlier and later stages of clump evolution. The test also showed that for the 1.30 Myr PPP data cube, it was able to converge on the same 11 cores, regardless of orientation. These results are summarized in Table 4.8.

There are fewer bound clumps at earlier stages than at later stages, which highlights the rate of progression of the prestellar core formation. This result also reveals that, by tracking core locations, prestellar cores formed at early times in our simulation remain bound at later times. The filament case dominates in terms of the percentage of its clumps which were identified to be prestellar cores from the boundedness test, strengthening once again the relation between filaments and star formation.

For the most massive prestellar core identified in the 1.30 Myr PPP cube (Core 1 in Table 4.7), Table 4.9 lists the core's properties at different orientations and different stages of its evolution.

Table 4.9: Properties of the most massive “prestellar core” for various cases

	1.25 Myr	1.30 Myr	1.30 Myr (X)	1.30 Myr (Y)	1.35 Myr
M_i (M_\odot)	4.69	9.37	9.35	9.33	11.9
M_f (M_\odot)	2.21	7.57	7.56	7.54	10.5
x_{com} (pc)	-1.5	-1.5	-1.5	-1.5	-1.5
y_{com} (pc)	0.3	0.3	0.3	0.3	0.3
z_{com} (pc)	2.6	2.6	2.6	2.6	2.6
\bar{v} (km/s)	0.85	0.69	0.70	0.70	0.66
σ_{1d} (km/s)	0.20	0.29	0.29	0.29	0.54
$R_{1/2}$ (AU)	7338	12979	12958	12937	11635
R_{vir} (AU)	8397	12787	12762	12748	2285
$\bar{\rho}$ (cm^{-3})	2.0×10^6	1.2×10^6	1.2×10^6	1.2×10^6	2.4×10^6
K (ergs)	2.7×10^{42}	2.0×10^{43}	2.0×10^{43}	1.9×10^{43}	9.1×10^{43}
U (ergs)	-5.1×10^{42}	-4.0×10^{43}	-3.9×10^{43}	-3.9×10^{43}	-4.3×10^{44}
E_{th} (ergs)	2.2×10^{42}	7.6×10^{42}	7.6×10^{42}	7.6×10^{42}	1.1×10^{43}
E_{tot} (ergs)	-2.3×10^{41}	-1.2×10^{43}	-1.2×10^{43}	-1.2×10^{43}	-3.3×10^{44}
α_{vir}	1.046	0.988	0.988	0.988	0.426

By studying the most massive prestellar core along different lines of sight, we were able to confirm that all of our results are consistent, regardless of the orientation of the cloud. An indication of how the core properties evolve over time can also be seen in Table 4.9. The centre of mass remains constant over time; however, although the mass steadily increases, the radii estimates and average density fluctuate. We note also that the virial parameter decreases with increasing time, indicating that the core becomes more tightly bound as it evolves. As the core is increasing in mass and becoming more tightly bound, the velocity dispersion is increasing as well. The velocity dispersion of these objects will be discussed in greater detail in Section 4.4.

4.4 Connecting the Dots: Traceable Properties?

Our aim is to connect the true three-dimensional properties of the molecular cloud to observable line-of-sight properties, such as the virial parameter and the velocity dispersion, which can aid in the proper identification of physically real objects in the cloud.

The virial parameter is a key observable parameter which is often used to determine whether or not a clump is bound (e.g. Bertoldi & McKee, 1992; Heyer et al., 2001). We discussed the virial parameter in Chapter 2, where it was defined to be:

$$\alpha_{vir} = |2K/U|$$

The virial parameter defined by Bertoldi & McKee (1992) is approximately equal to $|2K/U|$ and is derived using only observable properties from molecular-line data, which allow an assumption to be made regarding the boundedness of an object. The Bertoldi & McKee (1992) equation for the virial parameter is:

$$\alpha_{vir} = \frac{5\sigma^2 R_c}{GM_c}$$

where $\sigma^2 = \sigma_{1d}^2 + c_s^2$ is the total velocity dispersion, R_c is the projected radius of the clump, and M_c is the estimated mass of the clump. If $\alpha_{vir} < 1$, then the object is bound. We have already shown that an observational estimate of the mass cannot always be trusted, particularly from extraction from continuum data. However, it is possible that the virial parameter will remain a useful tool for testing the boundedness of an object, despite the uncertainties in the estimates of the individual variables.

Figure 4.18 shows that, for all 499 clumps identified from the 1.30 Myr (z) case, the observed virial parameter, $\alpha_{vir} = 5\sigma^2 R_c / GM_c$, is a very close approximation to the theoretical virial parameter, $|2K/U|$. According to the virial parameter estimates, no clumps are bound prior to the boundedness test based on the initial properties of the clumps.

We have mentioned previously that once we strip off all the unbound particles, only 11 bound clumps remain. The boundedness in this case is determined by the negative total energy of each core. We see that these prestellar cores also have calculated virial parameters less than or approximately equal to 1. However, we see in Figure 4.19 that several of the corresponding observed virial parameters for each of these cores are *greater* than 1.

If there are cores which have $\alpha_{vir} > 1$, then these cores would be identified as being unbound by the observational test of gravitational boundedness. However, there are a number of authors (e.g. Larson, 1981; Shetty et al., 2010) who state that cores with $\alpha_{vir} \leq 2$ may also be gravitationally bound. Our results appear to agree with this statement, thus the observed virial parameter gives a good indication of the boundedness of star-forming cores from molecular-line data.

We mentioned in Chapter 2 that Larson’s third law, the size-linewidth relation, is expected to apply to small dense substructures within the molecular cloud. It was stated that the size-linewidth relation can be expressed as $\sigma \propto L^{1/2}$, provided that the GMCs have approximately constant column densities and are in virial equilibrium (Larson, 1981; Solomon et al., 1987). The non-

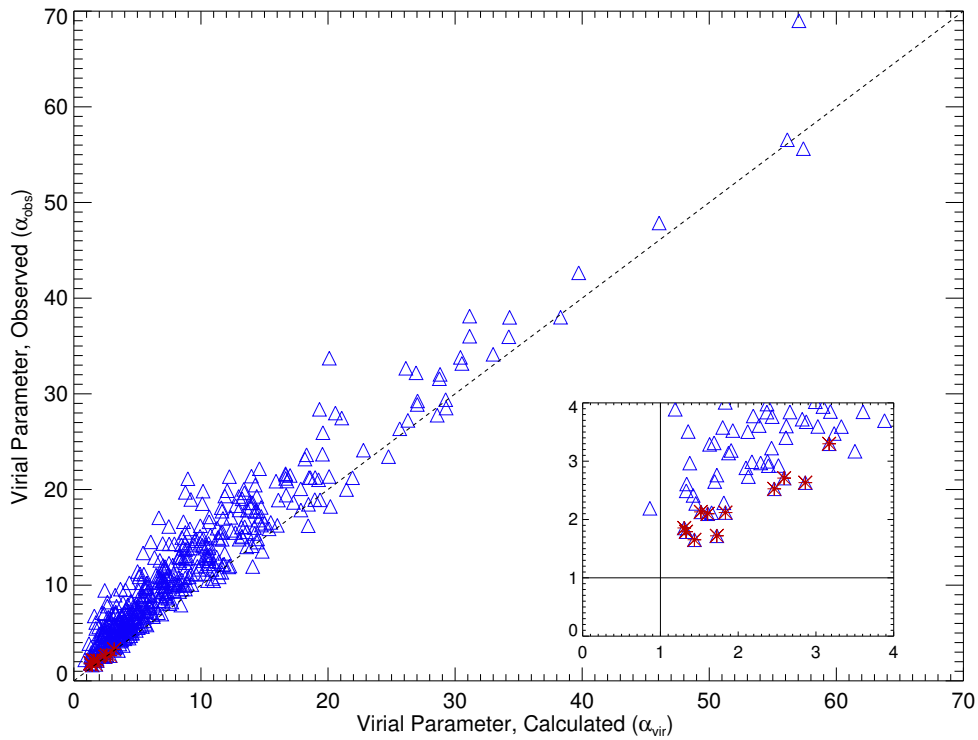


Figure 4.18: Plot of the relation between the observed and theoretical virial parameters. All candidate clumps are included using their initial properties. The calculated theoretical virial parameter equals $|2K/U|$ and the observed virial parameter is equal to $5\sigma^2 R_{1/2} / GM_i$, where $R_{1/2}$ is the half-mass radius and M_i is the initial PPP mass. The dashed black line is the 1-to-1 line and a zoom-in of the plot is shown as an inset. The red symbols mark the 11 candidate clumps which will eventually be classified as bound prestellar cores.

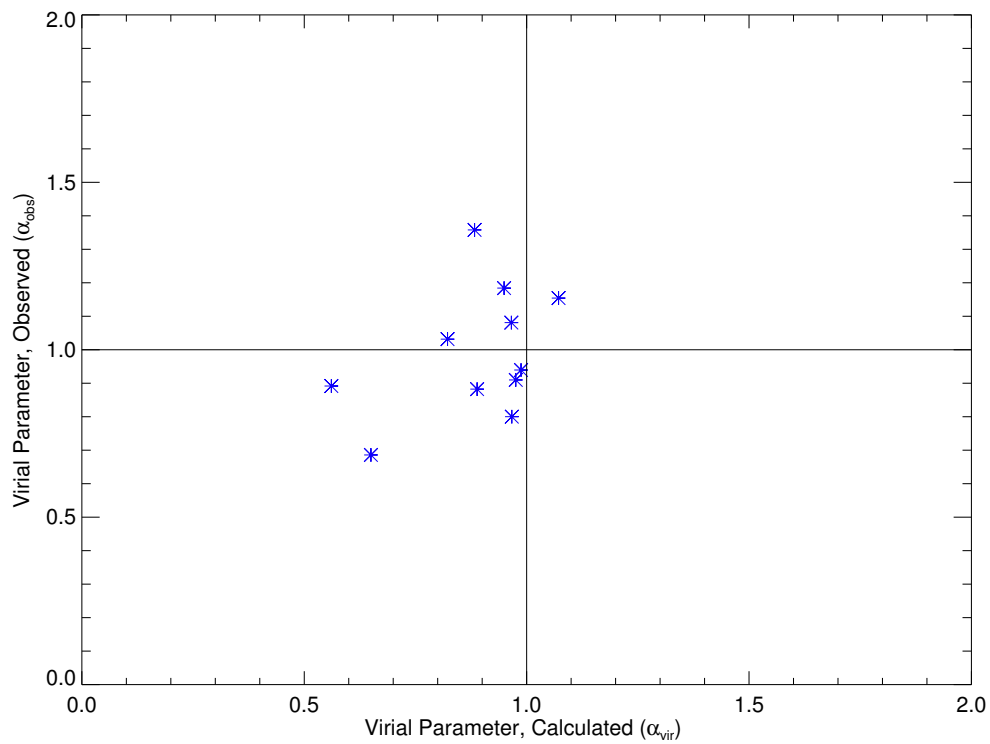


Figure 4.19: Plot of the relation between the observed and theoretical virial parameters for the bound prestellar cores. An object can be defined as bound if $\alpha_{\text{vir}} \leq 1$ in either axis.

thermal one-dimensional velocity dispersion, σ_{1d} , of each of the prestellar cores was determined by the equation

$$\sigma_{1d} = \sqrt{(\sigma_x^2 + \sigma_y^2 + \sigma_z^2) / 3}$$

where

$$\begin{aligned}\sigma_x^2 &= \sum_i \frac{(v_{xi} - \bar{v}_x)^2}{N_c} \\ \sigma_y^2 &= \sum_i \frac{(v_{yi} - \bar{v}_y)^2}{N_c} \\ \sigma_z^2 &= \sum_i \frac{(v_{zi} - \bar{v}_z)^2}{N_c}\end{aligned}$$

The values for σ_{1d} are listed in Table 4.7. The total linewidth for each core was calculated using the equation, $\sigma^2 = \sigma_{1d}^2 + c_s^2$, which includes a thermal contribution from the sound speed, and the results were plotted in Figure 4.20 against their corresponding sizes, equal to twice the half-mass radius.

There is considerable scatter and the limited number of data points result in large uncertainties in the estimate of the fit. The best fit to the data was determined to be

$$\sigma \propto L^{0.58 \pm 4.16}$$

We attempted to produce a similar size-linewidth relation for the unbound starless cores; however, the scatter was extremely large and no significant fit to the data could be obtained. The condition that the objects must be in virial equilibrium implies that unbound cores will not follow this relation, which is what we found when studying our starless cores.

According to recent studies by Pineda et al. (2010), it may be possible to identify these dense regions of star formation by the transition from supersonic

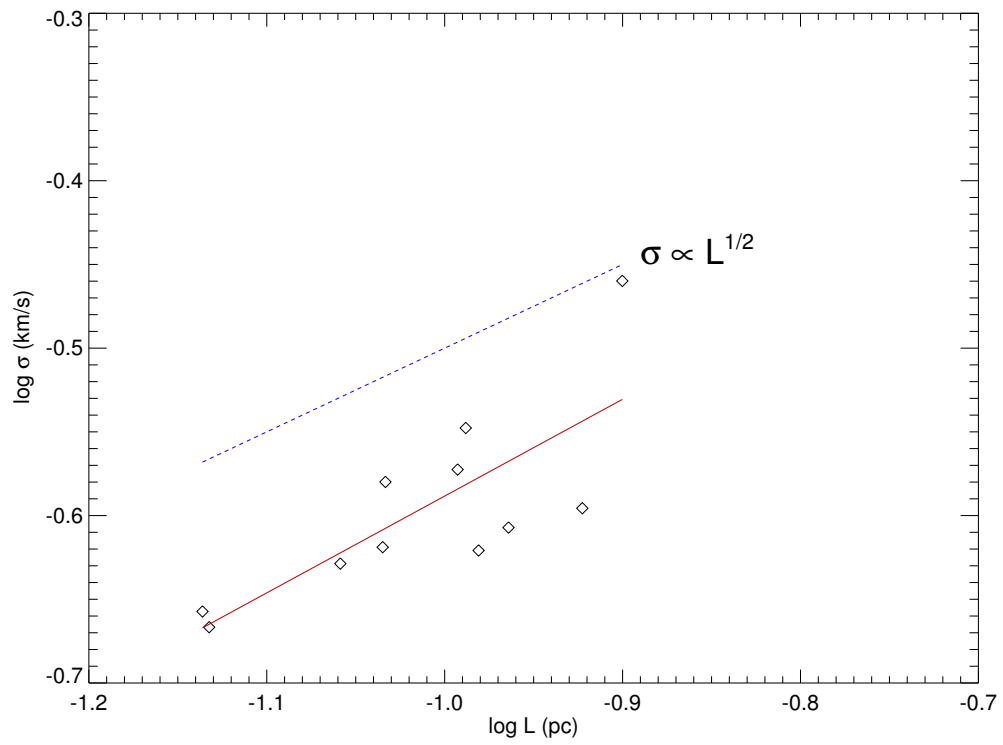


Figure 4.20: The size-linewidth relation for the prestellar cores. A fit to the data is shown as a red solid line and Larson's third law is shown as a blue dashed line.

to subsonic turbulence and the presence of low velocity dispersion in the cores. Maps of mean velocity and velocity dispersion for the molecular line emission tracer for dense gas, NH_3 , were created from the PPV spectral-line data cube (Figure 4.21). The intensity-weighted velocity and the intensity-weighted dispersion along the line of sight were produced using the *collapse* task from the KAPPA software package, a part of the Starlink software environment.

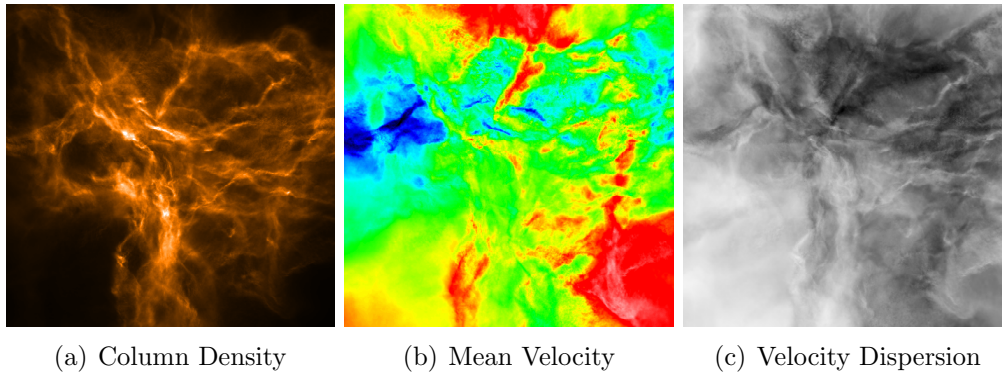


Figure 4.21: Column density map, produced by collapsing the full PPP cube, shown with the corresponding mean velocity map and intensity-weighted velocity dispersion map for the molecular line emission along the line of sight.

As shown in Figure 4.22, we have produced several Doppler-broadened velocity spectra maps for a dense region of our simulation from the generated PPV data cube. The resolution was chosen such that it would approximately match that in the dense core NH_3 observations used by Pineda et al. (2010) of 0.02 pc per pixel.

These types of spectral line grid maps are very commonly used to study the spatial dependence of molecular line profiles and to search for outflows

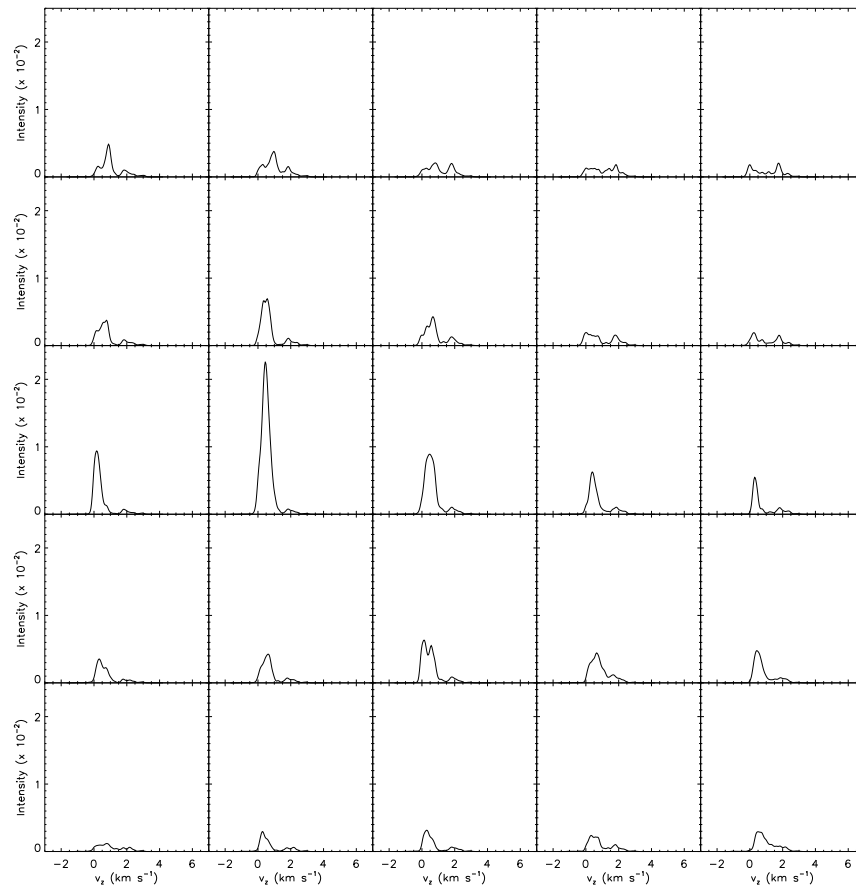


Figure 4.22: Doppler-broadened velocity spectra map generated from a PPV data cube with a resolution of 2000 AU/pixel and a velocity channel width of 0.04 km s^{-1} . These maps include all of the emission of the gas along the line of sight.

and evidence of rotation (e.g. Di Francesco et al., 2001; Ward-Thompson & Buckley, 2001; Rosolowsky et al., 2008).

As the most massive prestellar core evolves, preliminary results in Table 4.10 show that, although the calculated virial parameter is decreasing, the observed virial parameter and the velocity dispersion of the core is increasing.

Table 4.10: Evolution of σ & α_{vir} for the most massive “prestellar core”

	1.25 Myr	1.30 Myr	1.35 Myr
σ (km/s)	0.20	0.29	0.54
α_{obs}	0.657	0.937	1.778
α_{vir}	1.046	0.988	0.426

We would expect that as the calculated virial parameter decreases, the core is becoming more tightly bound. However, the observed virial parameter is increasing over time, as is the velocity dispersion, implying that the core is becoming less bound. The observed virial parameter is likely increasing due to its σ^2 dependence. It will be interesting to explore these results further and use new simulations to track our clumps through time to even later stages of evolution. This definition that a star-forming clump could be identified by a sharp transition to coherence could be the strongest evidence for the presence of a bound core, linking an observable LOS property to a true property of the cloud.

4.5 Summary

We used Clumpfind to identify dense regions in our simulated cloud and determined the global and individual properties of the identified clumps for various cases with different evolutionary stages, different orientations, and for different initial collapse conditions. We introduced our correlation method to estimate properties of three-dimensional star-forming clumps as they would be observed in a two-dimensional column density map and in a PPV spectral-line data cube. Based on these results, we found that projection has the greatest effect on estimates derived from PP column density maps. We identified a factor of 3 – 4 difference between our PP and PPP clump mass functions, which implies that the CMF shift from the stellar IMF to higher masses may not be related to a star formation efficiency at all, but instead may be solely due to an effect of projection. We conclude that clump properties are best derived from molecular-line data rather than continuum data, in order to minimize projection effects and produce trustworthy results.

We developed a boundedness test implementing the particles from the simulation of which the clumps are composed. Using the results of the boundedness test, we were able to classify our clump candidates as either a starless core or a prestellar core and show that prestellar cores which were formed at early times in our simulation remain bound at later times. We also noted that the filament case showed the highest percentage of bound clumps, which is in agreement with recent observations which show that filaments are a key component of star formation.

These results were followed by a discussion of the virial parameter and the velocity dispersion, which are the most likely traceable properties of bound cores. These observable properties, obtained from molecular-line data, are quite representative of the true properties of the cloud. We find that spectral-line observations are essential for the study of star formation in order to make any plausible claims regarding the properties of clumps and cores.

Bibliography

Alves, J., Lombardi, M. & Lada, C. J. 2007, *A&A*, 462, L17

Anathpindika, S. 2011, *New Astronomy*, 16, 477

Arzoumanian, D., André, P., Didelon, P., Könyves, V., Schneider, N., Men'shchikov, A., Soubie, T., Zavagno, A., Bontemps, S., di Francesco, J., Griffin, M., Hennemann, M., Hill, T., Kirk, J., Martin, P., Minier, V., Molinari, S., Motte, F., Peretto, N., Pezzuto, S., Spinoglio, L., Ward-Thompson, D., White, G., & Wilson, C. D. 2011, *A&A*, 529, 6

Bate, M. R. & Bonnell, I. A. 2005, *MNRAS*, 356, 1201

Bergin, E. A. & Tafalla, M. 2007, *ARA&A*, 45, 339

Bertoldi, F. & McKee, C. F. 1992, *ApJ*, 395, 140

Chabrier, G. 2005, *The Initial Mass Function 50 Years Later*, 327, 41

Di Francesco, J., Myers, P. C., Wilner, D. J., Ohashi, N., & Mardones, D. 2001, *ApJ*, 562, 770

Di Francesco, J., Evans, II, N. J., Caselli, P., Myers, P. C., Shirley, Y., Aikawa, Y., & Tafalla, M. 2007. An Observational Perspective of Low-Mass Dense Cores I: Internal Physical and Chemical Properties. In *Protostars and Planets V*, eds. B. Reipurth, D. Jewitt, and K. Keil (Tucson: University of Arizona Press), pp.17-32

Enoch, M. L., Evans, N. J., Sargent, A. I., Glenn, J., Rosolowsky, E., & Myers, P. 2008, *ApJ*, 684, 1240

Heyer, M. H., Carpenter, J. M., & Snell, R. L. 2001, *ApJ*, 551, 852

Kainulainen, J., Lada, C. J., Rathborne, J. M., & Alves, J. F. 2009, *A&A*, 497, 399

Kroupa, P. 2001, *MNRAS*, 322, 231

Larson, R. B. 1981, *MNRAS*, 194, 809

Men'shchikov, A., André, P., Didelon, P., Könyves, V., Schneider, N., Motte, F., Bontemps, S., Arzoumanian, D., Attard, M., Abergel, A., Baluteau, J.-P., Bernard, J.-P., Cambrésy, L., Cox, P., di Francesco, J., di Giorgio, A. M., Griffin, M., Hargrave, P., Huang, M., Kirk, J., Li, J. Z., Martin, P., Minier, V., Miville-Deschênes, M.-A., Molinari, S., Olofsson, G., Pezzuto, S., Roussel, H., Russeil, D., Saraceno, P., Sauvage, M., Sibthorpe, B., Spinoglio, L., Testi, L., Ward-Thompson, D., White, G., Wilson, C. D., Woodcraft, A., & Zavagno, A. 2010, *A&A*, 518, 103

Motte, F., André, P., & Neri, R. 1998, *A&A*, 336, 150

Motte, F., Zavagno, A., Bontemps, S., Schneider, N., Hennemann, M., di Francesco, J., André, P., Saraceno, P., Griffin, M., Marston, A., Ward-Thompson, D., White, G., Minier, V., Men'shchikov, A., Hill, T., Abergel, A., Anderson, L. D., Aussel, H., Balog, Z., Baluteau, J.-P., Bernard, J.-P., Cox, P., Csengeri, T., Deharveng, L., Didelon, P., di Giorgio, A.-M., Hargrave, P., Huang, M., Kirk, J., Leeks, S., Li, J. Z., Martin, P., Molinari,

- S., Nguyen-Luong, Q., Olofsson, G., Persi, P., Peretto, N., Pezzuto, S., Roussel, H., Russeil, D., Sadavoy, S., Sauvage, M., Sibthorpe, B., Spinoglio, L., Testi, L., Teyssier, D., Vavrek, R., Wilson, C. D., & Woodcraft, A. 2010, *A&A*, 518, L77
- Muench, A. A., Lada, E. A., Lada, C. J., & Alves, J. 2002, *ApJ*, 573, 366
- Myers, P. C. 1999, *The Physics and Chemistry of the Interstellar Medium*, Proceedings of the 3rd Cologne-Zermatt Symposium, Eds.: V. Ossenkopf, J. Stutzki, and G. Winnewisser, GCA-Verlag Herdecke, 227
- Offner, S. S. R., Klein, R. I., McKee, C. F., & Krumholz, M. R. 2009, *ApJ*, 703, 131
- Petitclerc, N. 2009, PhD Thesis, McMaster University
- Pineda, J. E., Goodman, A. A., Arce, H. G., Caselli, P., Foster, J. B., & Rosolowsky, E. W. 2010, *ApJ*, 712, L116
- Rathborne, J. M., Lada, C. J., Muench, A. A., Alves, J. F., Kainulainen, J., & Lombardi, M. 2009, *ApJ*, 699, 742
- Reid, M. A., Wadsley, J., Petitclerc, N., & Sills, A. 2010, *ApJ*, 719, 561
- Rosolowsky, E. W., Pineda, J. E., Foster, J. B., Borkin, M. A., Kauffmann, J., Caselli, P., Myers, P. C., & Goodman, A. A. 2008, *ApJS*, 175, 509
- Salpeter, E. E. 1955, *ApJ*, 121, 161
- Scalo, J. 1990, *Physical Processes in Fragmentation and Star Formation*, 162, 151

Schmalzl, M., Kainulainen, J., Quanz, S. P., Alves, J., Goodman, A. A., Henning, T., Launhardt, R., Pineda, J. E., & Román-Zúñiga, C. G. 2010, *ApJ*, 725, 1327

Shetty, R., Collins, D. C., Kauffmann, J., Goodman, A. A., Rosolowsky, E. W., & Norman, M. L. 2010, *ApJ*, 712, 1049

Simpson, R. J., Nutter, D., & Ward-Thompson, D. 2008, *MNRAS*, 391, 205

Solomon, P. M., Rivolo, R., Barrett, J., & Yahil, A. 1987, *ApJ*, 319, 730

Swift, J. J. & Williams, J. P. 2008, *ApJ*, 679, 552

Ward-Thompson, D. & Buckley, H. D. 2001, *MNRAS*, 327, 955

Williams, J. P., de Geus, E. J., & Blitz, L. 1994, *ApJ*, 428, 693

Chapter 5

Summary and Future Work

Observations of a star-forming region in the sky lack one fundamental component: the third dimension. It is important to understand how the projection of a three-dimensional structure can introduce bias into the analysis of observations and affect subsequent conclusions.

In this thesis, we used observer’s tools and techniques to study dense regions, called ‘clumps’, from synthetic observations of a molecular cloud and determine the clump properties at different stages of their evolution, for different orientations, and for four different initial cloud collapse conditions – Spherical, Ribbon, Sheet, and Filament. The synthetic observations were produced from the Petitclerc (2009) simulation of molecular cloud collapse and were used as a means to study the effects and biases which may result from the use of common observer’s tools, such as Clumpfind. Once the properties of the dense regions were determined, the clumps were then classified either as starless or prestellar cores.

We have seen that there are some cores, which would be identified in column density maps, may not necessarily be cores at all, but extended regions of low

density gas which, when projected onto a two-dimensional sky, appear as a single object. We have shown that this occurs quite frequently in observations. Clumpfind2d relies only on the column density map, where the more commonly used Clumpfind also requires the velocity spectrum along the line of sight. By correlating the clumps found in the PPP to those found in PP and PPV, we find that the properties of objects derived from PPV spectral-line data cubes were more representative of the true physical properties of the clumps than those obtained from the PP column density map. We found that effects of projection greatly impacted estimates of clump properties derived from two-dimensional column density maps. Our results indicate that the observed shift of the CMF from the stellar IMF to higher masses (Alves et al., 2007) is likely not the result of a star formation efficiency factor, but instead may be solely due to an effect of projection. Thus, any analysis based purely on two-dimensional data should be done with the utmost care.

We developed a boundedness test which determined whether or not an identified object was gravitationally bound by using the intrinsic energies of the SPH particles. We noted that the few bound objects identified in the PP column density map could not be classified as cores, as they were all located at the outer edges of the cloud, very far from regions of high-density, and were so large and diffuse that they would likely be rejected by manual identification methods. Our results for the PPP case showed that many of the dense objects identified by Clumpfind were unbound starless cores with only a few bound prestellar cores, which is expected at such an early stage of star formation. By tracking the evolution of the prestellar cores, we found that those which were formed at early times in our simulation remain bound at later times.

Two traceable properties of bound cores, the virial parameter and the velocity dispersion, can be obtained from molecular-line observations and appear to be quite representative of the true properties of the cloud.

We conclude that spectral-line observations are essential for the study of star formation. Core properties are best derived from PPV data cubes rather than PP dust continuum maps, in order to minimize projection effects and maximize the identification of truly bound structures in observations. ALMA is poised to reach incredible spatial and spectral resolutions and should prove to be the most powerful tool for future discoveries in star formation.

Since the timescale for star formation is measured in thousands to millions of years, we cannot observationally follow one particular cloud as it collapses, forms cores, and then stars. Our understanding of the process is drawn from observations of multiple star-forming regions in the Galaxy, and estimates of the ages of each system and the different stages each represents. We are currently running a simulation of a $50000 M_{\odot}$ molecular cloud to track the evolution of the cores from the initial collapse of the cloud through to the pre-main sequence evolutionary phase. As the cores evolve, we will be able to see how often they will merge and collapse into bound objects and how often they disperse to determine a statistical likelihood that an observed core will eventually become a star. The study of the core evolution will provide insight into the formation mechanisms of multiple star systems, such as binaries, and will also give an indication of the multiplicity of these objects in observations; for example, how often a single, identified core is, in reality, two or more widely separated cores which have been confused in projection.

We also intend to run a simulation incorporating the effect of radiative feedback from the protostars using a radiative transfer code recently implemented in Gasoline (Rogers & Wadsley, 2011). Since we are interested in studying the later stages of pre-main sequence stellar evolution when the cores become associated with a compact source of luminosity and are emitting protostellar radiation, we need to understand the effects of localized heating due to the radiative feedback from newly-formed stars and determine the significance of the addition of radiative transfer under the conditions of our simulation.

Our research has shown that the effects of projection can distort our view of how stars form. Just as observations continue to reveal new and exciting features of the star formation mechanism, so too will simulations play an important role in defining the overall picture of stellar birth in the Galaxy.

Bibliography

Alves, J., Lombardi, M. & Lada, C. J. 2007, *A&A*, 462, L17

Petitclerc, N. 2009, PhD Thesis, McMaster University

Rogers, P. D. & Wadsley, J. 2011, *MNRAS*, 414, 913